POLYTECHNIQUE MONTRÉAL
affiliée à l'Université de Montréal

Composite Aircraft Lightning Strike Protection Damage Evaluation Using Microwave Microscopy

LEANDRO MIGUEL RUFAIL
Département de génie électrique

Thèse présentée en vue de l'obtention du diplôme de *Philosophiæ Doctor*
Génie électrique

Août 2020

© Leandro Miguel Rufail, 2020.

POLYTECHNIQUE MONTRÉAL
affiliée à l'Université de Montréal

Cette thèse intitulée :

Composite Aircraft Lightning Strike Protection Damage Evaluation Using Microwave Microscopy

présentée par **Leandro Miguel RUFAIL**
en vue de l'obtention du diplôme de *Philosophiæ Doctor*
a été dûment acceptée par le jury d'examen constitué de :

Mohammad S. SHARAWI Ph.D., président
Jean-Jacques LAURIN Ph.D., membre et directeur de recherche
Ke WU Ph.D., membre
Vahé NERGUIZIAN Ph.D., membre externe

DEDICATION

To all my friends . . .

ACKNOWLEDGEMENTS

Firstly, I would like to express my gratitude to my supervisor Prof. Jean-Jacques Laurin for his continuous support, for his infinite patience, his motivation, and knowledge. His advice helped me in all the time of research as well as in the writing of this thesis.

Besides my advisor, I would like to thank the rest of my thesis committee: Prof. Ke Wu, Prof. Vahé Nerguizian, and Dr. Mohammad Sharawi, for the time devoted for reading and correcting this work.

I would also like to express my gratitude to Dr. Fidèle Moupfouma and *Bombardier Aeronautique* who believed in this project and support it from the very beginning.

Finally, big thanks for the assistance of all technical staffs at the Poly-Grames Research Centre. I want to thank Mr. Jules Gauthier, Mr. Steve Dubé and Mr. Traian Antonescu who have helped in realizing all devices and pieces that were used in this project. I am grateful to Mr. Jean-Sébastien Décarie for troubleshooting all computer problems and to Mrs. Nathalie Lévesque, and Mrs. Rachel Lortie for their help on administrative matters.

RÉSUMÉ

Au cours des 30 dernières années, les concepteurs d'avions se sont tournés vers les matériaux composites pour fabriquer leurs véhicules plus légers, plus économes en carburants et plus confortable pour les passagers. Les matériaux composites présentent un certain nombre d'avantages substantiels par rapport au métal, traditionnellement utilisés dans l'industrie. L'une de leurs principales propriétés est un rapport rigidité/poids très élevé. Des fibres très rigides (généralement des fibres de carbone ou verre) sont incorporées dans un matrice (généralement de la résine époxy). Un deuxième avantage par rapport au métal est leur tolérance à la corrosion. Les métaux sont sensibles à la fois à la corrosion et à la fatigue. Les composites ne se corrodent pas, et ils ne sont pas soumis à des dommages de fatigue dans l'étendue des structures métalliques. Par contre, les composites ne sont pas conducteurs (par exemple la fibre de verre) ou sont nettement moins conducteurs que les métaux (par exemple la fibre de carbone), et ne peuvent donc pas évacuer les courants intenses développées lors d'un événement de foudre. Les constructeurs d'avions ont mis au point un certain nombre de techniques spécialisées de protection contre la foudre (LSP en anglais). Bien que les LSP soient devenus d'un intérêt primordial au fil des ans comme moyen de protéger les structures composites, aucune technique n'a été trouvée pour diagnostiquer les LSP en fonction des exigences des fabricants. Les travaux de cette thèse ont été partiellement financés par *Bombardier Aérospatiale*. Elle se concentrera sur une forme particulière de LSP, à savoir la feuille de cuivre expansée (ECF en anglais) qui est largement utilisée dans la plupart des avions de long courrier de Bombardier.

Le premier chapitre de cette thèse consite en une revue des techniques les plus répandues actuellement utilisées dans l'évaluation des polymères renforcés de fibres de carbone (CFRP en anglais). Il compare ces techniques et indique leurs limites et contraintes pour résoudre le problème formulé. Une introduction à la microscopie micro-onde en champ proche est également présentée dans ce chapitre. Elle représente le noyau de tous les développements de cette thèse.

Il y a de nombreuses variables qui interviennent dans la technique de microscopie micro-onde et qui doivent être adaptées à l'objectif de ce travail. Le Chapitre 2 est une exploration des sondes électriques en champ proche ainsi qu'une analyse du dispositif de mesure correspondant. Il fixe les limites, les avantages et les inconvénients de l'applicabilité de la microscopie à micro-ondes pour l'évaluation des CFRP. Une sonde à guide d'onde coplanaire est utilisée ici pour démontrer que des défauts peuvent être trouvés dans le maillage LSP. Les limites de

cette conception vont ouvrir la porte au développement d'une sonde magnétique.

Une nouvelle application de la technique de microscopie à micro-ondes est démontrée expérimentalement au Chapitre 3. Une nouvelle conception de sonde magnétique est introduite, capable de révéler des défauts dans le LSP, sous la couche. Une application potentielle de la mesure de l'épaisseur de la peinture est également identifiée.

L'objectif principal de cette thèse est le développement de méthodes et d'outils pour diagnostiquer les LSP qui sont appliqués sur le fuselage d'un avion. Ainsi, des grandes surfaces doivent être inspectées à la recherche de petits défauts. Afin d'accélérer les tests, un ensemble de 6 sondes qui sont reliées au dispositif de mesure par un interrupteur RF est décrit au Chapitre 4. La démonstration expérimentale des capacités du réseau de sondes a été faite sur des échantillons de panneaux CFRP frappés par la foudre et aussi sans dommages.

Finalement, deux variables importantes qui jouent un rôle clé dans le développement des nouvelles applications pour cette technique sont la portabilité et le temps de mesure. Une méthode d'interpolation qui peut accélérer les mesures des plusieurs ordres de grandeur est expliquée dans le dernier chapitre. L'algorithme proposé est appliqué dans des modèles simulés et des expériences de laboratoire. Il a été confirmé que les exigences en matière des appareils de mesure peuvent être assouplies et que le temps de mesure peut être considérablement réduit.

ABSTRACT

The last decades have seen a surge in the amount of composite materials used by the aircraft industry. This tendency is mainly due to a key advantage of composites compared with traditional aluminum alloys. They have strength while lowering the overall weight of the aircraft, which saves fuel consumption and improve efficiency and performance. A second advantage over metal is their tolerance to corrosion. Metals are susceptible to both corrosion and fatigue. Composites do not corrode, and they are not subject to fatigue damage to the extent of metal structures. Conversely, composites are either not conductive (e.g. fiberglass) or significantly less conductive than metals (e.g., carbon fiber), so they can not conduct away the intense currents developed during a lightning event. Aircraft manufacturers have developed a number of specialized lightning strike protection materials (LSP). Even though LSP has become of paramount interest over the years as a means to protect composite structures, no techniques have been found to diagnose LSP according to manufactures requirements. Since this work was partially supported by *Bombardier Aerospace*, it will be concentrated in one particular form of LSP, namely expanded copper foil (ECF) which is widely used in most Bombardier long courier aircraft.

The first chapter of this thesis reviews the most established techniques currently used in carbon fiber reinforced polymer (CFRP) evaluation. It compares these techniques and it states their limitations and constraints to solve the formulated problem. An introduction of near field microwave microscopy is also presented in this chapter which will be the core of all developments in this dissertation.

There are many variables that intervene in microwave microscopy technique that must be adapted to the purpose of this work. Chapter 2 is an exploration of near filed electric probes and analysis of the related measurement set-up. It sets the limits, pros and cons of the applicability of microwave microscopy for scanning CFRP. A coplanar waveguide probe is used here to demonstrate that defects can be found in LSP mesh. The limits of this design prompts the development of a magnetic probe.

A new application of microwave microscopy technique is experimentally demonstrated in Chapter 3. A new magnetic probe design is introduced capable of revealing flaws as small as 100 µm in the LSP, even under 350 µm thick paint layer. A potential application consisting of measuring the paint thickness is identified as well. Experimental measurements of the paint layer thickness with a resolution better than 2 µm have been demonstrated.

The main objective of this thesis is the development of methods and tools to diagnose LSP

that are applied on an aircraft fuselage. As such, large surfaces needs to be inspected in the search for small defects. An array of 6 probes that are linked to the measurement set-up trough an RF switch is described in Chapter 4 in an effort to cover larger surfaces. Experimental demonstration of the array capabilities are proven on samples of CFRP panels struck by lightning and also undamaged.

Finally, two important variables that play a key role in developing new applications for this technique are portability and time. An interpolation method that can accelerate measurements by several orders of magnitude is described in the last chapter. The proposed algorithm is applied in simulated models and experiments. It was confirmed that requirements in the measurement set-up can be relaxed, and measurement time can be substantially decreased from 16 min/cm^2 to less than 3 min/cm^2.

TABLE OF CONTENTS

DEDICATION iii

ACKNOWLEDGEMENTS iv

RÉSUMÉ v

ABSTRACT vii

TABLE OF CONTENTS ix

LIST OF TABLES xii

LIST OF FIGURES xiii

LIST OF SYMBOLS AND ACRONYMS xvii

LIST OF APPENDICES xviii

CHAPTER 1 INTRODUCTION 1
- 1.1 Lightning and aircraft 1
- 1.2 Non-destructive Testing for Composites: Different inspection methods 7
  - 1.2.1 Ultrasonic A-Scan and S-Scan 7
  - 1.2.2 Thermograpy 8
  - 1.2.3 Shearography 8
  - 1.2.4 Eddy currents 8
  - 1.2.5 Microwave near-field imaging 9
  - 1.2.6 X-ray inspection 9
- 1.3 Near field microwave microscopy 10
- 1.4 Goals and Motivation 12
- 1.5 Thesis Contributions 12

CHAPTER 2 ELECTRIC PROBE 14
- 2.1 Introduction 14
  - 2.1.1 Equivalent circuit. 15
- 2.2 Experimental set-up 17
- 2.3 Width gauge 20

2.4 Grooves gauge 21
2.5 Coplanar waveguide probe 27
2.5.1 CPW probe experimental results 32
2.6 Conclusions 36

CHAPTER 3 MAGNETIC PROBE 39
3.1 Introduction 39
3.2 Magnetic Probe - loop antenna 41
3.3 Experimental results 45
3.3.1 Balanced probe 47
3.3.2 Shielded Probe 49
3.3.3 Misaligned scanning 55
3.4 Conclusion 55

CHAPTER 4 PROBE ARRAY 59
4.1 Introduction 59
4.2 RF switch 61
4.2.1 Switch perturbation analysis 62
4.3 General Purpose USB to GPIO 65
4.4 Control software 65
4.4.1 Main routine auxiliary functions 67
4.4.2 Probe calibration subroutine 68
4.5 Experimental Results 70
4.5.1 Probe deterioration 70
4.5.2 Calibration correction procedure 71
4.5.3 Samples 74
4.5.4 Sample measurements 75
4.6 Conclusion 82

CHAPTER 5 PROBE MEASUREMENT ACCELERATION TECHNIQUE 83
5.1 Introduction 83
5.1.1 Equivalent circuit 84
5.1.2 Fractional Linear Transformation curve fitting 88
5.1.3 Simulation results 93
5.1.4 Experimental results 101
5.2 Conclusion 103

CHAPTER 6 CONCLUSION 105
6.1 Conclusions 105
6.2 Future work 106
6.2.1 Instrument specifications 106
6.2.2 Reduction of resonator size 106
6.2.3 X-rays validation 107

REFERENCES 108

APPENDICES 115
A.1 Main control program 115
A.2 Calibration function 123

LIST OF TABLES

3.1 Electric and Magnetic probe features comparison 56
5.1 Resonant frequencies - Raw data and Interpolated data 103
5.2 Measurement time per probe per position (sec) and per square centimeter (min). 103

LIST OF FIGURES

1.1 Composites are used in more than 50% of the *Boing 787* aircraft fuselage [1]. 2
1.2 Typical path of swept-channel attachment points [2]. 3
1.3 Damage produced by the initial entry and final exit of lightning current [3]. 3
1.4 Composite skin with integrated copper mesh. 4
1.5 CFRP stack [1]. 6
1.6 Lightning superficial damage [4]. 6
1.7 Transmission radiography of a composite specimen composed of paper honeycomb core and metal (copper) surface grid. 10
2.1 Schematic of the experimental set-up. 15
2.2 Set-up simplified model. 15
2.3 Sample-tip lumped element model. 16
2.4 $|S_{11}|$ circuit response for C_p=0.1, 0.5 and 1 pF and R =0 Ω. (a) 2 resonant modes. (b) one resonant mode. 17
2.5 Smith chart representation of S_{11} for C_p=0.1, 0.5 and 1 pF and R =0 Ω. 18
2.6 Micro-coax probe and CPW transition. 19
2.7 Experimental set-up. 19
2.8 Micro-coax probe measurements. Grounded dielectric sample, copper and no-sample. 20
2.9 Strip width gauge. 21
2.10 Measuread $|S_{11}|$ every 0.1 mm over a path length of 100 mm. 22
2.11 Width gauge measurement. Probe displacement steps of 0.1 mm. The blue regions in the test samples are metallized. 23
2.12 Alumina substrate with slots 50.8 µm to 254 µm - 25 µm steps. . . . 23
2.13 Alumina slots. Probe over 254 µm slot. 24
2.14 Measurements for $Pos1$ and $Pos2$ positions. 24
2.15 Sharpened micro-coaxial tip. 25
2.16 Sharpened micro-coaxial tip scanning 127 µm width slot 25
2.17 Near field simulation models. 26
2.18 Near E field magnitude distribution at 1 GHz. 26
2.19 Lift-off distance control. 27

2.20 Measurements of the probe scanning 254 µm, 228 µm and 203 µm Slots, $Pos1$ and $Pos2$ points. 28
2.21 Open CPW on finite thickness substrate over sample. 30
2.22 Kapton CPW probe. 12.7 µm substrate. (a) Side view. (b) Top view. 30
2.23 Simulated $|S_{11}|$ for probe-sample separation values of: 50, 100, 150, 200, 250, 350, 450, 550, 650, 750, 850, 950, 1050, 1150, 1350, 1550, 2000, 2500, 3000, 3500, 4000, 5000 µm. 31
2.24 Probe $|S_{11}|$ measurements. Gap between center line and ground plane of 152, 177, and 254 µm. 32
2.25 Measured $|S_{11}|$ for probe-sample separation values of: 50, 100, 150, 200, 250, 350, 450, 550, 650, 750, 850, 950, 1050, 1150, 1350, 1550, 2000, 2500, 3000, 3500, 4000, 5000 µm. 33
2.26 CPW probe and sample on probe station. 34
2.27 CFRP sample. 35
2.28 $|S_{11}|$ at resonant frequency as a function of distance. 36
2.29 Resonant frequency shifts as a function of distance. 37
3.1 Schematic of the experimental set-up. A photograph of the balanced loop probe is shown in the top right corner. 40
3.2 ADS set-up simplified model. 40
3.3 Circuit response for $L = 1, 2, 3nH$ and $R = 0\Omega$. (a) S_{11} and (b) Q circles. 42
3.4 Circuit response for $L = 1nH$ and $R = 0, 5, 10\Omega$. (a) S_{11} and (b) Q circles. 42
3.5 Wire mesh and probe simulation model. 43
3.6 Equivalent circuit representing the interaction between the loop probe and the mesh. 44
3.7 Simulated probe input impedance for simple probe (green) and shielded probe (violet). Fixed (solid) and variable separation (dashed). 45
3.8 Simulated probe input impedance for simple probe (dashed) and shielded probe (solid). 46
3.9 CFRP sample. 47
3.10 Printed loop probe with integrated balun scanning the sample. 48
3.11 Measured loop probe frequency shifts and optically measured paint thickness vs distance. 49
3.12 Planar multi-layer shielded probe. 50

3.13 Photograph of the two sides of shielded probe printed on a T-shaped substrate. Dimensions are given in Fig. 3.12. (a) Feeding microstrip line. (b) Ground plane. 50
3.14 Shielded loop probe scan over the CFRP sample. (a) Resonance frequency shift and paint thickness. (b) Resonance frequency shift and $|S_{11}|$ at resonance. (c) Amplitude of frequency shift oscillations versus paint thickness. 51
3.15 Scan Area - Contours every $1.5kHz$. 54
3.16 Optical photographs showing defects 1 and 2. In (a) six cell loop paths are interrupted. In (b) one cell loop is discontinued. 55
3.17 Probe scanning sample and tape. Scanning angle of 12° 56
3.18 Scan over sample and tape. Scanning angle of (a) 0°, (b) 6°, (c) 12° . 57
4.1 Probe array. 59
4.2 Probe array sweeping CFRP panel. 60
4.3 Simplified model SP6T 60
4.4 Measurement set-up - devices and interfaces. 61
4.5 Minicircuits RF switch evaluation board [5]. 62
4.6 Minicircuits RF switch S parameters. $RF1$ output is selected. . . . 63
4.7 Perturbation analysis simulation model. 64
4.8 Center loop input reactance. Parasitic probes short and open. 64
4.9 Adafruit FT232H control board. 65
4.10 Main program flow chart. 66
4.11 Probe calibration subroutine. 69
4.12 Worn-out probe tip. 70
4.13 Protected array. 71
4.14 Undamaged painted CFRP sample - Uncorrected raw data. 72
4.15 Changes in resonance frequency of each probe due to different RF signal paths in the switch. 73
4.16 Undamaged CFRP - 3D Normalized surface. 74
4.17 Undamaged CFRP sample. The ruler scale is in cm. 76
4.18 8 steps milled sample in strips of $12mm$. 76
4.19 CFRP sample damaged by lightning strike. 77
4.20 Undamaged CFRP with deep cut - 3D Normalized frequency shift surface. 77
4.21 Undamaged CFRP. Normalized frequency shift contours. The inset shows a zoom of the region near the deep cut. 78

4.22 Stepped CFRP sample - 3D Normalized frequency shift surface. . . . 79
4.23 Stepped CFRP sample. Normalized frequency shift contours. 80
4.24 CFRP sample damaged by lightning strike - 3D Normalized frequency shift surface. 80
4.25 CFRP sample damage by lightning. Normalized frequency shift contours. 81
5.1 ADS set-up simplified model. 85
5.2 Resonator coupled to the source by a lossless two-port. 86
5.3 Input reflection coefficient as a function of frequency. 89
5.4 Generic lossless two-port network. 89
5.5 Values of Γ_{L1},Γ_c, Γ_s for the 1st iteration. 94
5.6 Values of Γ_{L1},Γ_c, Γ_s for the 2nd iteration. 94
5.7 Γ_i for L=2.5, 2.75 and 3 nH. (a) Γ_i magnitude. (b) Γ_i Smith chart. . 95
5.8 Wire mesh and probe simulation model. Probe at $x = -3.175mm$ $(-1LWD)$ 96
5.9 Simulated probe in the 1st (a), 2nd (b) and 3rd (c) positions. 96
5.10 Γ_i for 5 positions. (a) Γ_i magnitude for positions 1 to 5. (b) Γ_i Smith chart for positions 1,2 and 3. 97
5.11 Resonance frequencies estimated with 21 frequency points. Probe at $x = 0$, $\frac{1}{4}LWD$, $\frac{1}{2}LWD$, $\frac{3}{4}LWD$, LWD. 98
5.12 ADS Γ_i simulation with 5 frequency points. Probe at positions 1, 2 and 3. 99
5.13 Resonance frequencies estimated with 5 frequency points. Probe at positions 1, 2 and 3. 100
5.14 ADS Γ_i simulation with 5 frequency points over $6LWD$ 100
5.15 Γ_i Micro-coax probe measurements. 401 frequency points. 101
5.16 Γ_i Micro-coax probe measurements. 5 frequency points. 102

LIST OF SYMBOLS AND ACRONYMS

LSP	Lightning Strike Protection
CFRP	Carbon Fiber Reinforced Polymer
ECF	Expanded Copper Foil
IF	Intermidiate Frequency
VNA	Vector Network Analyzer
PNA	Performance Network Analyzer
LWD	Long Way of Design
SWD	Short Way of Design
PCB	Printed Circuit Board
SP6T	Single Pole Six Throw
USB	Universal Serial Bus
RF	Radio Frequency
GPIO	General Purpose Input Output
MoM	Method of Moments
DLL	Dynamic Linked Library
SCPI	Commands for Programmable Instruments
FAA	Federal Aviation Administration
NDI	Non-destructive Inspection
CT	Computer Tomography
CPW	Coplanar Waveguide
FEM	Finite Element Method
NDE	Non-Destructive Evaluation

LIST OF APPENDICES

Appendix A Matlab Code 115
Appendix B C Code: FT232H 127
Appendix C Publications 129

CHAPTER 1 INTRODUCTION

1.1 Lightning and aircraft

Lightning stroke is is a sudden flow of electric charge between an electrically charged area of a cloud and another cloud, or between a charged cloud and the ground. Lightning can happen at any moment if a region of the atmosphere attains an electric charge sufficiently large to cause electric breakdown. The lightning stroke mechanism can be broken down into several parts. Initially, as soon as the air near the clouds breaks down, a leader streamer starts flowing from negatively charged region (cloud) to the positively charged one (earth). As the leader streamer reaches the earth, a return stroke triggers from the earth to the cloud, following the same path previously opened by the downward leader (channel). This phenomenon causes a spark that is usually referred as lightning. Even when this phenomenon appears to the eye as a single isolated flash, in reality, it is composed of a number of separate strokes that travel down the same path within milliseconds. A lightning discharge may have currents in the range of 10 kA to 200 kA and voltages up to 1 million volts.

According to statistics published by the Royal Canadian Air Force and the U.S. Federal Aviation Administration (FAA), a plane can be struck by lightning on average once every 1000 to 3000 flight hours. For commercial aircraft, that is equivalent to one strike per aircraft per year. [6]

In the last 30 years, aircraft designers have been turning to composites to make their vehicles lighter, more fuel-efficient and more comfortable for passengers. Half of the materials used in the construction of *Boeing 787* and the *Airbus A350*, for example, are composites. Figure 1.1 shows the different materials used in a *Boeing 787 Dreamliner* today.

Composites present a number of substantial advantages to aircraft designers as well as new challenges. Among the pros of composites we can cite their very high stiffness-to-weight ratio. Very stiff fibers (usually carbon or glass) are embedded in a matrix (typically epoxy resin). A second advantage over metal is their tolerance to corrosion. Metals are susceptible to both corrosion and fatigue. Composites do not corrode, and they are not subject to fatigue damage to the extend of metal structures. Despite all the advantages, aircraft manufacturers are cautious in transitioning from metal to composites. One reason is that composites are essentially a laminated structure composed of many ply layers bound together. This structure can delaminate between layers. Delamination and cracks in the composite are usually internal and will not be visible from the surface. They are also hard to detect with today's inspection

techniques.

Figure 1.1 Composites are used in more than 50% of the *Boing 787* aircraft fuselage [1].

The question of what happens when lightning strikes a composite airplane naturally arises at this point. During a lightning incident the aircraft forms a part of the discharge path (swept channel - See Figure 1.2) between regions of opposite polarity (cloud to cloud or cloud to ground). Therefore, there are typically two attachment points. One entry point (i.e. the nacelles) and one exit point (i.e. the tail). The current will travel through the protective exterior skin and grounding structures of the aircraft between these two points. Because of the relative movement of the plane compared to the lightning channel, the lightning flash is displaced along the aircraft reattaching itself at other locations on the fuselage. A picture of the damage showing entry point at the nose and exit point at the tail is shown in Figure 1.3

When a lightning bolt strikes an unprotected structure, extremely high currents developed on the surface of the aircraft are seeking the least resistance path. In the process, it may vaporize metal control cables, weld hinges on control surfaces and even explode fuel vapors within fuel tanks if current arcs through gaps around fasteners [7]. These direct effects also include vaporization of resin in the strike area, with possible burn-through of the laminate.

Unlike their metal counterparts, composite structures do not efficiently conduct away extreme currents developed during a lightning event because they are either not conductive (e.g. fiberglass) or significantly less conductive than metals (e.g., carbon fiber). The damage caused during a lightning event is mainly due to the matrix resin thermal stress which is

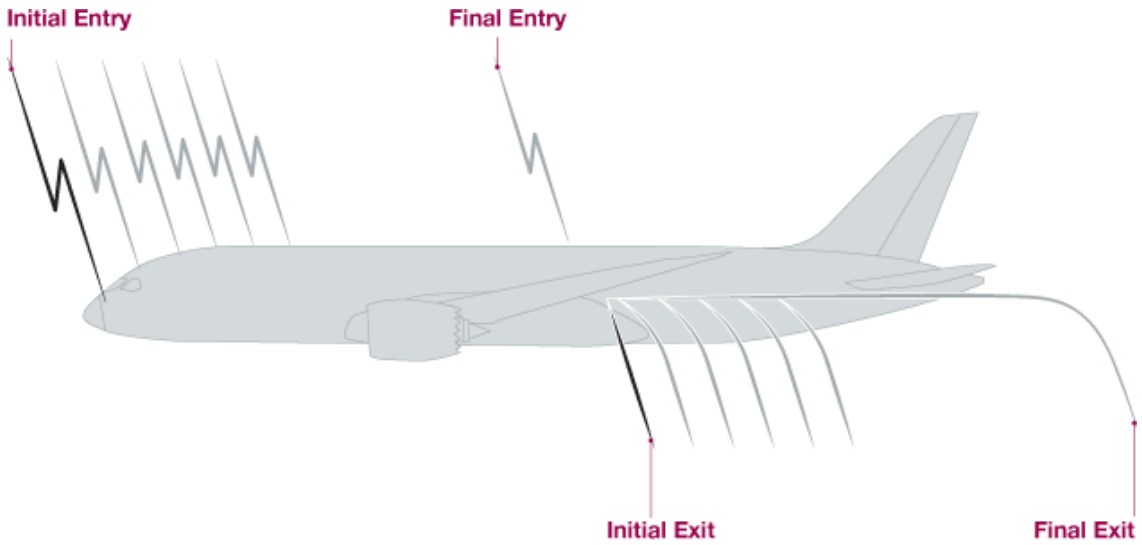

Figure 1.2 Typical path of swept-channel attachment points [2].

Figure 1.3 Damage produced by the initial entry and final exit of lightning current [3].

generated by high conduction current joule effect. Moreover, fiber sublimation, carbon fiber rupture and decline in the inter-laminar strength are caused by the thermal decomposition of resin and pyrolisis gas pressure between layers. For this reason, lightning strike protection (LSP) has been a significant concern since aircraft industry started using composites.

Direct effects of lightning, as explained earlier, are related to the physical damage caused by the conduction of the current into the structure of the aircraft. On the other hand, indirect effects are related to disturbances to avionic equipment caused by the high intensity electric or magnetic field. The lightning arc induces transient voltages that can destroy onboard electronics that have not been properly shielded or lightning protected.

The necessity for protection of composite structures has prompted development of a number of specific lightning strike protection materials (LSP). Those materials and strategies share as a common goal which is to decrease the surface resistance of the structure and spread over the directly coupled or magnetically induced current path [8]. Multiple LSP solutions has been adopted over the years as the use of composites gain popularity during the past decades. Since composites have a poor electrical conductivity, all LSP solutions intend to provide a continuous conductive path of low resistance over the aircraft exterior. Among the most popular techniques we count the LSP metal mesh or foil (see Fig. 1.4).

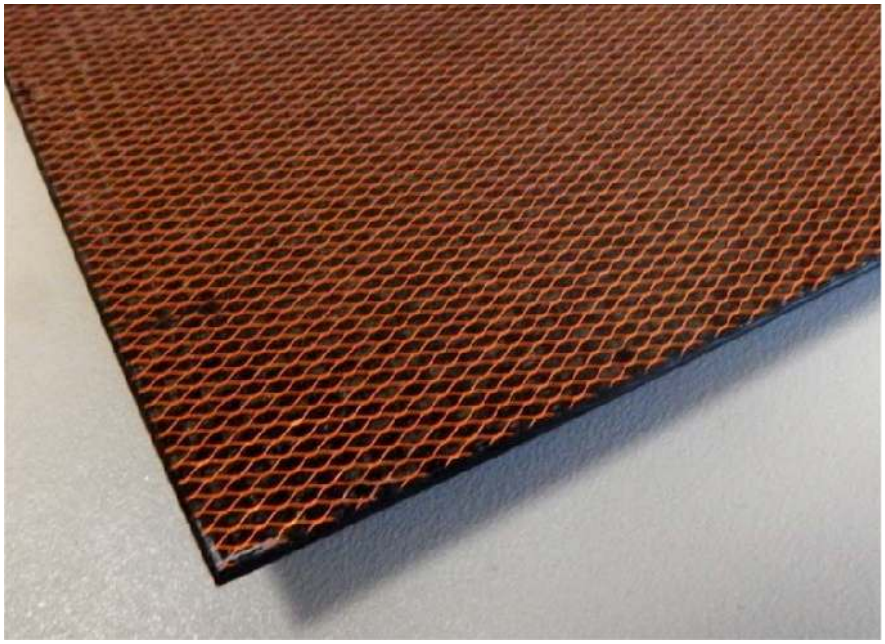

Figure 1.4 Composite skin with integrated copper mesh.

Typically, it is a fine, lightweight mesh (aluminum or copper) or foil embedded in a surfacing film within the outer laminate ply. It is placed in contact with metal bonding strips or

other structures that connect the outer conductive surface to a metallic grounding point or internal "ground plane". Another alternative technique involves coating carbon fibers with highly conductive materials; for instance a nonwoven veil made with randomly oriented nickel, copper-coated-carbon fibers [9] or coating a carbon nonwoven sheet with nickel. A third group of techniques consists of sprayable conductive paint or a surfacing film that is post applied over the carbon fiber reinforced polymer (CFRP) sandwich. Out of all solutions, in the present work, we will concentrate exclusively on the expanded copper foiled (ECF) wire mesh. The present project originated from a collaboration between *Polytechnique Montréal* and *Bombardier Aerospace*, particularly for the *C-Series* program at its beginnings. The goal is to develop tools that allow the company to assess the condition of the installed LSP. Since the main lightning protection mechanism presently used in the *C-Series* program is of wire mesh type, all the investigation in the current work is centered around this kind of LSP protection.

Damage in the LSP can occur before or after a lighting episode. Also, the damage to LSP mesh can be progressive. Since aluminum, because of its lightweight, is one of the primary choices for LSP meshes, galvanic corrosion can be a problem [10]. The risk of galvanic corrosion arises when two dissimilar metals function similarly to a battery, causing the metal that acts as the anode to corrode. An isolation ply is needed between them in order to avoid the later effect. Furthermore, if moisture penetrates the composite skin, aluminum corrosion can also occur. A picture showing all the layer in a standard CFRP stack is shown in Fig. 1.5.

After lightning strikes a plane, the damaged zone must be inspected. The amount and type of damage an airplane experiences can vary depending on factors such as the current intensity of the strike, attachment and exit locations and the duration of the strike. At the same time, those factors are strongly related to the probability of lightning to attach to different zones of the aircraft (FAA zones). Visual inspection is the most popular technique to evaluate damage. A well-formed technician looks for the entrance, exit points and pinholes. Sometimes the damage is evident, (e.g. when delamination occurs) and sometimes it is not. The outer surface burns just look like pepper sprinkled over the paint. Example of superficial damage is given in Fig. 1.6.

Paint thickness is also of primary importance [11]. It has been demonstrated that the lightning arc root radius is inversely related to the paint thickness. The arc root radius is defined as the radius of the arc attachment to the surface of the fuselage. So, small root radius means intensive current and heat concentration. Therefore, paint thickness has to be controlled and maintained under a prescribed upper limit. When the paint thickness increases

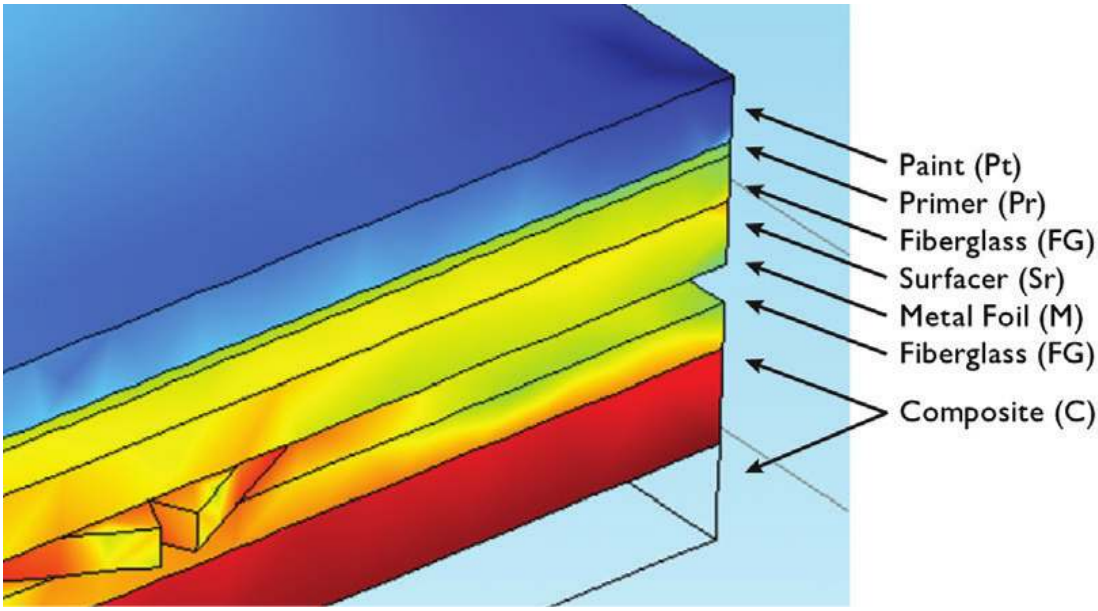

Figure 1.5 CFRP stack [1].

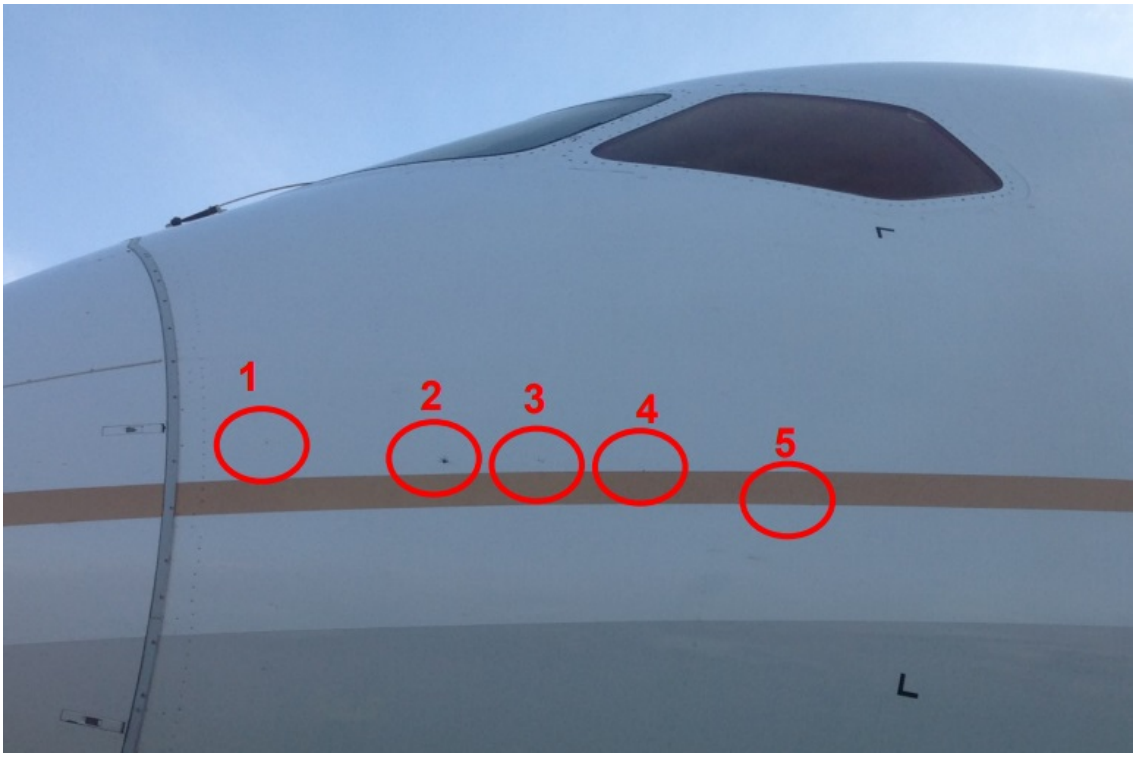

Figure 1.6 Lightning superficial damage [4].

over certain value, several dielectric breakdowns occur as a consequence of the conductive path between the plies which gives rise to internal sparking phenomena. Then, the panel experiences delaminations and punctures of the stratified material [11, 12].

In summary, LSP is a big concern of aircraft industry and it needs to be accurately evaluated during panel assembly, after lightning strikes and repairs. Non-destructive techniques currently used to inspect composites will be briefly reviewed in the next section.

1.2 Non-destructive Testing for Composites: Different inspection methods

With more and more composite material on aircraft, knowing how to inspect them for damage is an important topic. In this section we will describe some of the most widespread non-destructive inspection techniques (NDI) and examine their potential for finding defects in LSP mesh. All techniques, presented briefly below, aim to detected structural flaws in composites, such as disbonds, delaminations, porosity and others. As such, their resolution is too large to discriminate defects in the wire mesh. Here, we define lateral resolution as the ability of the system to locate discontinuities that are close together. For the wire mesh, sometimes a strand is cut by a gap of a few micrometers width and it needs to be detected. The most relevant inspections techniques that will be briefly described in the following paragraphs are ultrasonic A-Scan and C-Scan, thermograpy, shearography and x-ray inspection [13].

1.2.1 Ultrasonic A-Scan and S-Scan

A-Scan and C-Scan are two variants of ultrasonic techniques. These techniques detect variations in the acoustic impedance of a medium. A-Scan ultrasonics uses a pulse-echo system (i.e. pulse reflection) to locate flaws. A transducer probe is placed on the surface to be inspected using a liquid couplant to ensure good sound conductivity. The probe then transmits ultrasonic pulses through the part. The system measures the time the pulses takes to bounce from the back surface of the part. Flaws in the material would result in a different times respectively to a calibration reference.

Similarly, to A-Scan technique, a C-Scan device measures the amount of time that the sound passes through the thickness of the part. For this reason, access to both sides of the part is required. This technique also needs a liquid medium to couple the probe to the material under test ensuring good sound transmission.

Typical frequencies that are used in ultrasonic techniques are in the low MHz range (1 MHz to 10 MHz) for composite materials. Lowering the frequency degrades spatial resolution as depth profile forming is directly related to the ultrasonic wavelength. Increasing the frequency

leads to excessive attenuation of the ultrasonic signal. The lateral resolution of ultrasonic depends on the width of the beam generated by the transducer, which is approximately equal to the width of the transducer [14]. In high frequency ultrasonics, the transducer radius is in the order of a mm which is too large to detect flaws in the LSP mesh. More importantly, a small break in one diamond of the LSP mesh would not affect the mechanical property of the tested sample significantly. Therefore, methods based on acoustic waves do not appear promising for this application.

1.2.2 Thermograpy

Thermography can be used to inspect composite structures. It consists in applying heat to a part that needs to be inspected. Subsequently, the part is viewed through an infrared camera as it cools down. This can give indications of a flaw. In the presence of a defect, the induced heat will locally build up and will be seen as a hot spot in reflection or a cold spot in transmission. It is a volumetric inspection approach not suitable to inspect LSP mesh [15].

1.2.3 Shearography

Shearography is an optical method founded on speckle interferometry, for the non-contact measurement of material surface deformations [16]. A laser light is scattered from the test surface and passed through a shearing optic that splits the picture into two identical but displaced images before the image is focused on the detector. This is called the speckle pattern which is basically a gradient of the surface profile in the direction of observation. The image of an unstressed reference surface is recorded by an acquisition system. The inspected surface is then mechanically bent in order to increase the deformation around the defect. A second picture of the stressed surface is then captured. Finally, the difference of the stressed and unstressed plots is observed and reveals the deformation gradients, and by extension, allows the detection of defects. Since this is an optical technique and small defects on the wire mesh does not contribute to the deformation gradient this technique can not be applied as an evaluation method or LSP mesh.

1.2.4 Eddy currents

Eddy currents techniques are based on detection of coil impedance changes placed on top of the testing structure. The frequencies of operation are typically between 100 Hz and 10 MHz which limits the resolution of this method [17]. Attempts have been made to apply the eddy current technique at microwave frequencies, but they require cumbersome setups, and they

proved to be effective only with homogeneous conductive materials [18].

1.2.5 Microwave near-field imaging

Microwave and millimeter wave near-field imaging techniques using an open-ended waveguide [19], [20] could be a suitable NDE methods. A disadvantage of these techniques is that spatial resolution of images is in the order of the waveguide aperture size. So, resolving small defects requires using higher frequencies. For a resolution corresponding to typical LSP mesh size, frequencies in the millimeter-wave range would be required. Also, these techniques are sensitive to the orientation of the defects with respect to the probe E field. This sensitivity is undesirable for our LSP application.

The sensitivity to probe orientation and the need for expensive millimeter-wave hardware are avoided when using electrically small resonant probes operating at low microwave frequencies, as for instance in [21], [22], [23]. Implemented probes with different variants of split-ring resonators proved to be efficient in the detection of long and thin cracks in a homogeneous metal block, and provide resolution in the order of typically 0.1 mm along the crack width.

1.2.6 X-ray inspection

X-ray inspections of composites are conducted like those on metal structures. X-ray computer tomography (X-ray CT) method can produce high resolution images of the embedded flaws in composites. Moreover, it provides flaw depth information. Images are based on material density and it can also see some delaminations if set up at an angle. Water and inclusions can also be seen. The major disadvantages of this technique are that it is slow, expensive, bulky, and not suitable for on-line real-time inspection. Furthermore, the ionizing nature of the radiation limits its use and requires strict safety precautions. The X-ray technique consists basically on a source that radiates a sample and detectors on the opposite side. The source has a small focal spot size. Apertures at the source and detector limit the X-rays to a plane passing through the sample. The X-rays that goes through the sample are attenuated by the material located between the X-ray source spot and each detector element. The attenuated X-rays are detected by an array of detectors located on the other side of the sample. The sample is rotated in multiple positions in a way that the resulting measurements are manipulated by a computer to produce a 2D or 3D map of the attenuation. The resulting data corresponds to point-by-point density values on the cross section of the sample. This technique can reach spatial resolutions in the order of 1 µm and even below [24]. An example of X-ray images of the wire mesh extracted from [25] is presented in figure 1.7

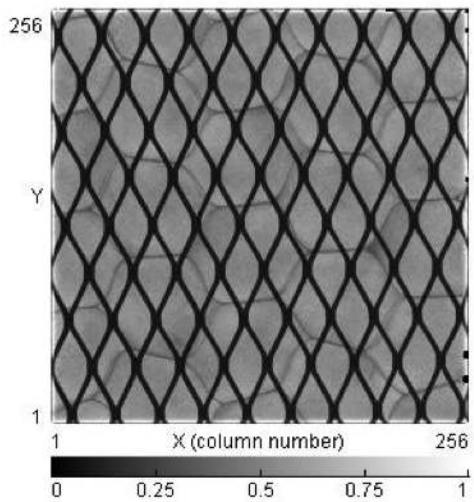

Figure 1.7 Transmission radiography of a composite specimen composed of paper honeycomb core and metal (copper) surface grid.

Even when the resolution of this technique is adequate to find defects in a wire mesh, the processing time may be an issue. A constraint between the sample size to resolution must be observed. It is clear that the resolution needs to be chosen on the basis of the length scale of the features under investigation. It was established in [26] that the sample must be no larger than 1000 to 2000 times the smallest feature size. As we will show in Chapter 3, strands that are cut by gaps in the order of 10 µm can been found in damage meshes which would implied according to [24] samples in the order of 10 mm. Considering that the goal of the present work is to be able to scan large surfaces, the applicability of X-ray for defect detection in aircraft is far from convenient.

1.3 Near field microwave microscopy

Microwave microscopy was initially proposed as a technique to overcome the limitations of classical optical microscopy. One of this limitations is well know as Abbe barrier or diffraction limit. As Abbe had calculated, no glass refinement or theoretical calculation about lens shape could overcome the diffraction barrier for visible light, which is about one-half microns. Optical instruments are restricted in their ability to distinguish between two objects separated by a lateral distance less than approximately half the wavelength. Early papers on microwave microscopy were looking for a way to beat the axiom that in order to increase resolving power it is necessary to decrease the wavelength or increase the numerical aperture of a lens.

In 1928 Synge [27] achieved a resolution of 10 nm by illuminating with a bright blue light a semi-transparent biological sample, using an aperture on a opaque screen. The signal recovering device was simply a photo-cell.

Zdenek Frait in 1959 [28] and Soohoo in 1962 [29] performed similar works measuring magnetic properties of material through ferromagnetic resonance. Instead of using the classical set-up where a ferromagnetic sample is placed inside a microwave cavity, they make a 1 mil hole at the bottom of a cavity and placed the sample underneath in a way that only the portion of the material directly opposite to the opening is exposed to the microwave radiation. They shifted this portion relatively to the hole to scan different regions of the sample. They measured the absorption curve (absorption vs H field) to derive material properties from resonance. Both works also increased the sensitivity of their measurements modulating the magnetic field with low frequency.

Closer to our time, Husain and Ash in 1975 [30] have achieved resolution in the order of $\lambda/200$ by illuminating a sample with a 1 GHz frequency signal through a 1 mm circular aperture. They introduced many of the techniques later used by others. They essentially measured the perturbation in the resonant frequency of a microstrip resonator. They also vibrated the sample at low frequency in order to increase the signal-to-noise ratio.

Most of the previously mentioned works described this technique as super-resolution or ultra-microscopy because the resolution obtained was orders of magnitude smaller than the free-space wavelength. The basic principle consists in illuminating an object with evanescent fields that are obtained in the neighborhood of a small aperture. The relative position of the object under the aperture is changed and a "pixel by pixel" image can be obtained. The signal recovered allows to construct images with resolution in the order of the aperture size.

The field of microwave microscopy flourished during the nineties, settling the basis for many of nowadays applications. In early 1990s Tabib-Azar [31] used a microstrip quater-wavelength resonator to characterize semiconductors with a resolution of $\lambda/1000$. In the late 1990s, the same group claimed a resolution in the order of $\lambda/750000$ [32] while detecting material nonuniformities.

Steinhauer's research group was also very prolific in this field [33–36]. All their papers basically share the same set-up configuration that consists of a long coaxial cable as a resonator, an open-ended coaxial probe, diode detector and lock-in amplifier in a frequency following circuit construction.

In one of their first papers [33] they measured frequency shifts to produce images of surface resistance in the range of $20\,\Omega/\square$ to $200\,\Omega/\square$. They employed a frequency following circuit

set-up that is configured centered at 7.5 GHz and a 480 µm center conductor coaxial probe. In [34] they construct quantitative imaging of sheet resistance of metallic thin film using the same set-up. They achieved $\lambda/80$ spatial resolution using a probe 500 µm diameter center conductor probe. In this case they also measured the quality factor to separate the effects of sample sheet resistance and topography. Again, in [35] with the same set-up they obtained quantitative topographic images of a metallic surface. This paper highlighted the importance of the separation between the tip of the probe an the sample. The technique allows a resolution of 55 nm with a 10 GHz center frequency.

1.4 Goals and Motivation

Considering the importance of LSP protection in new composite aircraft, a quantitative periodic evaluation of such structures is of primary concern. Until now, the author could not find any technique that can effectively resolve damage in such structures with the resolution required by aircraft manufacturers. As an example, Bombardier Aerospace has the following specification related to expanded copper foiled mesh installation: "The material shall be free from stains, discolorations or burnishing marks. The material shall not have more than 3 broken strands per square inch, 12 per square feet and 30 per 3 linear feet." Heretofore, there is no method or device capable of assessing this kind of material flaws.

It has been demonstrated that microwave microscopy is an effective technique to perform quantitative imaging of material properties, such as conductivity and dielectric constant. The simplicity of the detected signal interpretation is one of the most important advantages of near-field microwave microscopy. At the same time, it improves imaging resolutions by orders of magnitude smaller than the free-space wavelength of the radiation.

The initial motivation of this work is to modify and extend the capabilities of microwave microscopy in order to make the technique applicable in aircraft large surfaces. New probes and probe arrays that can resolve defects with the level of detailed required by the industry in this field have been designed.

1.5 Thesis Contributions

This work presents a new application of microwave microscopy for the diagnostic of the painted lightning strike protection (LSP) mesh used in composite aircraft skin. New flexible probes are presented. These probes are able to sweep over the surface of the composite skin and detect breaks in the LSP laying underneath. With this new approach it is possible to resolve defects as small as one cut strand under the paint. Gaps in the wire mesh smaller than

100 µm and under a stack made of a 350 µm layer of paint and a 125 µm layer of dielectric tape can be successfully identified.

This technique features the possibility to measure the paint thickness with a resolution in the order of micrometers. It is demonstrated that the paint thickness resolution is directly related to the capability of the VNA to discriminate frequency displacements. Considering that our experimental set-up resolution is 1 kHz, the resolution of paint thickness measurements is 1.6 µm.

The other contributions are related to the speed of the process. An interpolation method has been optimized to speed up measurements of the quality factor with just a few measurement points. Pursuing the same objective, an array of probes has been developed to speed-up the process aiming its applicability in the inspection of large surfaces. Applying these methods, the scanning time per cm^2 was reduced from 16 minutes to 2.7 minutes.

CHAPTER 2 ELECTRIC PROBE

2.1 Introduction

As discussed in Chapter 1, microwave microscopy has been proposed as a technique to solve the problem of finding damage or flaws in the LSP mesh [33–36]. It was already shown that microwave microscopy can overcome the Abbe barrier and resolve defects much smaller than the radiation wavelength. The high resolution and low frequency of this technique would allow us to detect small flaws that other techniques are not able to detect at the present time. Also, the simplicity and straightforward interpretation of the detected signal are important for planing a future portable device which could potentially be used for in-service evaluation of damaged materials. We explore in this chapter the potential of electric probes to solve the problem that has been exposed in the previous chapter. In particular, we investigate the ability to discriminate thin copper traces over composite; exposed and under the paint. Also, we explore the ability to detect broken strands.

The well-know basic principle of microwave microscopy consists in (see [37, 38]) illuminating a sample with a near-field or an evanescent field probe. The size of the probe has to be small, as it is directly related to the spatial resolution of the microscope image. This radiation interacts with the sample in a way that part of it is dissipated in the sample, reflected back in the probe feeding line or scattered away. The signal reflected by the probe contains detailed information about very localized properties of the sample and it can be used to construct an image of the sample as a function of the probe height and position. The source of the evanescent fields is typically a sub-wavelength antenna. In our case, we construct a probe from an open-ended micro-coaxial line which is exited by a network analyzer at a frequency of 1 GHz. The coaxial probe is located at the end of a low loss coaxial line resonator coupled to a source by a tunable reactive element. A tuner made of coaxial lines with sliding contacts is used in our experimental set-up (see Fig. 2.1). The return loss vs frequency curve of the resonator exhibits sharp resonances (see Fig. 2.4a). Focusing on one of the resonances (Fig. 2.4b), we scan the probe at a fixed distance from the sample, and we record the frequency response for every position. The recorded response provides us with two streams of information i.e. frequency shifts of resonances and quality factor. By post-processing this data, we can extract the significant information and build the wire mesh images that allow us to identify faults.

2.1.1 Equivalent circuit.

The starting point is the experimental arrangement used by Steinhauer [35] in a simplified fashion. Instead of using a frequency following circuit to measure the return power we simply use a vector network analyzer (VNA) as a source and detector. A schematic of the experimental set-up is shown in Fig. 2.1.

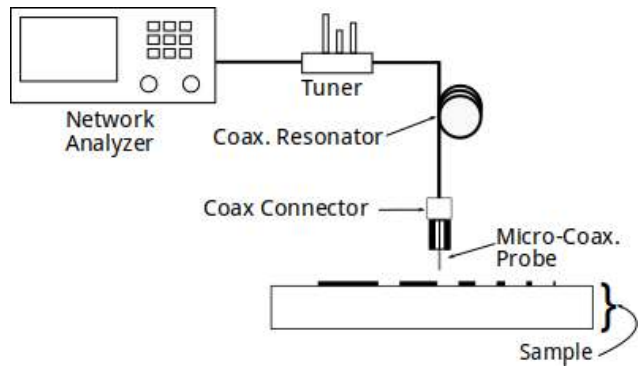

Figure 2.1 Schematic of the experimental set-up.

Simulation of an equivalent circuit model is useful to illustrate the behavior of the set-up in presence of a wire mesh. As illustrated in Fig. 2.2, a microwave source excites a coaxial transmission line resonator through a coupling capacitor. The coupling capacitor, C_c, represents the tuner in the experimental set-up of Fig 2.1. This capacitor was set to a value of 1 pF. The justification of this value is given in the Section 2.5, where a full wave simulation has been performed for a CPW probe. The circuit was simulated in *Keysight-ADS®* software. In the model, where C_c was adjusted in order to have a good match between simulations and measured S_{11} responses. The coaxial line is terminated by an open-ended coaxial probe that is interacting with the sample. In Fig. 2.3 a model of the interaction between the probe and the sample is presented. The capacitance between the center conductor of the probe and the sample is represented by C_x. C_x is determined by

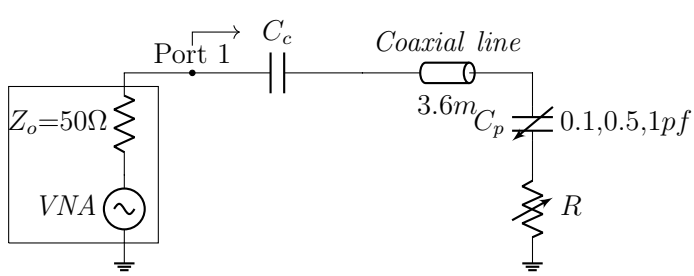

Figure 2.2 Set-up simplified model.

the area of the center conductor and separation from the sample. In the same fashion, C_o models the outer conductor capacitance. Z_s is the impedance of the sample. The real part of Z_s is related to the microwave surface resistance of the sample. Parameters C_0, C_x and Z_s determine the shifts in the resonator resonant frequency that will allow us to later detect defects in the material. In the simulation circuit model of Fig. 2.2, C_0 and C_x are represented by C_p, and R models the sample surface resistance. The series resistance R represents losses in the sample; we consider them negligible in this section.

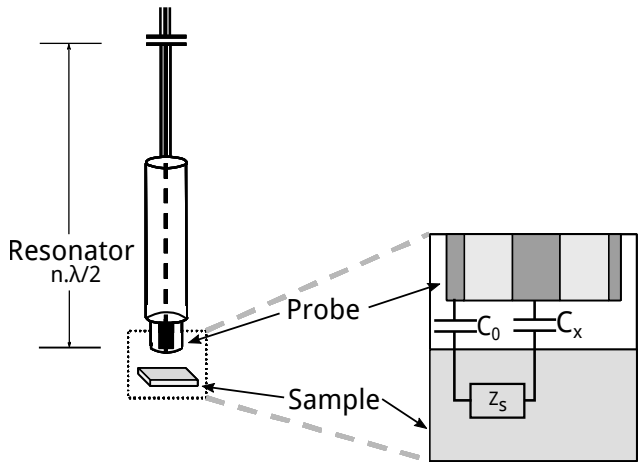

Figure 2.3 Sample-tip lumped element model.

Strong reflections at both ends of the line cause resonances. Since $R = 0$ was assumed, the return loss is uniquely due to dissipation in the coaxial line. The plot of S_{11} parameter for three values of probe capacitance C_p, i.e. 0.1 pF, 0.5 pF, 1 pF and no losses (R=0 Ω) are presented in Fig. 2.4. The resonance frequency is shifted down with increasing values of capacitance. Increasing probe capacitance is equivalent to lengthening the coaxial transmission line which leads to lower resonance frequencies. A semi-rigid coaxial cable *Micro-coax* UT-141C-LL was used in the experiments. According to its specifications, losses of 0.3 dB m^{-1} were considered in the coaxial line model, and a real characteristic impedance of 50 Ω was assumed. Notice that large variation of C_p values were used in the simulations to emphasize frequency shifts. As it will be shown in section 2.5, the probe capacitance changes are much smaller.

In a Smith chart representation of S_{11}, sharp resonances are mapped as "Q-circles" [39] . When C_p increases, points at a given frequencies will rotate in such a way that the Q-circle is almost entirely rotated clockwise, overlapping itself in part. Because the losses are constant, all the points are constrained to the same Q circle (see Fig. 2.5). Probe and sample losses could be included in the model with a resistor in series with the capacitor. For this situation,

there will be a new Q circle for each new resistor value. Further explanations of this situation will be given in the next chapter where a magnetic probe is introduced.

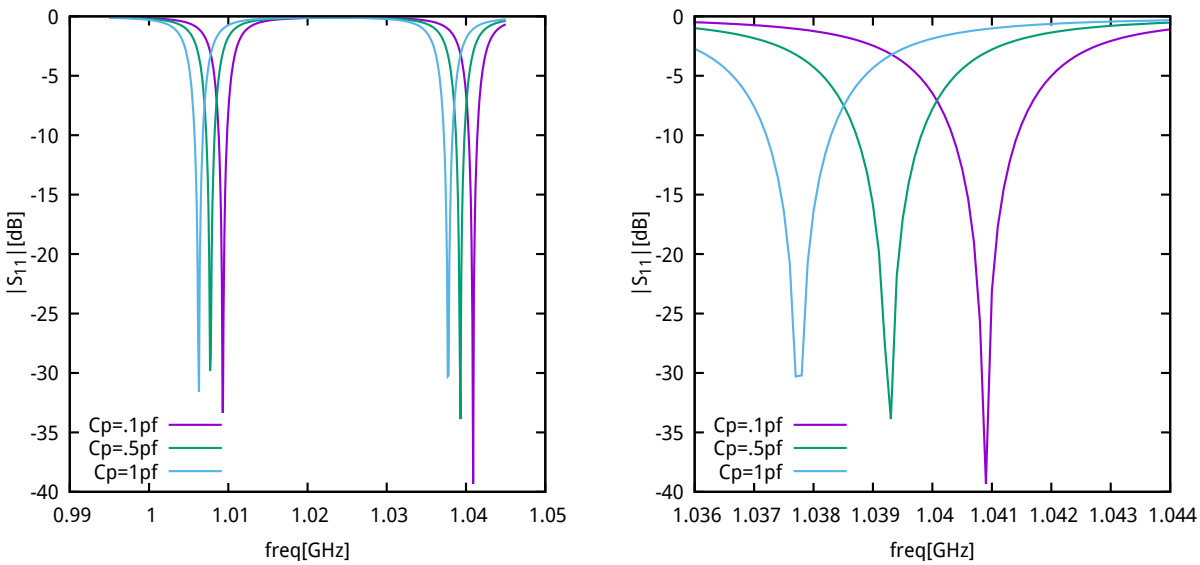

(a) (b)

Figure 2.4 $|S_{11}|$ circuit response for C_p=0.1, 0.5 and 1 pF and R =0 Ω. (a) 2 resonant modes. (b) one resonant mode.

2.2 Experimental set-up

In the following sections we explore qualitatively the principles of microwave-microscopy with a basic set-up. We describe the use of a microwave microscope with an open-ended coaxial probe to map dielectric and metal surfaces.

The experimental set-up follows the schematic circuit presented in Fig. 2.1. The key element is a 3.6 meter-long resonant coaxial transmission line. One end of the line is connected to an open-ended micro-coaxial probe and the other is weakly coupled to a microwave source (VNA), via a piston tuner. The probe is made with Pasternack semi-rigid coax cable with 0.94 mm outer diameter and 0.28 mm inner diameter. Since there is no off-the-shelf connector for a micro-coaxial cable a transition has been designed. This transition is simply a 50Ω grounded coplanar waveguide (CPW) where a PCB SMA edge launcher connector is soldered (see Fig. 2.6). The micro-coaxial cable inner conductor is soldered on the center conductor of the grounded CPW line. The substrate that was utilized in the design was Rogers RO4003C with 60*mil* of thickness. Rows of vias are implemented on the two edges of the substrate to

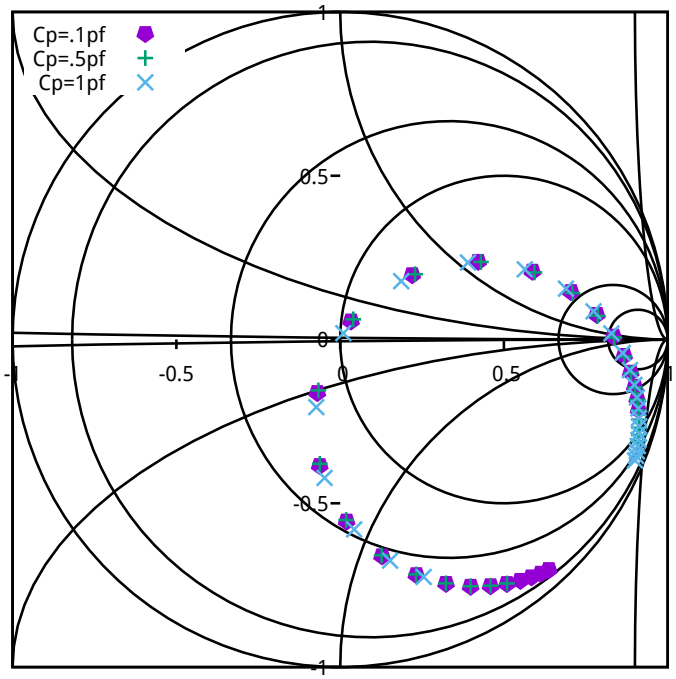

Figure 2.5 Smith chart representation of S_{11} for C_p=0.1, 0.5 and 1 pF and R =0 Ω.

ensure ground continuity with the micro-coax outer surface.

The probe was installed in the experimental set-up shown in Fig. 2.7. This set-up includes an x-y translation stage that is capable of displacements in the order of 1 µm in the two axes. Narrow-band measurements have been performed over FR4 glass-epoxy substrate. Two samples have been prepared. One with all the copper etched from the top surface, and second one with all copper intact in both surfaces. In a third measurement the slab was removed keeping the probe in the same position. This measurement was labeled "No-sample", and it corresponds to the smallest possible capacitance at the probe tip. The probe was positioned vertically above the center of the samples as close as possible to the sample without measuring the probe-sample distance separation (naked eye, around 0.25 mm). The measured S_{11} curves for three cases are plotted in Fig. 2.8. As it was expected, the resonant frequency decreases with the increase of capacitance. The capacitance is higher with a dielectric sample compared to a no-sample situation and even higher with the fully metalized sample. The measured frequency shift of the resonance was 12 kHz between the dielectric and metalized samples.

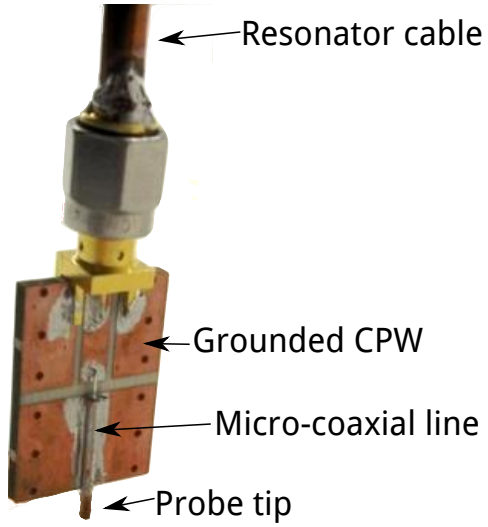

Figure 2.6 Micro-coax probe and CPW transition.

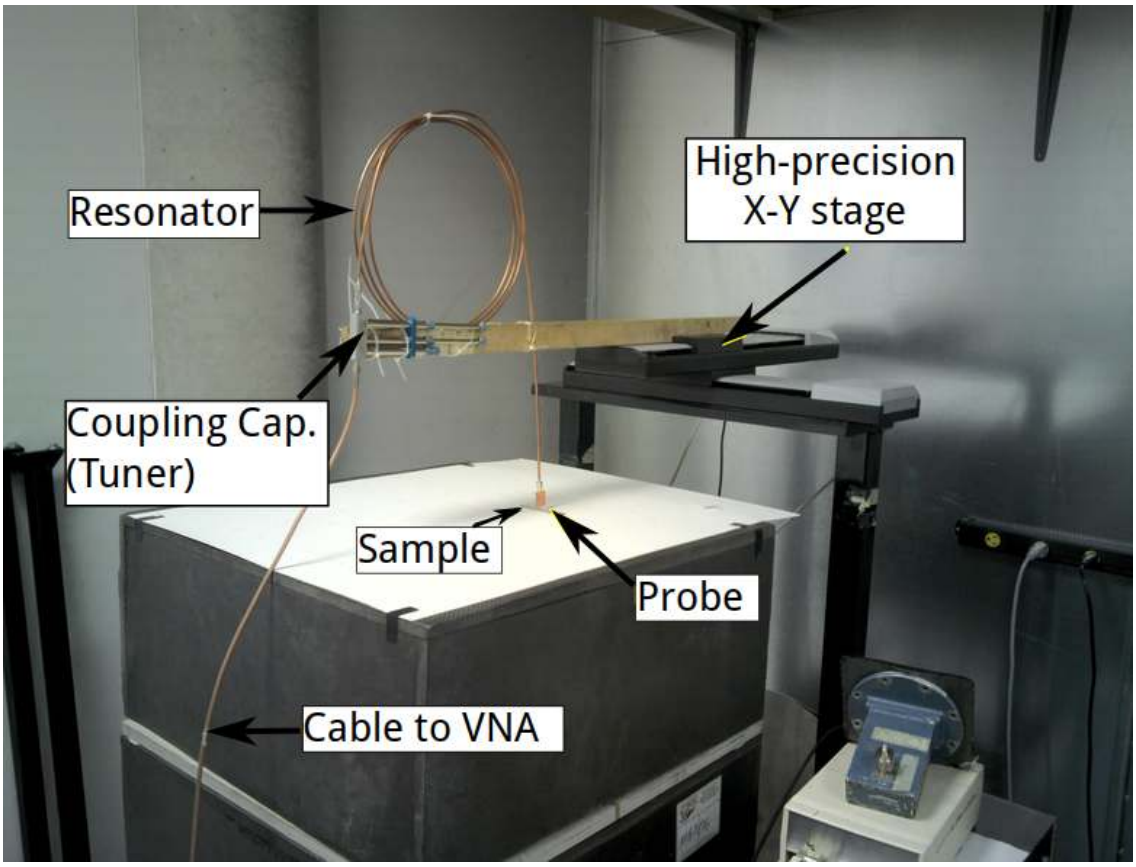

Figure 2.7 Experimental set-up.

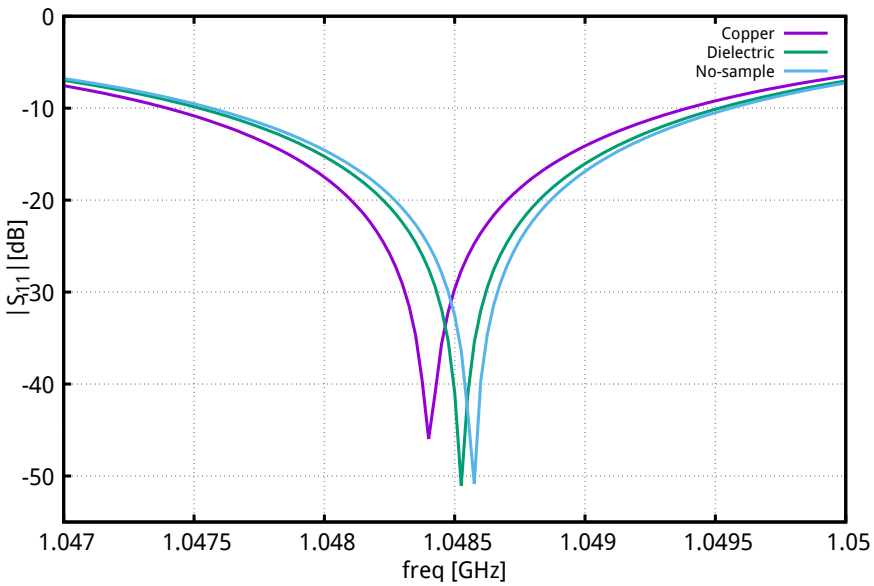

Figure 2.8 Micro-coax probe measurements. Grounded dielectric sample, copper and no-sample.

2.3 Width gauge

In the first exploratory experiment it was observed that the sensitivity of the set-up allowed to distinguish between dielectric and metallic samples. In this section, we intend to estimate the spatial resolution of the system. To quantitatively demonstrate the capabilities of the system we scanned the probe over a pattern of copper traces, along a line perpendicular to the traces. We designed a gauge (see Fig. 2.9) composed of printed traces that vary in width, namely 10.1 mm (400*mil*), 5.08 mm (200*mil*), 2.54 mm (100*mil*), 1.25 mm (50*mil*), 0.762 mm (30*mil*), 0.508 mm (20*mil*), 0.252 mm (10*mil*), 0.125 mm (5*mil*) and 4 traces of 0.076 mm (3*mil*). The spatial resolution can be deduced from the image profile of the narrowest lines. In addition, a computer running *Labview*® is in charge of commanding the step motors responsible for the probe movement. It also triggers the VNA (*HP 8510C*) in each position and save the S_{11} curve afterwards.

To determine the spatial resolution of the system, the probe was placed very close to the sample. The distance between probe and sample was not measured precisely but it was estimated between 0.25 mm and 0.50 mm. The probe swept the sample over a path perpendicular to the traces in steps of 0.1 mm covering all strips on the sample (100 mm). The VNA measurement windows was set to a frequency of 1.045 GHz, a span of 30 MHz and 200 measurement points. For each position of the probe the computer records a S_{11} curve. Fig.

2.10 shows 1000 recorded curves. The inset in the same figure shows the variation of S_{11} at 1.047 55 GHz while the probe moves through the different traces. The same reference frequency (1.047 55 GHz) was used to build the plot in in Fig. 2.11. It is clear that the system is able to discriminate between metalized and non-metallized parts of the substrate even if the S_{11} difference between metallized and non-metallized is limited to 1 dB for the thinnest traces (76 µm). Moreover, since only two of the thinnest traces were detected out of 5, it can be inferred the scan steps of 0.1 mm is larger than the trace and so the probe could have jumped over it. In other series of tests under the same condition but with different probe starting point those traces were detected.

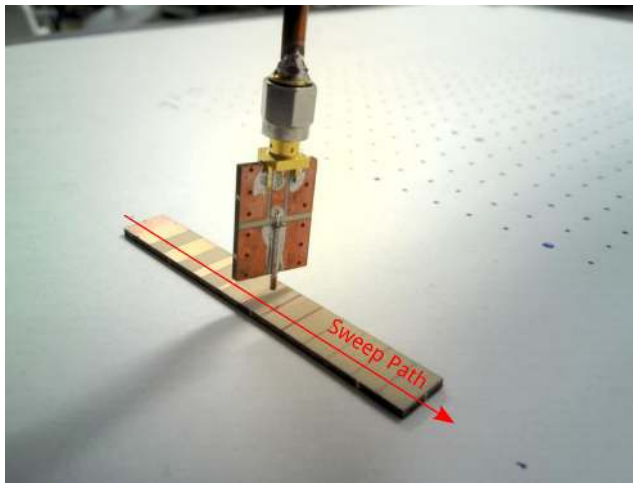

Figure 2.9 Strip width gauge.

2.4 Grooves gauge

Ultimately, the goal of this work is to identify broken strands in a metallic wire mesh. In this section we explore the ability of the proposed microscope to detect slots of different widths practiced in a copper plane. (see Fig. 2.12) Similarly to the previous experiment, slots were etched on alumina substrate from 50.8 µm to 254 µm width in 25.4 µm steps. The probe was placed as close as possible to the sample and moved over the sample in a path perpendicular to the slots orientation, starting near the narrowest slot and ending on the right 254 µm slot. During measurements, we were not able to detect any change in S_{11} as in the previous section. The VNA setting (span, center frequency and number of points) were the same as in the previous section. As mentioned before, the inner diameter of the micro-coax constituting the probe is 280 µm, which is much larger than the widths of all the slots. The probe scanning the widest slot (254 µm) is showed as inset in Fig. 2.13. Clearly,

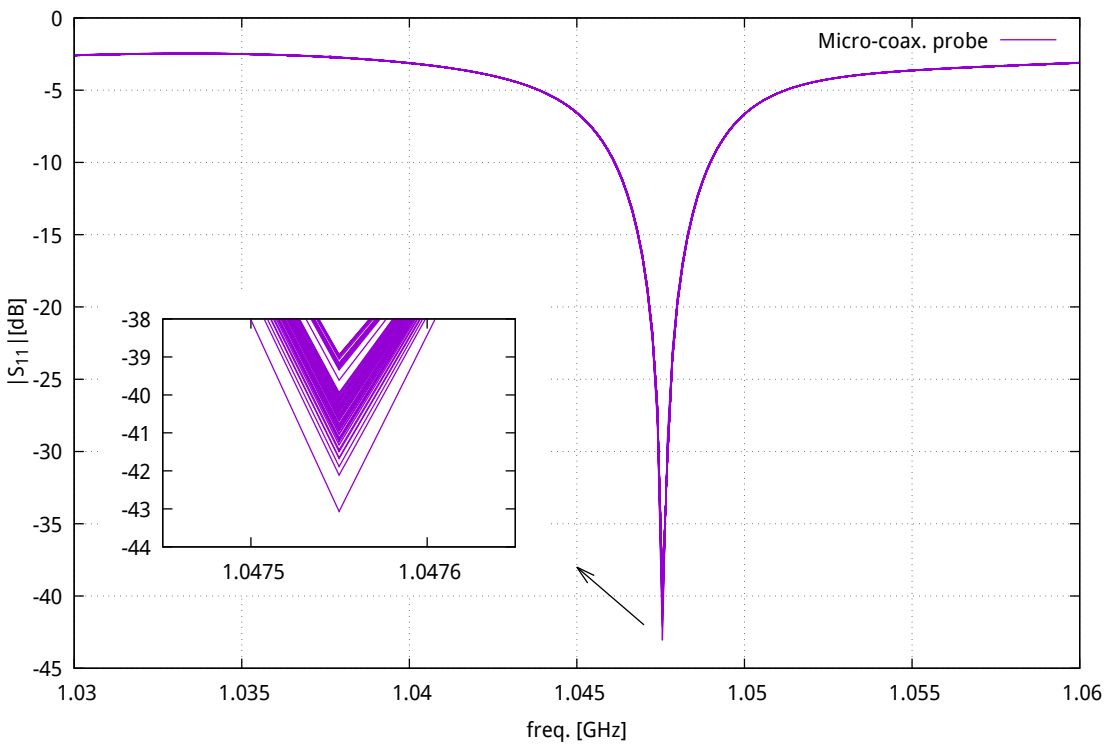

Figure 2.10 Measuread $|S_{11}|$ every 0.1 mm over a path length of 100 mm.

the probe tip is on the same order of magnitude as the slot and the outer probe diameter is almost 4 times the slot width, which makes the slots undetectable.

Moreover, a problem has been identified related to the probe-sample distance. As seen in Fig. 2.14, measurements have been taken in two points near to the left and right edges of the sample. These points are label $Pos1$ and $Pos2$ in Fig. 2.13. Since, the copper layer has not been etched on those areas, one would expect identical curves at the two positions. However, different resonance curves are obtained as illustrated in Fig. 2.14. The differences between the resonance frequencies is of 20 kHz. In comparison, the shift in resonance frequency between the metal and dielectric surfaces reported in section 2.2 is in the range of 10 kHz. A possible explanation for this 20 kHz shift could be a variation of the probe-to-sample distance during the scan from $Pos1$ to $Pos2$. Taking into account this hypothesis, a probe-to-sample distance control mechanism has been developed to correct the aforementioned problem.

Two actions has been taken in order to improve the set-up without changing any of the components. As demonstrated in multiple previous works [33, 35], the smallest resolvable feature is determined by size of the probe tip. Firstly, the probe tip has been sharpened into a conical shape at an angle of 45° in order to concentrate the electric field flux in a small volume close to the tip. Secondly, a distance control mechanism has been implemented. An

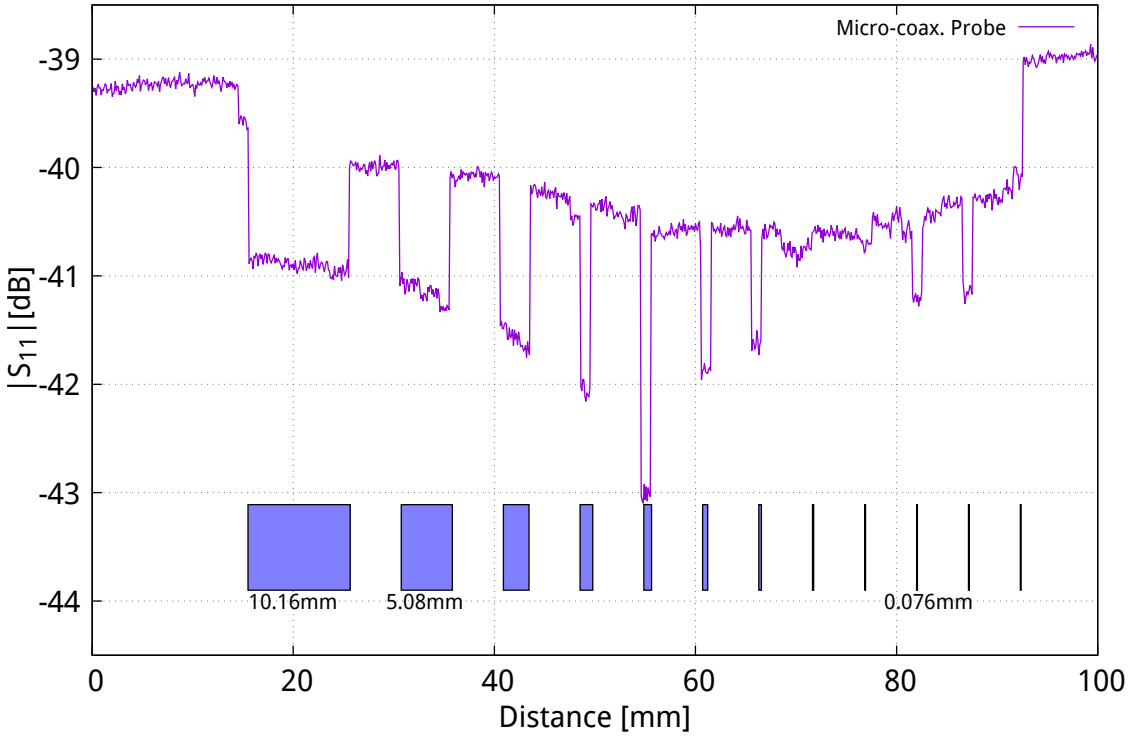

Figure 2.11 Width gauge measurement. Probe displacement steps of 0.1 mm. The blue regions in the test samples are metallized.

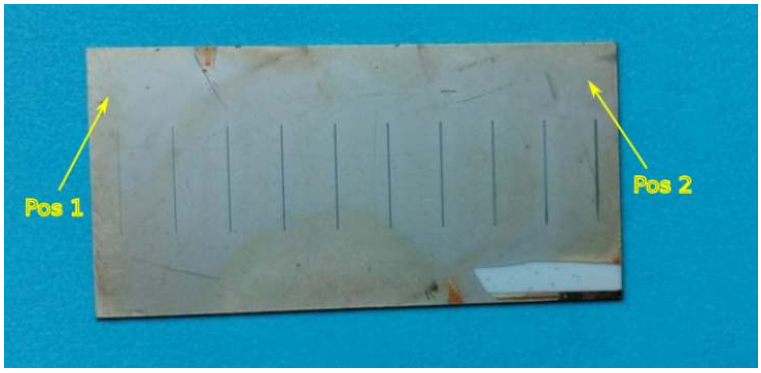

Figure 2.12 Alumina substrate with slots 50.8 µm to 254 µm - 25 µm steps.

image of the sharpened probe is shown in Fig. 2.15. For comparison purposes, a microscopic image of the probe has been taken near a 127 µm slot (see Fig. 2.16)

Near field simulations have been carried out to compare how near field is spread over the sample. A method of moments (MoM) simulator (*Feko*®) has been used fo this purpose (see Fig. 2.17). Two different cases have been considered where the probe is separated by a distance of 100 µm from a piece of substrate *Rogers RO*4003*C*. In case a) the inner and

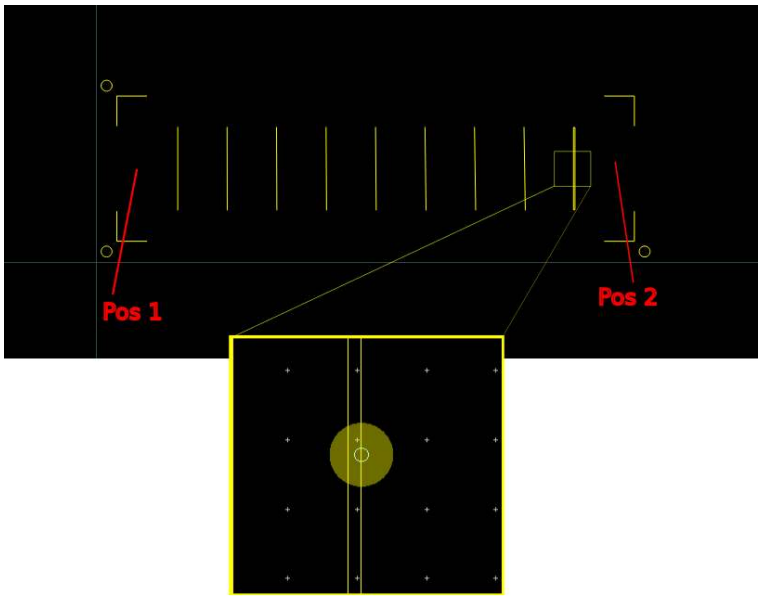

Figure 2.13 Alumina slots. Probe over 254 µm slot.

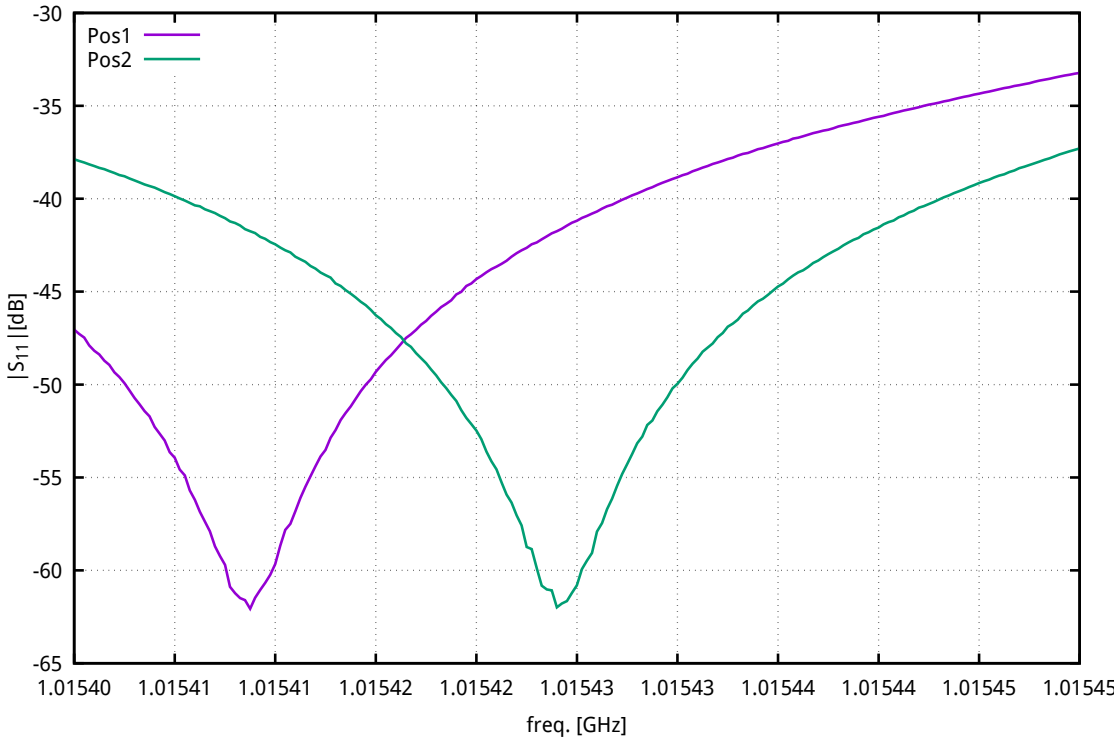

Figure 2.14 Measurements for $Pos1$ and $Pos2$ positions.

outer conductor are of equal length (representing no sharpening). In b) the probe has been sharpened into a conical shape of 45°. In both cases, the outer and inner conductor of the

probe are simulated as perfect electric conductor. The field inside the sample is calculated at 1 GHz using finite element method (FEM). Figures 2.18 a) and b) shows the results of these two cases. The normalized electric field magnitude is displayed. The geometrical scales are the same for the two figures. It is observed the increase in concentration of near electric field around the inner conductor in image b) in comparison with image a). Notice that due to discrete meshing of the inner conductor, electric fields appears to exist inside the PEC inner conductor. The effect is mostly noticeable in case a).

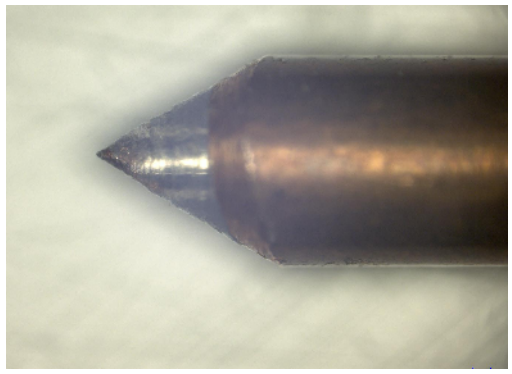

Figure 2.15 Sharpened micro-coaxial tip.

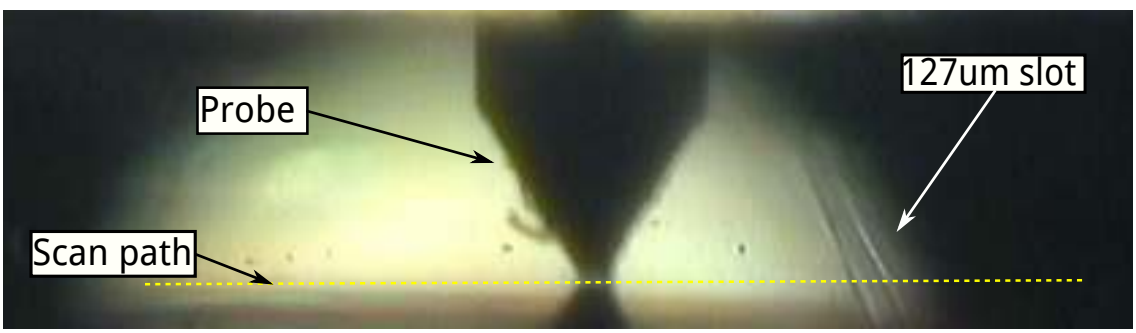

Figure 2.16 Sharpened micro-coaxial tip scanning 127 µm width slot

The mechanism of distance control includes a marble base and a piece of plexyglas with three screws that allow us to level the sample. (See fig. 2.19). In addition, the use a dial indicator (model *Mitutoyo 2417S*), with a resolution of 254 µm (10mil) was utilized to measure the lift off distance at both extreme sides of the sample. By using level screws and dial indicator, it was possible to level the sample so the point labeled $Pos1$ and $Pos2$ (see Fig. 2.12) presents the same height. At the same time, the probe-sample separation was set to 508 µm.

The two aforementioned actions did not provide the expected corrections. In Fig. 2.20 we scan the same slotted sample presented before. The VNA span was set 200 kHz and 1600

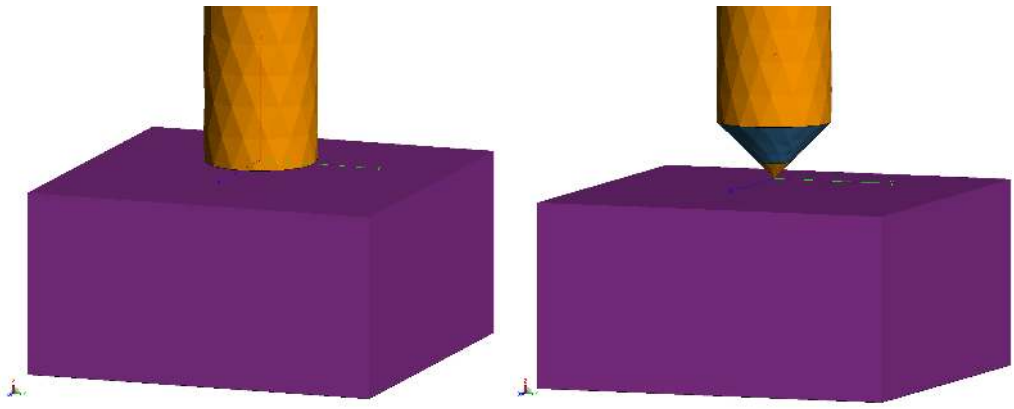

(a) (b)

Figure 2.17 Near field simulation models.

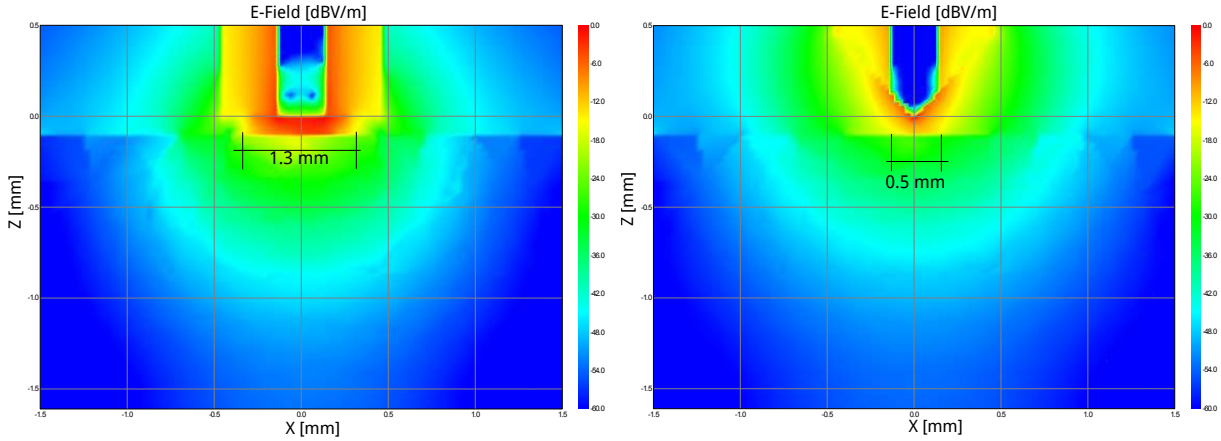

(a) (b)

Figure 2.18 Near E field magnitude distribution at 1 GHz.

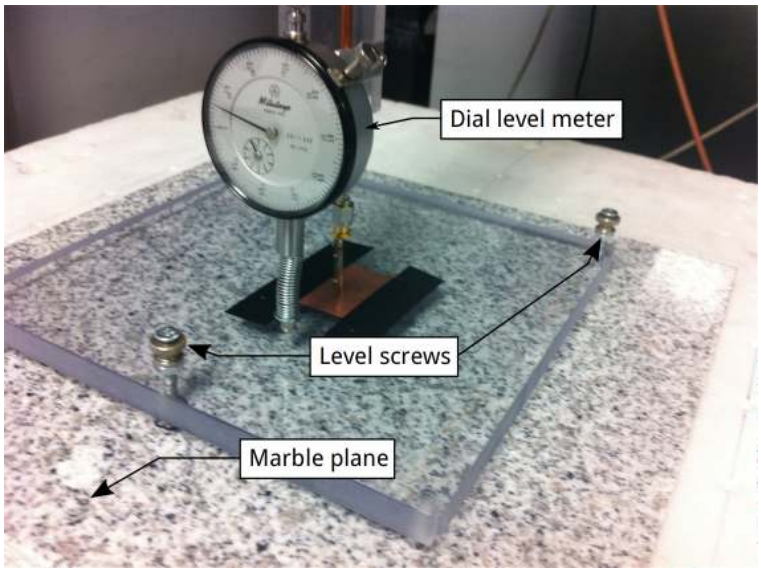

Figure 2.19 Lift-off distance control.

points of frequency were used. The curves that represent measurements at points $Pos1$ and $Pos2$ are not identical, as it would be expected. The problem still persists but the height control mechanism reduce the difference between resonance frequencies of both curves to 10 kHz (previously 20 kHz). Also, on a positive note, the new set-up did improve the detection of the 3 widest slots (see inset in fig 2.20). These curves also presents errors. As the widths of the slots decrease, it would be expected that the resonance frequency was shifted toward lower frequencies. The resonance frequency of the 228 µm slot is higher than the one that corresponds to the 254 µm which is inconsistent with theory. These errors would be also consequence of the primitive sample-distance control mechanism that would not provide enough precision for the pretended application. In brief, it has been identified the probe-sample separation as a critical variable in the presented measurement set-up. A new straightforward method is presented in the next section that aims to solve the problem.

2.5 Coplanar waveguide probe

Having strong indications on how sensitive the system is to the probe-sample separation parameter; a more stable, simple and straightforward approach has been taken. A new probe printed on a flexible substrate has been designed. The purpose of this design is to avoid cumbersome distance control mechanisms traditionally used on microwave microscopes (see [32, 40]). The principle is that the flexible probe substrate can bend and stay in contact with the sample as it slides over it, keeping the separation distance constant. Probes and

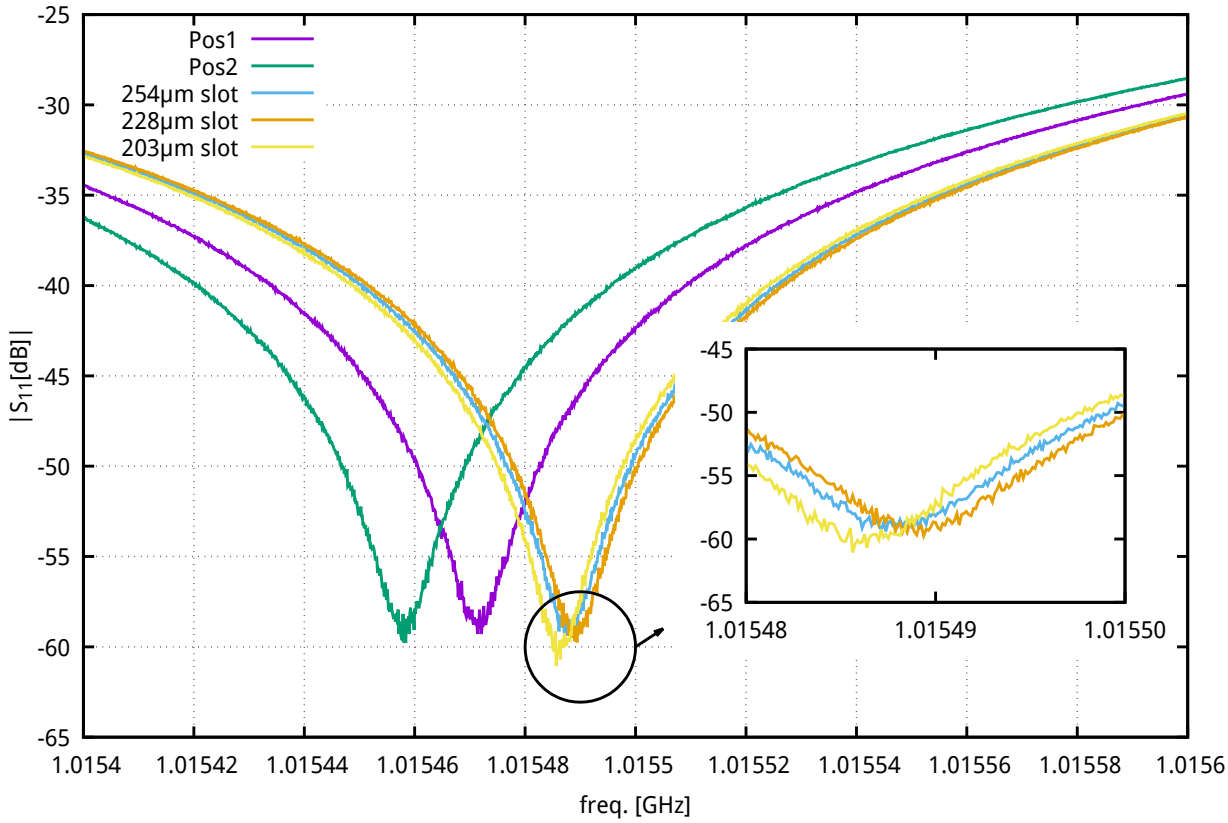

Figure 2.20 Measurements of the probe scanning 254 µm, 228 µm and 203 µm Slots, *Pos*1 and *Pos*2 points.

resonators made of strip lines were already used in microwave microscopy by precisely controlling the probe-sample separation distance in the same manner as for coaxial probes [41]. As mentioned earlier, these distance-controlling techniques are not suitable for our application due to their complexity and low speed. So, it was chosen to use the same substrate that support the printed transmission line as a fixing mechanism to control probe-sample separation. Moreover, instead of using a microstrip we choose to use a grounded CPW as it is less prone to radiate and has higher isolation than microstrips.

In the first attempt, the purpose of the design was to have maximum flexibility in a way that the probe could adapt to the scanned sample surface. Also, it is desirable minimize the separation of the sample to increase near fields interaction. The chosen substrate was a 12.7 µm (0.5 mil) *Dupont LF7012R* because it is one of the thinnest flexible substrates available. Given that the probe is placed at the end of a 50Ω coaxial transmission line, it was also designed to have the same characteristic impedance. The design was carried out according to the formulation in [42]. Simulation of this structure at a relative low frequency are not trivial. 3D simulators like *Feko* and *HFSS* fail in calculating the Green function for such electrically thin layered substrate, even when setting the engine to double precision. As a result, the first probes were designed using *ADS Momentum*, a 2.5D simulator. A 600 µm center strip separated from the ground by two 50 µm gaps constitutes a 50Ω impedance according to calculations and later verification by simulations. The probes constitute a simple open-ended CPW transmission line as shown in Fig. 2.21. Pictures showing the fabricated probe with a transition end launch connector are shown in Fig 2.22. Due to the low width of the center strip line and the reduced thickness of the substrate, the copper on the strip (17.78 µm thick) had the tendency to break easily. The probe was almost impossible to manage.

In a second attempt, several mechanical tests on different substrate thicknesses were performed. A 127 µm (5mil) thick substrate was chosen for the new probe. As the thickness increases substantially in respect to the previous substrate, we were able to simulate a 50Ω CPW line with 3D simulators. The proposed CPW belongs to the category of aperture-based probes [43]. It features a 1 mm center strip separated by a 152 µm narrow gap from the ground plane which translates in a 50Ω characteristic impedance. Since the gaps are very small, two regions of highly concentrated fringing field are created to interact with the sample. This interaction will alter the resonant frequency when there is a change in the sample conductivity under any of these areas. Taking into account the previous considerations, we can consider the footprint of the probe in the order of 1.32 mm, which is very large in terms of microwave microscopy. At the same time, the resolution is still in the order of 152 µm since this is the size of the apertures. To summarize, we can scan large surfaces searching for

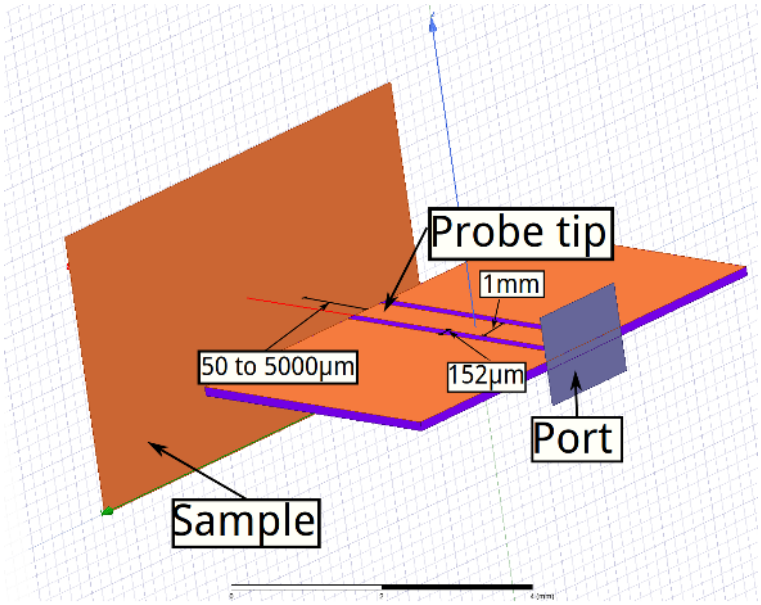

Figure 2.21 Open CPW on finite thickness substrate over sample.

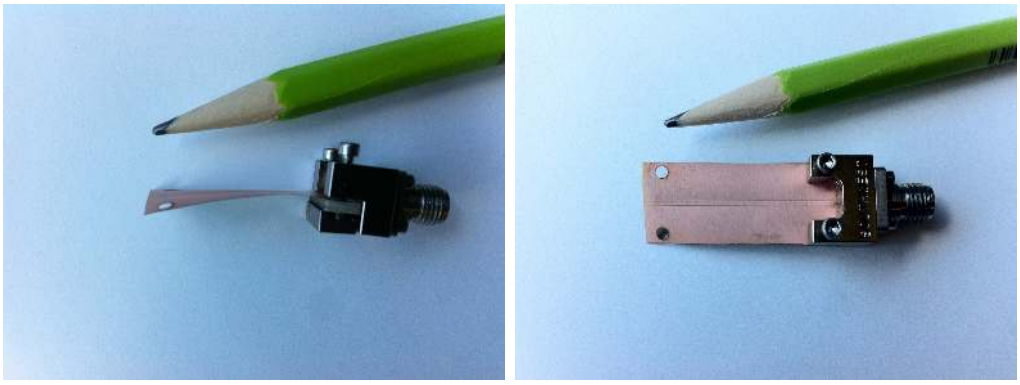

(a) (b)

Figure 2.22 Kapton CPW probe. 12.7 µm substrate. (a) Side view. (b) Top view.

little details.

We also performed the same simulation but with a CPW probe facing a PEC plane with *Ansys HFSS* . (See simulated model in Fig. 2.21). *Ansys HFSS* was used instead of *Feko* because finite element method technique (FEM) presents faster resolution for enclosed problems. The sample in this figure is simulated as PEC. Later, we use the S parameter extracted from the previous simulation into ADS simulation model that takes into account the coaxial cable and coupling capacitor. Fig. 2.23 shows resonance frequency variations on the order of 50 kHz when the probe separation increases from 50 µm to 5000 µm. Lastly, it was noticed that the resonance frequencies do not increase monotonically with separation distances for values higher than 500 µm. This is a consequence of simulation errors. The simulated structure is a very short piece of transmission line which roughly, in electrical terms, means $\lambda/50$ at 1 GHz simulation frequency. Simulator converge criteria settings, such as ΔS or $\Delta phase$, need to be very small to reach accurate results. As a consequence simulation time increases exponentially. It was considered purposeless to get accurate simulation results for such cases given that the principle of operation is verified by experiments in the next section.

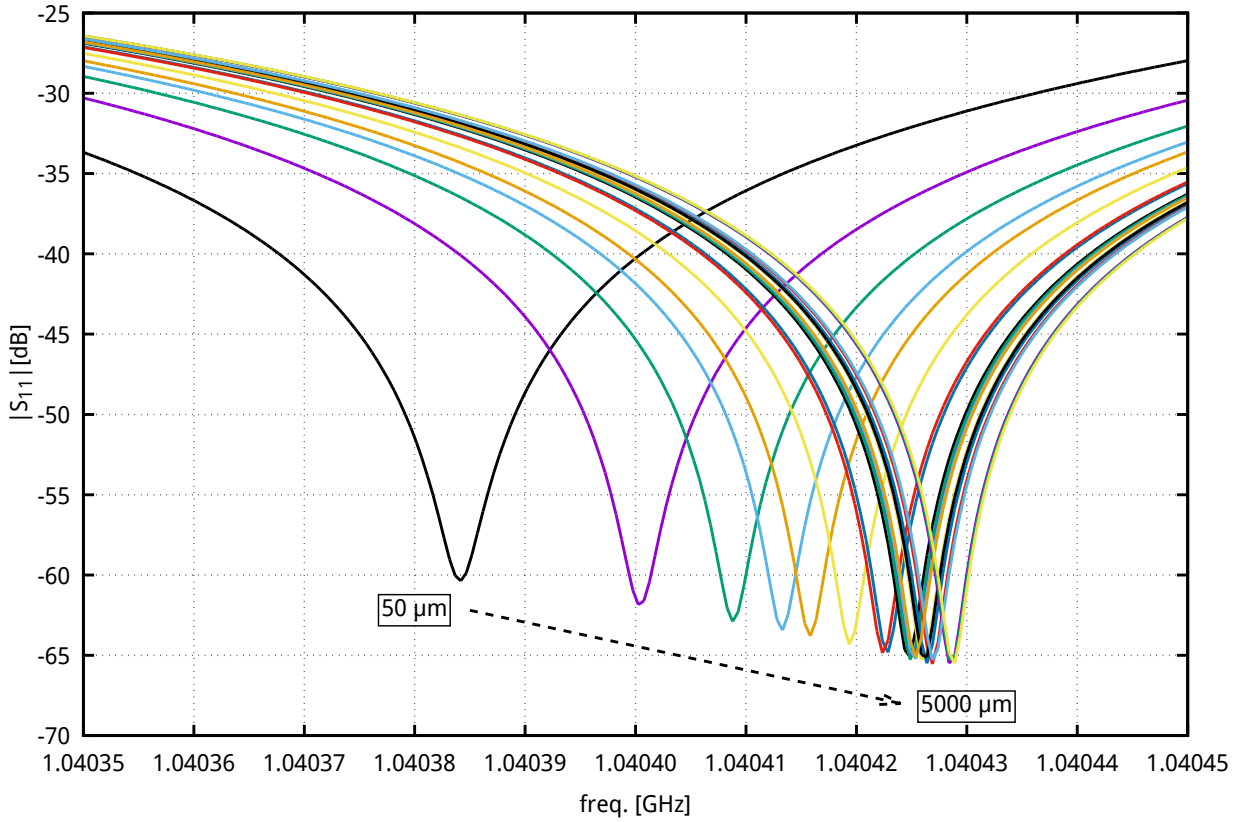

Figure 2.23 Simulated $|S_{11}|$ for probe-sample separation values of: 50, 100, 150, 200, 250, 350, 450, 550, 650, 750, 850, 950, 1050, 1150, 1350, 1550, 2000, 2500, 3000, 3500, 4000, 5000 µm.

2.5.1 CPW probe experimental results

Since the calculated CPW gap and strip width of the probe on the 5 mil substrate were very close to the fabrication PCB tolerances we have access at Poly-Grames, three different CPW probes with variable distances between the center line and ground plane, namely 152 µm, 177 µm, and 254 µm, have been fabricated to verify the consistency with calculations. We later measured S_{11} with a 50Ω chip resistor installed in one end of the CPW line. The results are shown in Fig. 2.24

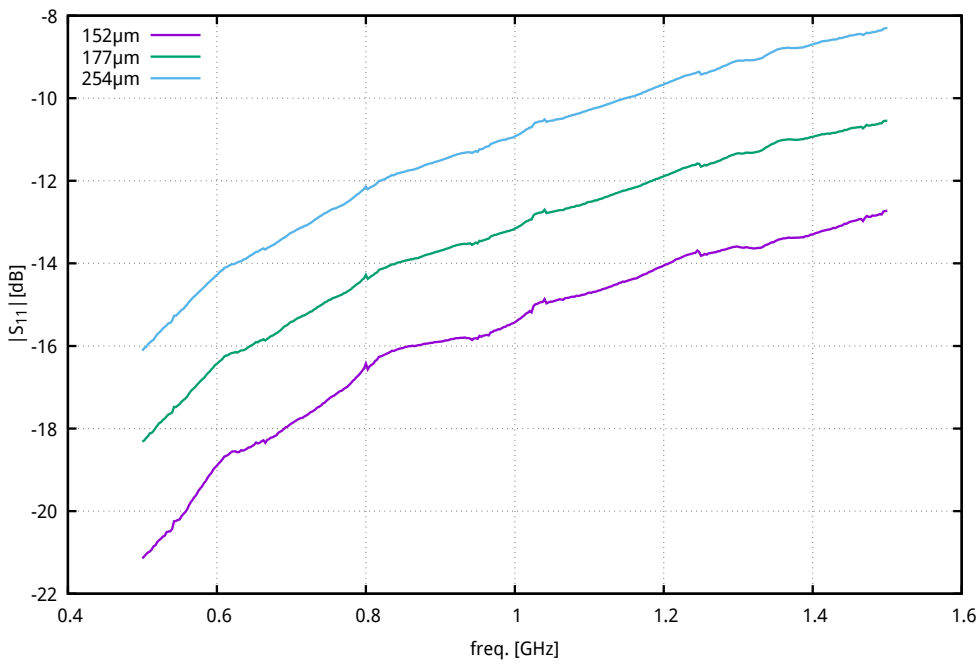

Figure 2.24 Probe $|S_{11}|$ measurements. Gap between center line and ground plane of 152, 177, and 254 µm.

Based on the previous results, the probe that presents a gap of 152 µm was chosen as the best candidate to be installed on the measurement set-up.

The next stage involves a sanity check to verify the correct behavior of the measurement set-up. The same simulated structure which results were presented in Fig. 2.23 was duplicated here using a probe station to accurately change the separation distance between probe and sample. The PEC sample sheet used before in simulations is represented now by piece of substrate with the unetched copper side placed towards the probe. The result of the experience is exhibited in Fig. 2.25.

It is observed that here the resonance frequencies shift monotonically towards high frequencies when the probe-sample distance increases; as expected. Also, the bandwidth covered by

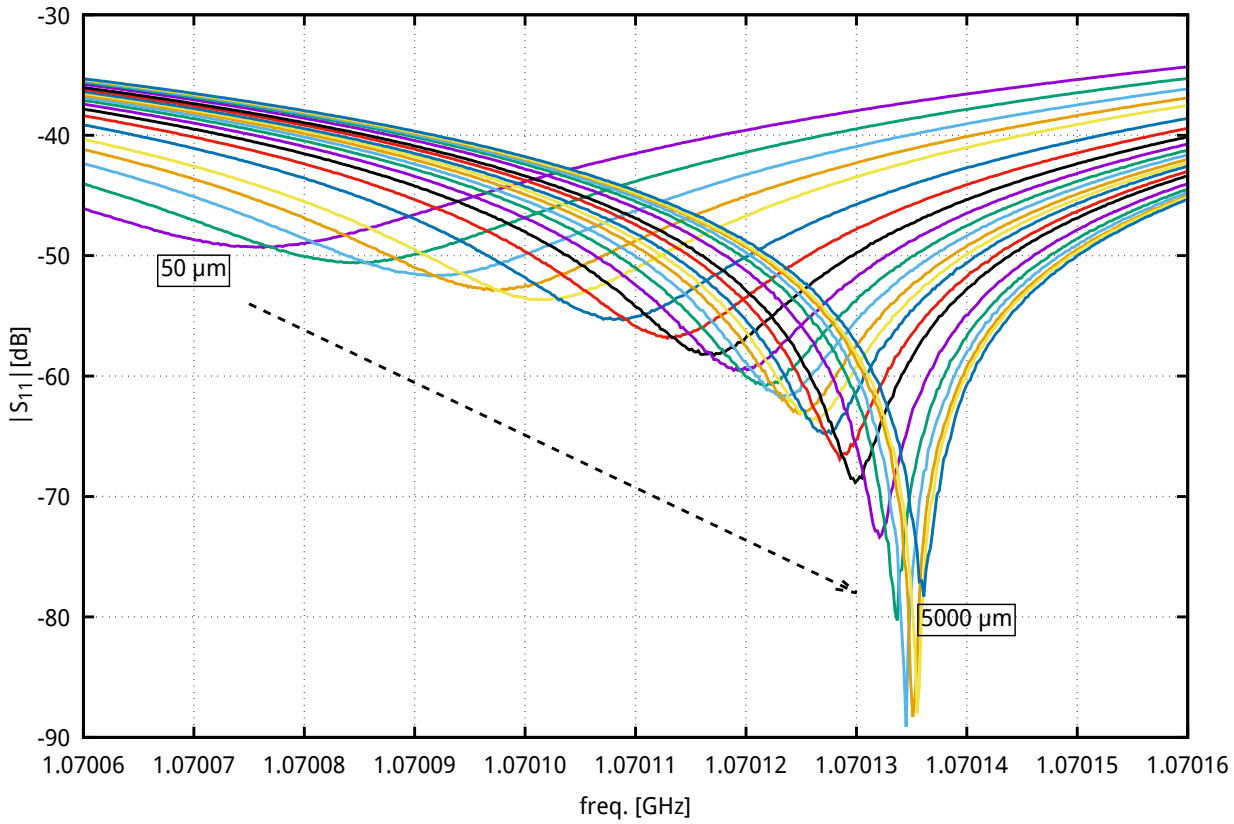

Figure 2.25 Measured $|S_{11}|$ for probe-sample separation values of: 50, 100, 150, 200, 250, 350, 450, 550, 650, 750, 850, 950, 1050, 1150, 1350, 1550, 2000, 2500, 3000, 3500, 4000, 5000 µm.

resonances is around 70 kHz instead of 50 kHz in simulations. The difference between experimental and simulation results is due to the fact that conduction losses are not considered in the simulations. Clarification on this matter will be given on Chapter 5.

The experimental set-up corresponds to the one presented in Fig. 2.1. This time, we employ a high-precision wafer probing station as x-y-z translation stage to control precisely the sample displacements. The sample under test is held with adhesive tape on the probe station chuck which is controlled by a computer that allows displacements in the order of 1 µm (see Fig. 2.26). The sample utilized in the measurement is briefly described in the next paragraphs.

Since this work was performed in collaboration with *Bombardier Aerospace*, damage and undamaged CFRP panel were provided by the company for testing purposes. These panels were build following specification as if they were part of an actual aircraft. Thus, they comply with their specification containing all required layers including LSP and paint.

The sample that was used in our tests, is simply a small portion of one of those panels that we cut in order to be fit in the probe station chuck. Specifically, the sample is 4 mm thick

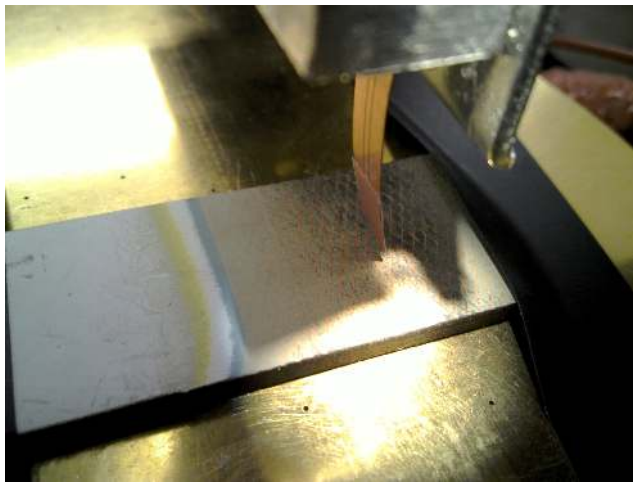

Figure 2.26 CPW probe and sample on probe station.

piece of CFRP panel manufactured using conventional layup process. It is covered with a layer of LSP and a non-conductive 300 µm thick paint layer. The LSP consists of a 50.8 µm thick expanded copper foil (ECF). The corresponding diamond dimensions, *LWD* and *SWD*, are 3.17 mm and 1.42 mm respectively. A picture of the sample is shown in Fig. 2.27. As it can be appreciated in this figure, the upper part of the sample was sanded to expose the wire mesh in a way that three different regions can be identified from top to bottom. In the upper part of the sample the copper mesh is completely exposed. This part is followed by an intermediate transition region where the paint thickness increases until it gets to its maximum 300 µm in the bottom region.

In addition to aesthetics, there are several technical reasons for painting composites. Among the most important ones, is the prevention of fluid damage; for instance, some resins are affected by water contact. The right paint system will provide a layer of protection against moisture and damaging fluids such as hydraulic fluid, fuel and de-icer. In our sample, four layers of paint (blue-white-yellow-white) are visible in the transition. The beige region above the transition is the epoxy surfacer film where the LSP mesh in embedded. The blue layer constitutes the filler that serves to smooth pinholes and voids. Later it follows three layers of paint namely, primer, intermediate coat and top coat. The thickness of these three layers together can vary from 100 µm to 300 µm depending on different needs presented by various aircraft zones. A complete mesh diamond has been removed in the exposed region (see red circle in Fig. 2.27) to simulate a defect.

In conventional microscopy, two quantities such as resonant frequency shift and quality factor are typically tracked [33]. In order to measure both quantities simultaneously, a frequency

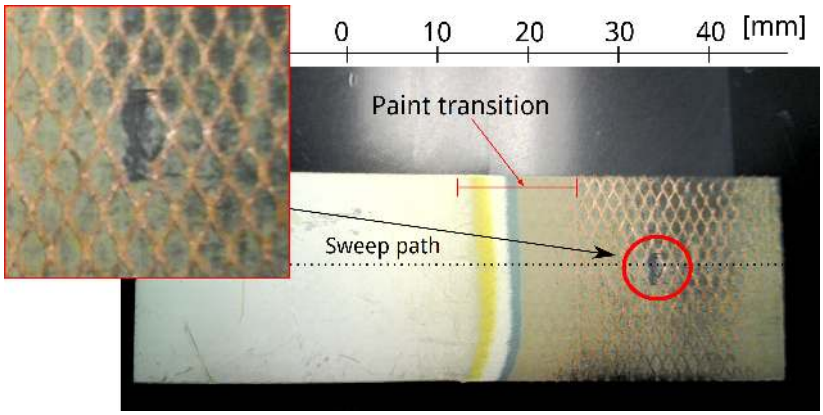

Figure 2.27 CFRP sample.

following circuit and lock-in amplifier in a feedback loop to lock the resonant frequency of a resonator is typically used. Alternatively, and in order to accelerate measurements, it is also possible to keep the generator at a fixed frequency near the resonance frequency read at a given probe position and then observe the variations of the reflection coefficient as the probe is scanned over the sample.

We use the same computer that controls the sample coordinate's movement to trigger the VNA that feeds the probe-resonator chain. At every new position of the probe relative to the sample, the computer triggers a new measurement of the reflection coefficient. The measurement is centered at a frequency of 1.053 GHz and over a 200 kHz span. The span width is chosen to include only one of the resonances in the Fabry Perot resonator. The reflection coefficient curve is recorded by software every time the probe moves to a new position. In a post-processing stage, changes in resonance frequency, or S_{11} at a fixed selected frequency, can be derived from the recorded data.

Measurements have been taken every 200 µm along the straight path that goes through the removed diamond. See Fig. 2.27. A regular pattern of peaks is observed every time the probe crosses a copper strand in the unpainted and transition regions. Each time, the system resonant frequency is modified. As a consequence, $|S_{11}|$ variation of 15 dB approximately are noted in these regions (see Fig. 2.28). The missing strand at 30 mm exhibits much greater fluctuations with $|S_{11}|$ values between -45 dB and -70 dB which make it easy to differentiate from the rest of the pattern. For probe positions between 17 mm and 25 mm the peaks are attenuated about 10 dB relative to the ones between 25 mm and 40 mm. The later attenuation is caused by the increasing thickness of the paint over wire mesh. The level of attenuation reaches its maximum for distances up to 15mm where the paint thickness is 300 µm. Different techniques (phase detector, distance modulation) can be utilized in order

to improve the sensitivity of the system and potentially detect the mesh under the paint.

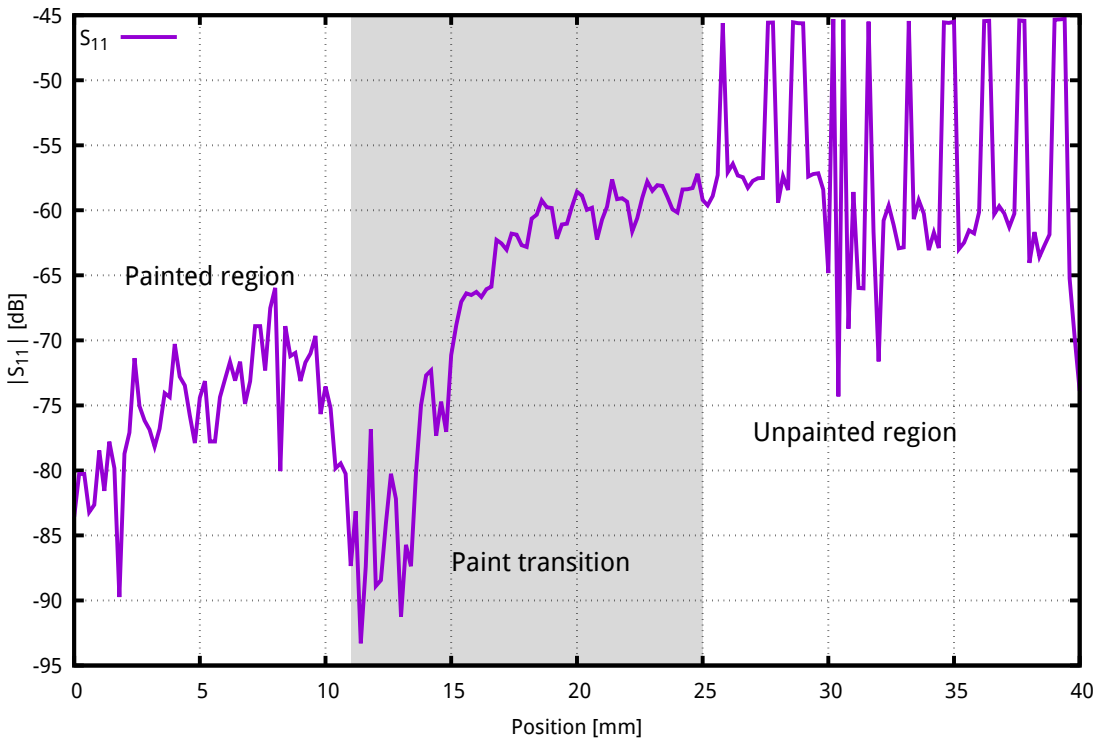

Figure 2.28 $|S_{11}|$ at resonant frequency as a function of distance.

The same behavior can be described in terms of frequency shifts. In this case, we record the frequency at which the minimum S_{11} occurs, and subtract the result from a reference frequency, e.g. 1.053 GHz. In Fig. 2.29 can be observed that every time the probe senses a copper strand, the frequency is shifted down from 10 kHz to 20 kHz in the non-painted area of the sample. The grid is clearly detectable by the microscope for positions in the 15 mm to 40 mm range. When the probe moves into the painted region, the frequency shifts are not significant enough to differentiate the copper from the CFRP. As stated before, the loss of sensitivity is caused by the 300 µm paint layer that separates the probe from the LSP mesh.

2.6 Conclusions

In this chapter, we explored the potential of electric probes to detect defects in LSP of composite aircraft. A simple resonant circuit has been used for this purpose. In the first approach a microcoaxial probe was used as a detection element close to the sample. A set-up has been build with the previous probe that allow us to test the capabilities and limitations of the probe as well as the circuit, in two different scenarios namely width and groove gauge.

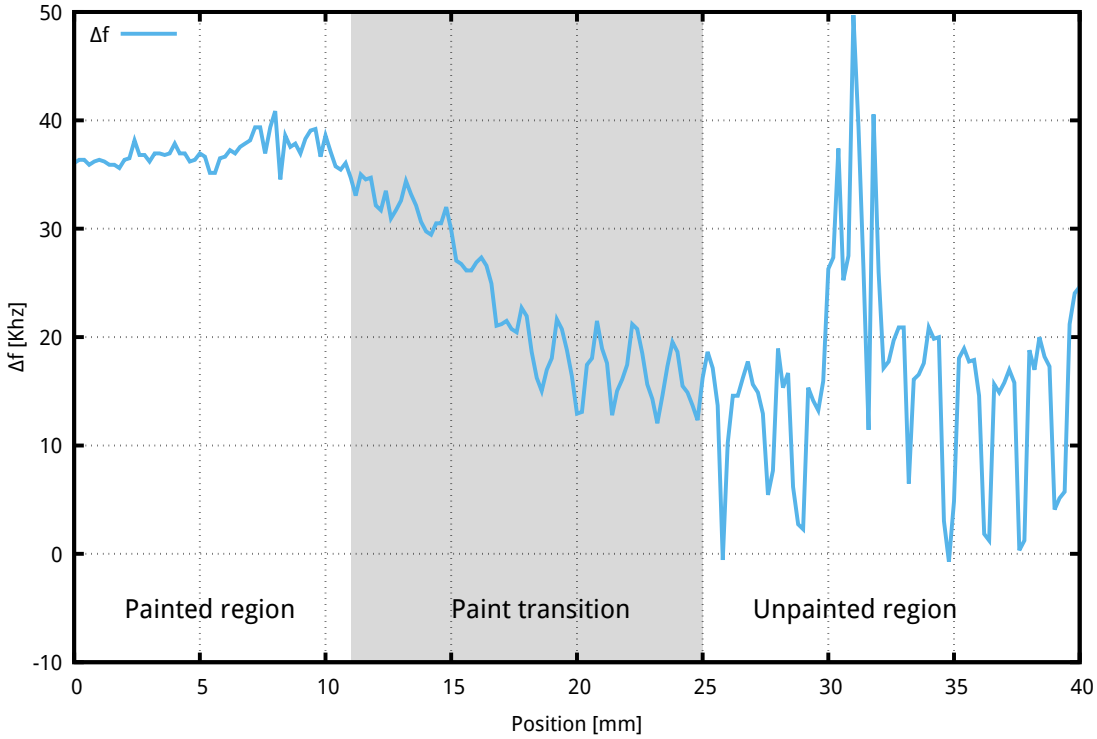

Figure 2.29 Resonant frequency shifts as a function of distance.

It has been concluded that the system is able to discriminate copper traces etched on a substrate up to 76 µm width. On the contrary, the system has failed in detecting thin slots etched on copper. Moreover, the realized experiments showed the importance of probe-sample distance separation. This variable has been identified as a critical detuning parameter in the measurements. Simple control techniques have been attempted to accurately govern the probe-sample separation with minor success. A new CPW probe has been introduced as a response to the previous problem. This probe printed on flexible substrate sets accurately the probe-sample distance separation without recurring to traditional slow and cumbersome mechanism. Tests have been conducted in a probe station were a precise correlation between measurements and simulations has been confirmed. The test platform is able to detect changes of this variable in the order of a few micrometers.

Trials over a piece of aircraft CFRP sample has been performed with the proposed CPW probe. It has verified that defects can be detected in the non-painted region of a wire mesh which is installed directly over the CFRP panel. The difference in conductivity between the materials is sufficient to be translated into deviations of the reflection coefficient of frequency shifts. Variation of the paint layer thickness over the LSP mesh layer is also clearly detected. However, the design sensitivity is not enough to detect the wire mesh under a 300 µm paint

layer.

Summarizing, the new CPW probe design built with a flexible substrate has been proven efficient to avoid cumbersome distance control mechanism. The probe is able to cover large areas and find small details at the same time. The relation between the paint thickness and the amplitude of the peaks or frequency shifts can be potentially used for quantitative measurements. Further work will be presented in the next chapter where we developed a new magnetic probe. This probe is sensitive enough to make the wire mesh visible under the paint. Also, the paint thickness can be measured accurately.

CHAPTER 3 MAGNETIC PROBE

3.1 Introduction

Inspired by the good performance of the resonance-based technique described in the previous chapter, we have developed a new loop probe designed to overcome the limitations of the electric probe presented in Chapter 2. The same straightforward set-up is employed to track changes in resonance frequencies to identify defects (Fig. 3.1). This probe has the following features [44], [45]. Firstly, it operates on a low microwave frequency (around 1 GHz), which allows penetration in lossy materials. Secondly, the printed tip of the probe has a geometry that is adapted to the shape of the objects to image (here a single LSP cell) in order to maximize sensitivity. Likewise, the tip can be reduced in size if needed, since it is only a small part of the resonant structure. However a smaller probe would lead to reduced mutual coupling with the LSP mesh, and therefore to reduced sensitivity. Thirdly, the probe is implemented on a flexible substrate and it can be swept conformally to the curvature of test objects, such as aircraft fuselage. Another benefit of this flexibility is that the probe can slide and maintain physical contact with the surface under test. No extra mechanism to control the probe-to-sample distance is required, as this function is built into in the sliding probe. In this chapter, we also present an improved version of this probe, which allows higher resolution immunity to the presence of surrounding objects due to better balancing and improved sensitivity. It is shown that in addition to enable detection of sub-millimeter broken strands in LSP mesh, it is also possible to measure accurately the paint thickness over the mesh, which is a critical parameter affecting the mobility of lightning strike attachment point [11]. This chapter is not addressing the detection of corrosion in the wire mesh.

Following the principles of microwave microscopy, the source of the evanescent fields is typically a sub-wavelength antenna. In this case, we utilize a printed loop at the end of a low loss coaxial line resonator coupled to the source by a tunable reactive element (tuner) (see Fig. 3.1). Data is gathered by a computer and by post-processing this data, we can extract the significant information and build the wire mesh images that allow us to identify faults.

As it was conducted in Chapter 2, a software simulation with *Keysight-ADS*® is useful to illustrate the behavior of the set-up in presence of a wire mesh. As illustrated in Fig. 3.2, a microwave source excites a coaxial transmission line resonator through a coupling capacitor. The coupling capacitor represents the tuner in the experimental set-up of Fig 3.1. The coaxial line is terminated by a loop probe that is interacting with the sample. Losses of $0.3\,\mathrm{dB\,m^{-1}}$ are considered in the coaxial line model, and a real characteristic impedance of

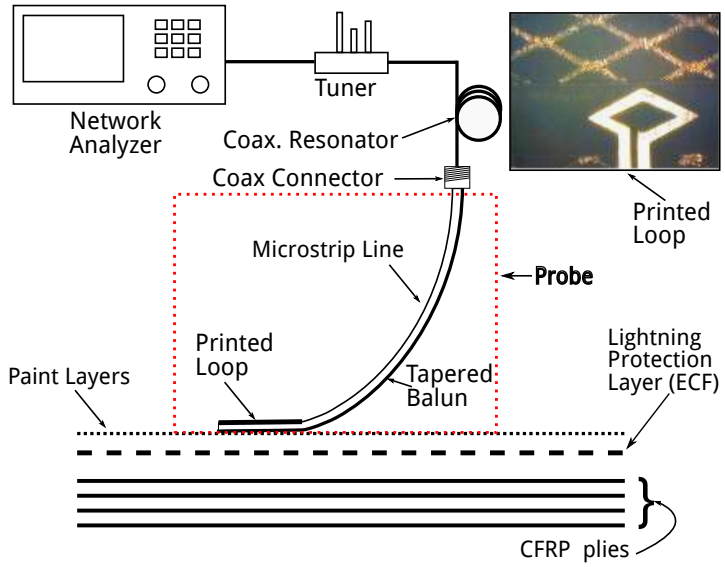

Figure 3.1 Schematic of the experimental set-up. A photograph of the balanced loop probe is shown in the top right corner.

50 Ω is assumed. The justification of the chosen inductance range is given in the next section. The series resistance R represents a fault in a wire mesh cell. The plot of S_{11} parameter for three values of inductance, i.e. 1 nH, 2 nH, 3 nH and no losses (R=0 Ω) are presented in Fig. 3.3. The resonance frequency is shifted down with increasing values of inductance. In a Smith chart representation, the Q-circle is rotated clockwise, overlapping itself in part, when the probe inductance is increased. Because the losses are constant, all the points are constrained to the same Q circle [39]. Probe and sample losses could be included in the model with a resistor in series with the inductor. For this situation, there will be a new Q circle for each

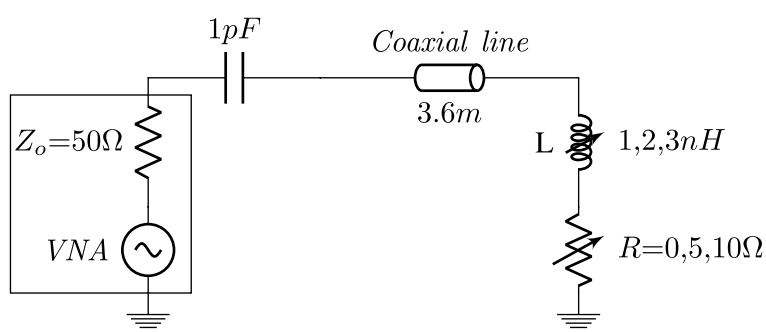

Figure 3.2 ADS set-up simplified model.

new resistor value. This is illustrated in Fig. 3.4 for resistor values ranging from $0\,\Omega$ to $10\,\Omega$ and a fix L of 1 nH.

3.2 Magnetic Probe - loop antenna

In this section we discuss the utilization of a loop probe as a means of detecting damage in the wire mesh. Square and circular loop probes are widely used for measuring magnetic fields. For a NDE application, we want to maximize the interaction between the probe and the LSP mesh in order to have a better measurement sensitivity. It is therefore required to maximize the mutual coupling between the two. As formulated by [46], the coupling is higher when the two loops have the same shape and when the distance between them is minimized. In brief, the main idea consist in using a probe with the same shape and dimensions of one LSP unit cell diamond or loop. As the probe sweeps over the painted LSP, its impedance will change first, according to the condition (i.e. broken or not broken) of the wire mesh beneath, and second, due to the distance between the probe and mesh which is imposed by the paint thickness. Furthermore, the paint thickness can be tracked by the variation of coupling due to the probe-cell separation. It is important to emphasize that the size and shape of the probe depends on the size and shape of the chosen wire mesh. Specifically, samples and wire mesh provided by *Bombardier* employed in the *CSeries* program are utilized in the present project.

To estimate the value of inductance that was referenced in the previous section and also justify the simple circuit model employed in the present section, a method of moments simulation of the probe was realized with $Feko^{®}$. The simulated probe consists of a rhombus with diagonal length of 3.17 mm and 1.42 mm respectively (see blue probe in Fib. 3.5). Furthermore, it is composed of 400 µm wide perfect electric conductor (PEC) strips and excited through an edge port. Considering 1 GHz as the working frequency, the inductance that results is in the order of 3 nH ($L = Z_{probe}/j\omega$). Also, according to [47] the radiation resistance is considered negligible for a probe with a ratio of a perimeter to wavelength smaller than 0.02. This was also verified by simulations.

The coupling between the probe and sample can be modeled with a simple equivalent circuit presented in Fig. 3.6. The left coil represents the probe (L_p) while the right one (L_s) represents a cell diamond in the LSP. R_s is the resistance of one grid loop. Specifically, two cases can be analyzed related to this circuit. The first one, corresponds to an intact wire mesh where R_L is very low. While the probe slides over the mesh the coupling coefficient K change continuously, and so the mutual inductance M. The M value peaks when the two loops exactly overlap with each other. In this case the input impedance of the circuit tends

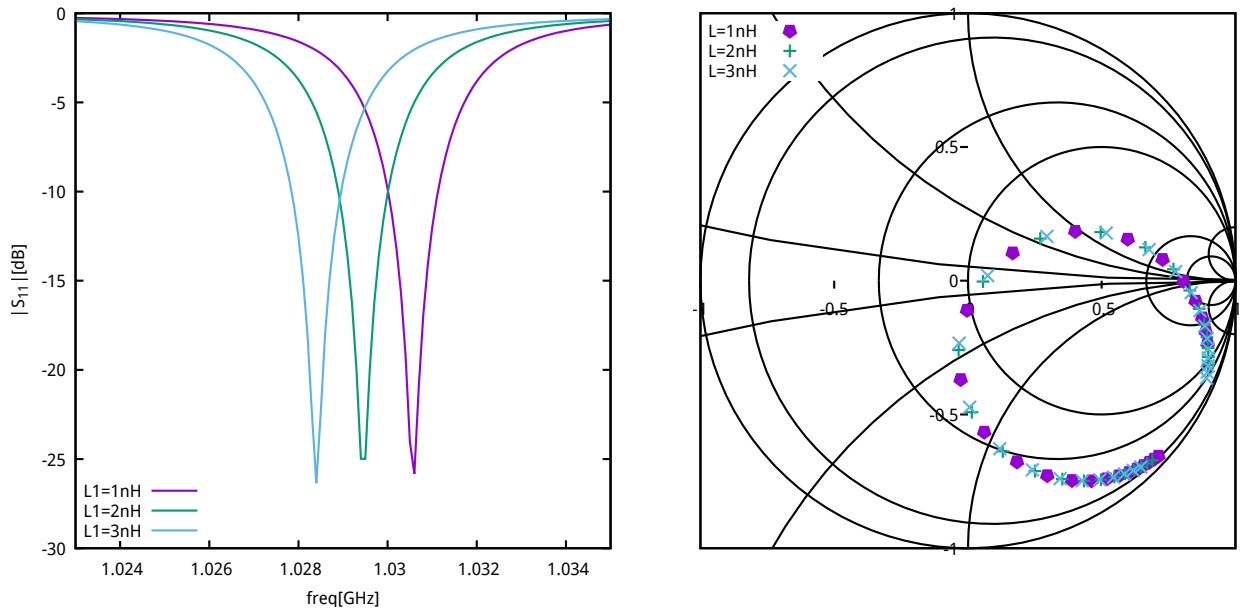

(a) (b)

Figure 3.3 Circuit response for $L = 1, 2, 3nH$ and $R = 0\Omega$. (a) S_{11} and (b) Q circles.

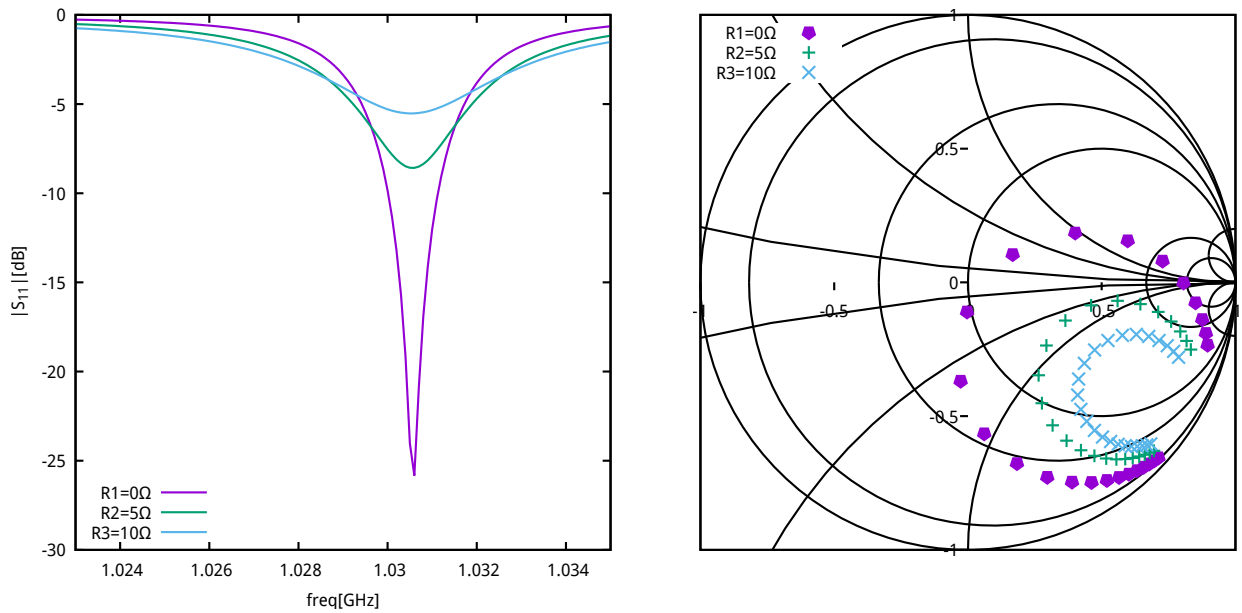

(a) (b)

Figure 3.4 Circuit response for $L = 1nH$ and $R = 0, 5, 10\Omega$. (a) S_{11} and (b) Q circles.

to its minimal value. A simple circuit analogy would be a transformer with its secondary shorted. On the other hand, the minimal coupling K occurs when the center of the probe

is halfway between two mesh diamonds. In this situation the input impedance reaches its maximum value. In the second case, it is assumed that the wire mesh features a cut strand. This is represented by a high value of R_L. In this circumstance, the effect of the wire mesh is very weak over the input impedance of the probe that remains almost unaltered. The contrast between the two previously described states is responsible for the shift in the resonator frequency. A third important variable that needs to be taken into account is the distance between the probe and the sample due to the paint thickness. Increasing this distance causes lower values of K which, in turn, decreases frequency shift. Summarizing, the overall combination of increasing separation and alternation between grid cells while the probe moves produces a modulation effect that can be appreciated in simulations and measurements as well. This will soon be demonstrated with simulation (Fig. 3.7) and experimental (Figs. 3.11 and 3.14a) results.

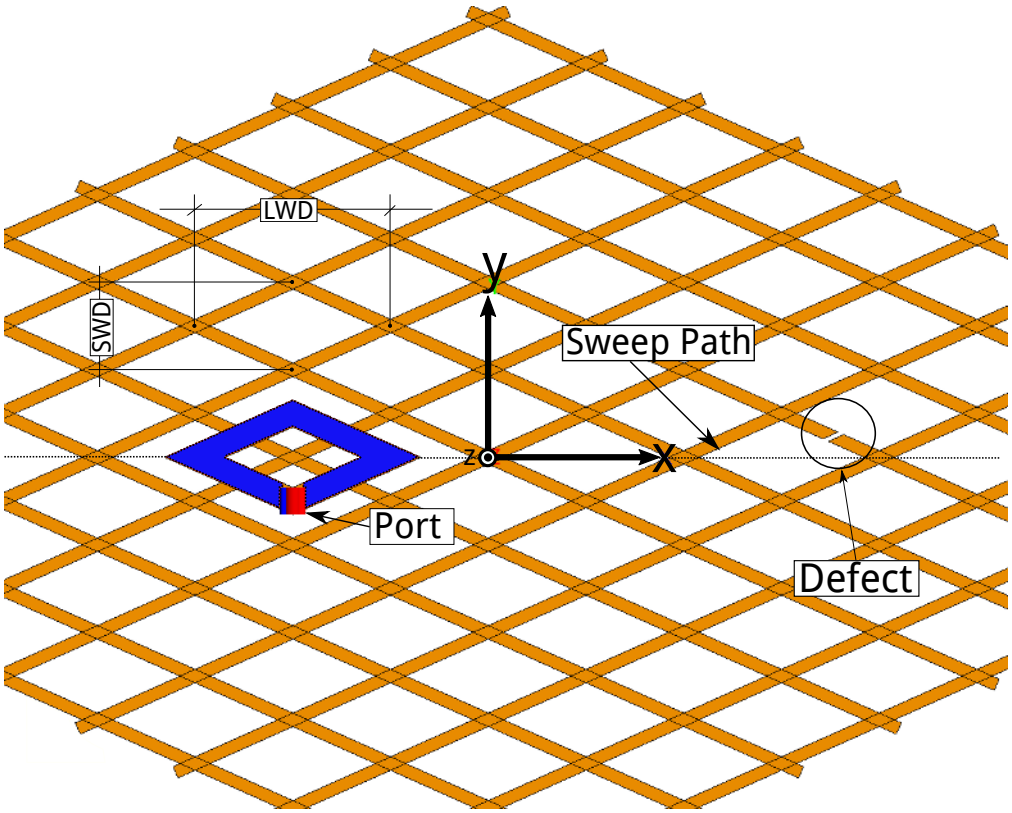

Figure 3.5 Wire mesh and probe simulation model.

To illustrate the operation of the system a method of moments simulation was realized. A typical rhomboid grid or expanded foiled grid made of PEC is simulated. The dimensions are the ones of the specimen that later will be tested in the laboratory, namely long way

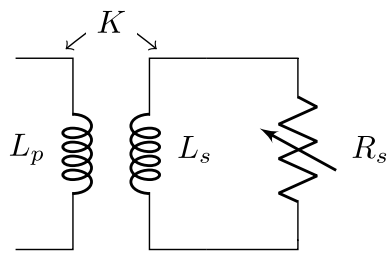

Figure 3.6 Equivalent circuit representing the interaction between the loop probe and the mesh.

of the diamond (*LWD*) of 3.17 mm and short way of the diamond (*SWD*) of 1.42 mm. See Fig. 3.5. The width of the strips are 200 µm. The dimensions of the simulated probe are the ones described previously in this section. First, a simulation is performed with the probe-to-sample distance constant and equal to 125 µm. The probe moves in a straight path. Every 3.17 µm, the probe overlaps with a new grid rhomboid, which makes the impedance of the port that excites the probe reach its minimum. The impedance increases to its maximum at half *LWD* distance, when the probe is halfway between two grid loops. The results of the simulation is shown in Fig. 3.7, with curves identified as "simple loop".

In order to simulate a defect, a strand is cut by a 100 µm gap at a distance of 5 mm. (See indication in Fig. 3.5) This defect is clearly shown in the impedance curve where we count 4 minimums every 10 mm until we reach the broken cell. At a distance of 5 mm the impedance is around 14 Ω instead of 11 Ω (see Fig. 3.7).

A second set of simulations consists of increasing the probe-sample separation while moving the probe along the same path. The separation distance increases from 25 µm to 250 µm when the probe moves over 10 *LWD* of linear displacement in x direction. In Fig. 3.7 the solid curves represent a fixed separation probe-mesh distance while the dashed ones correspond to variable separation. Peaks and valleys repeats with the same period but attenuation is observed as the probe moves farther from the sample. There is a link between this attenuation and the probe-grid distance, which in the practical case will correspond to the paint thickness. To further highlight the dependence of the probe impedance with the separation distance caused by the paint, in Fig. 3.8, we plot the input impedance against an increasing separation distance for a model where a probe is perfectly overlapping a mesh diamond.

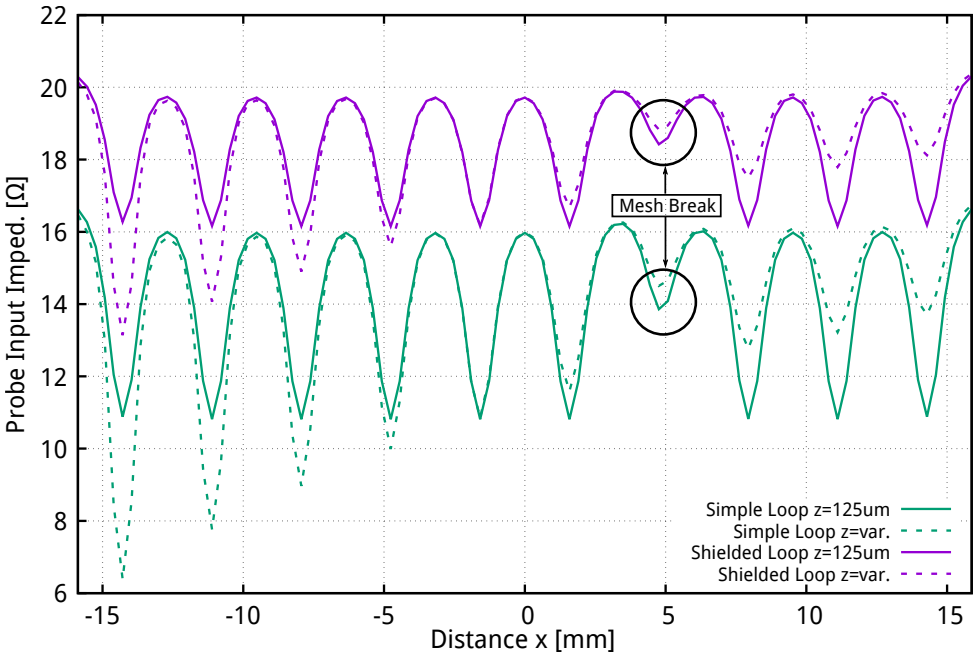

Figure 3.7 Simulated probe input impedance for simple probe (green) and shielded probe (violet). Fixed (solid) and variable separation (dashed).

3.3 Experimental results

As mentioned in Section 3.1 the experimental set-up used (Fig. 3.2) is similar to the one extensively presented in previous works [33], [34] that has been proven to be robust. A CFRP sample is mounted on an x-y-z computer-controlled stage that allows precise movements with a 1 µm accuracy. The computer that controls the stage also triggers the vector network analyzer (VNA) Keysight PNA-X N5247A that is recording the swept-frequency S_{11} response for every sample position.

The sample is a 4 mm thick piece of CFRP panel manufactured using conventional layup process. It is covered with a layer of LSP and a non-conductive 300 µm thick paint layer. The LSP consists of a 50.8 µm thick expanded copper foil (ECF). The corresponding diamond dimensions, *LWD* and *SWD*, are the ones used in the simulation model (see Fig. 3.5). A picture of the sample is shown in Fig. 3.9. As it can be appreciated in this figure, the upper part of the sample was sanded to expose the wire mesh in a way that three different regions can be identified from top to bottom. In the upper part of the sample the mesh is completely exposed. This part it followed by an intermediate transition region where the paint thickness increases until it gets to its maximum (300 µm) in the bottom region.

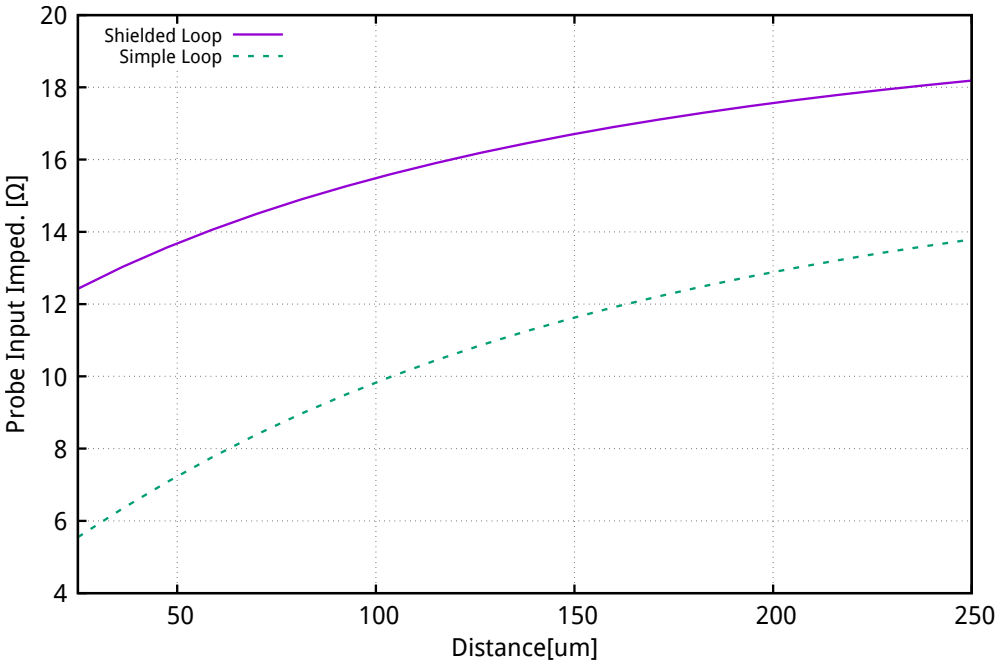

Figure 3.8 Simulated probe input impedance for simple probe (dashed) and shielded probe (solid).

Two defects have been practiced in the sample. A complete diamond has been removed in the exposed region and a deep scratch as been performed in the painted region. Both are highlighted in Fig. 3.9. As demonstrated in Fig. 3.8 the distance between the probe and the sample plays a critical role in detuning the resonator. Traditionally, cumbersome mechanisms have been used to keep this distance constant (see [40], [48]). The approach we adopt in this work is simply to separate the probe and the sample by a flexible layer of thin substrate sliding over the sample. The substrate used in the probe was polymide of 127 µm thickness. Since this substrate is flexible, we are able to bend the probe and 'sweep' the sample while keeping the distance between them constant at every position (See Fig. 3.1). A drawback of this is that the substrate thickness adds up to the probe-to-mesh distance caused by the paint. As can be noticed in Fig. 3.8, an additional separation of 125 µm can have a significant impact on the impedance and decrease the sensitivity on the height (therefore paint) thickness. The choice of 127 µm for the substrate was found to be a good compromise between measurement sensitivity and mechanical stability of the probe position during scanning.

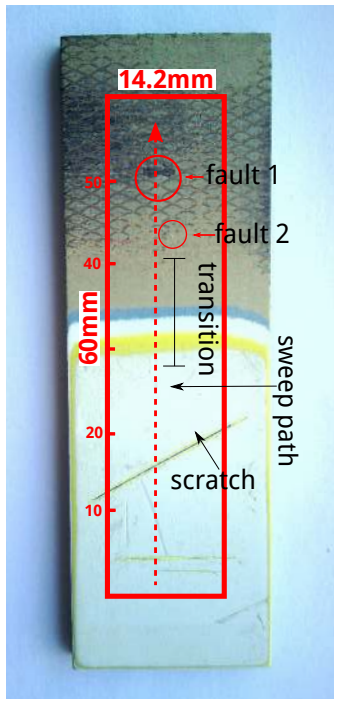

Figure 3.9 CFRP sample.

3.3.1 Balanced probe

Measurements have been performed using the circuit in Fig. 3.2. The frequency sweep included over 400 measurement points over a range of 500 kHz centered on 1 GHz. The span width was chosen to include one of the resonances in the Fabry-Perot resonator composed by the tuner, coaxial line and probe.

Since the loop is fed by a coaxial transmission line, a microstrip balun was inserted in the same piece of substrate between the line and the probe. The exponential tapered type balun was designed according to the specifications in [49]. The end of the substrate has been cut in a 'T' shape to ensure that the traversal axis of the probe is also kept parallel to the sample. A picture of the fabricated printed loop with the integrated balun is presented in Fig. 3.10.

In a first test, the probe swept the sample along the path in Fig. 3.9 from bottom to top. A swept-frequency S_{11} measurement was taken every 700 µm which corresponds to half SWD. Using this data, the frequencies of minimum $|S_{11}|$ for all probe position are recorded. The difference between these frequencies and an arbitrarily fixed reference is used to calculate a Δf. The results are shown in Fig. 3.11. The oscillation in the probe impedance predicted in Fig. 3.7 clearly appears as a fluctuation of the measured resonance frequency. Moreover, we observe that the variation on the frequency shifts are directly linked to the probe-sample

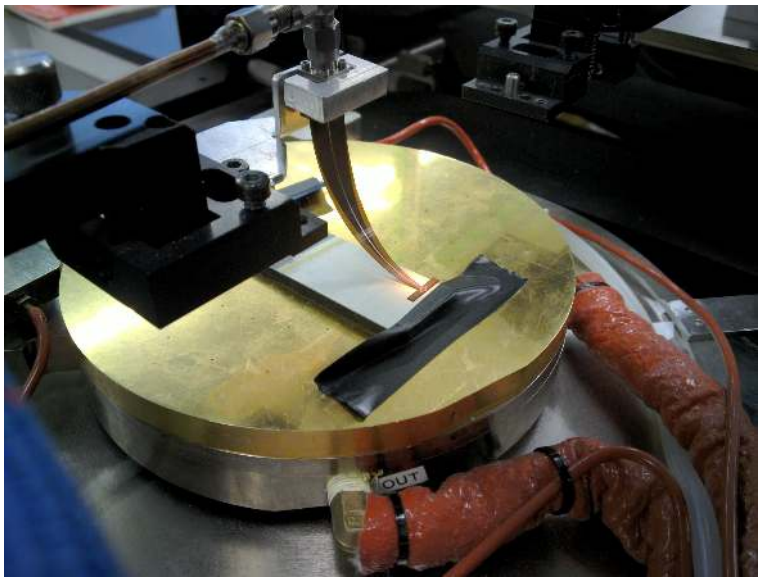

Figure 3.10 Printed loop probe with integrated balun scanning the sample.

distance variations. The increase of resonance frequency shift diminished with the decrease of the paint thickness. Shifts on the order of 150 kHz are present on the top of the sample, where the paint vanishes. The missing diamond is also detected at around 55 mm where there is a missing oscillation. It is important to notice that the scratch, in the bottom part of the sample, was not present for this first series of measurements. The paint thickness versus distance was afterwards measured with an optical microscope whose resolution is 1 µm, and it was plotted in same figure.

An amplitude modulation effect can be remarked in the oscillations, for instance in the painted area between 0 and 30 mm. This is due to a slight misalignment between the probe path and the lattice axes of the periodic LSP sample. This induces changes in K and it causes the smooth modulation on the oscillations appreciated in the painted region. The effect is also present in other regions but it is more difficult to perceive due to the high amplitude of oscillations.

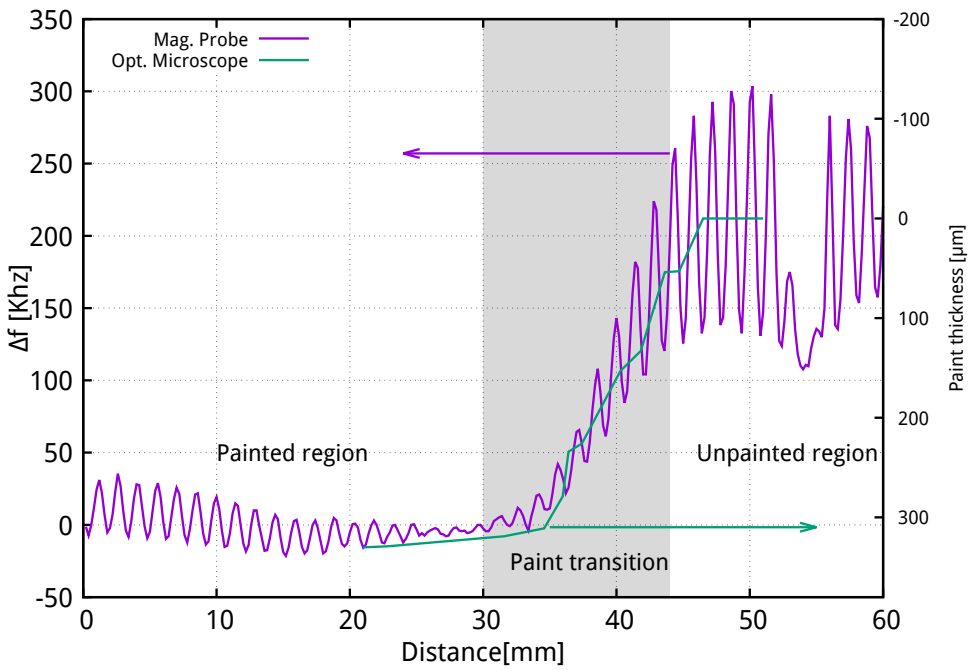

Figure 3.11 Measured loop probe frequency shifts and optically measured paint thickness vs distance.

3.3.2 Shielded Probe

It has been observed during the tests that the structure presented in the previous section which was essentially composed of a printed loop and an integrated balun, was sensitive to objects in the near field. It was also noticed that the structure radiates. This indicates that the integrated balun was possibly inefficient in preventing common mode currents on the printed circuit board and coaxial line. Since the whole detection concept is based on measuring field alterations in the immediate neighborhood of the probe (evanescent fields), this radiation perturbs the resonance frequency, which is an undesired effect, and it may reduce measurement sensitivity. We present in this section a shielded printed probe as an alternative device to overcome the aforementioned problem.

Shielded probes are commonly used in EMC diagnostics. Particularly, a shielded loop with central gap location offers a symmetry that prevents unwanted common mode coupling [50]. Among different types configurations, the structure that better suits our purpose is a planar multi-layer shielded loop with central-gap and loop inner conductor shorted to the shield at the probe gap [51]. Since a flexible probe is needed in order to maintain sliding contact on the sample under test, shielding was implemented with a multilayer flexible PCB (see Fig. 3.12). Basically, it consists of a microstrip line that excites the loop through a via. The diamond-

shaped loop is at the same time the return path of the microstrip line and the coupling loop element. The dimensions of the loop are exactly the same as the ones of the simple loop presented in the previous section. Specifically the width is 400 µm for the loop and 200 µm for the feeding microstrip line. It has been verified experimentally that for this design the results are not affected by the presence of surrounding objects. The simulations have been performed according to the structure in Fig. 3.12 and the results have been included in Fig. 3.7 and Fig. 3.8. Essentially the behavior is the same as for the simple probe case. However, an offset of approximately 4 Ω is observed due to the inductive reactance of the feeding line. The amplitude of the oscillations is also slightly reduced compared with the simple loop case. This effect is owing to the capacitive effects within the shielded probe.

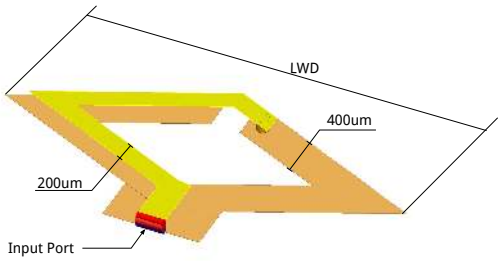

Figure 3.12 Planar multi-layer shielded probe.

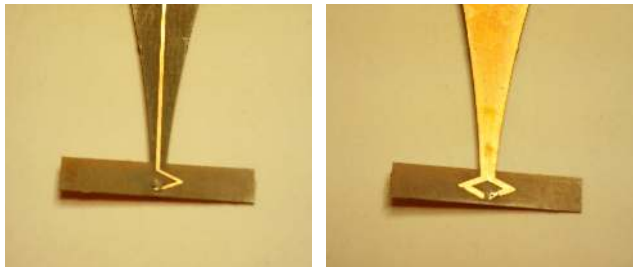

Figure 3.13 Photograph of the two sides of shielded probe printed on a T-shaped substrate. Dimensions are given in Fig. 3.12. (a) Feeding microstrip line. (b) Ground plane.

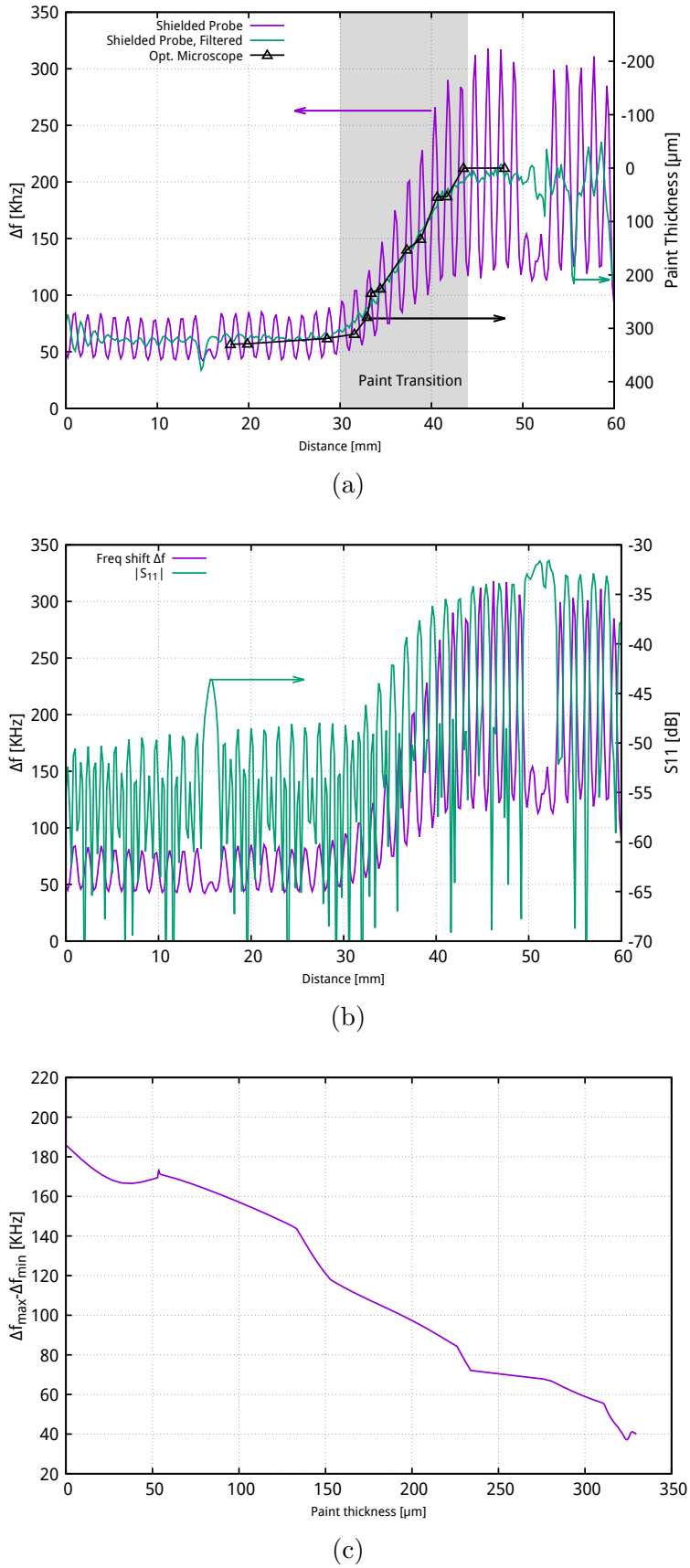

Figure 3.14 Shielded loop probe scan over the CFRP sample. (a) Resonance frequency shift and paint thickness. (b) Resonance frequency shift and $|S_{11}|$ at resonance. (c) Amplitude of frequency shift oscillations versus paint thickness.

The probe fabrication was carried out with same techniques and substrate as in unshielded probe. A picture of the probe showing both sides is given in Fig. 3.13. A scan of the same sample following the same path as in Section 3.3 was done and the results are plotted in Fig. 3.14a. In this case the modulation effect due to the misalignment between the scanning path and the diamond axes is barely visible. Both defects in the mesh are clearly visible. The scratch in the painted region at 16 mm where one oscillation is missing, and the missing diamond in the exposed region at 52 mm where two oscillations are absent.

To emphasize the link between frequency shift measurements with paint thickness, we have filtered the measured curve with a notch filter to remove the frequency components that produce the oscillation generated by the mesh. This technique produces a smother curve that mainly tracks the separation between the probe and the mesh, which is the paint thickness. The filtered response is included in Fig. 3.14a. As it can be noticed, good correlation exists between the paint thickness and filtered probe measurement. Moreover, taking in to account that during the measurements the resonant frequency moves in a range of 300 kHz while the paint thickness varies from 0 to 300 µm, it can be stated that the resolution of thickness gauge would be in the order of micrometers. This is because a fine-tuned VNA can achieve high frequency discrimination, at the expense of slower measurement times.

Fig. 3.14b is showing the minimum value of $|S_{11}|$ (i.e. at resonance) for the same scan path as in Fig. 3.14a. Oscillations due to the mesh cells are also clearly visible on this response, as well as the location of faults in the mesh. However, the Δf response shows a more stable and regular oscillation amplitude over the non-damaged LSP areas. Therefore, it should be preferred to the $|S_{11}|$ response in LSP evaluation. The amplitude of the oscillations ($amplitude \equiv |max(\Delta f) - min(\Delta f)|$) versus thickness is plotted in Fig. 3.14c. It can be clearly seen that the amplitude decreases with thickness, as expected. Eventually, a point will be reached where this amplitude saturates to a minimum value, which would be the noise limit. This limit depends on the roughness of the sample and the stability of the mechanical setup moving the probe. This point has not been reached in our test, even with a paint thickness (300 µm) that is higher than that typically used on aircraft (125 µm to 250 µm [12]). Tests on the 300 µm painted area covered with a 125 µm PVC tape still allowed the mesh oscillations and perturbation caused by the scratch and faults to be clearly observed.

Using the same set-up and to further highlight the possibilities of the probe, a two-dimension region was scanned, instead of a single path. The red rectangle in figure 3.15 marks the scanned area. The sample has been swept repeatedly in longitudinal paths separated 700 µm from each other. A contour plot is presented in Fig. 3.15. A contour plot is composed by

isolines that represent points with same resonance frequency. Many pieces of information can be extracted from this image. Firstly, each of the peaks corresponds to a diamond in the wire mesh. Higher density of contours indicates higher peak amplitude which in turns means thinner paint layer due to the stronger interaction between the probe and the mesh. So, the paint layer thickness decreases for increasing values in the y coordinate. Secondly, the slope of the surface that can be appreciated in the change of colors from top to bottom is also dependent on the paint thickness. Finally, the defects that were previously practiced on the sample, are clearly visible. The straight scratch line in the painted region and the missing diamond (defect 1) in the upper region can be identified by the interruption of the peak pattern that represents a healthy mesh. Besides, a second defect, that was not visible to the naked eye, was revealed after the measurement. In Fig. 3.16 an optical image of defects 1 and 2 are shown where the broken strands can be precisely identified.The test was repeated with the sample rotated around the z axis to observe the effect of the misalignment. Similar results and conclusion were obtained.

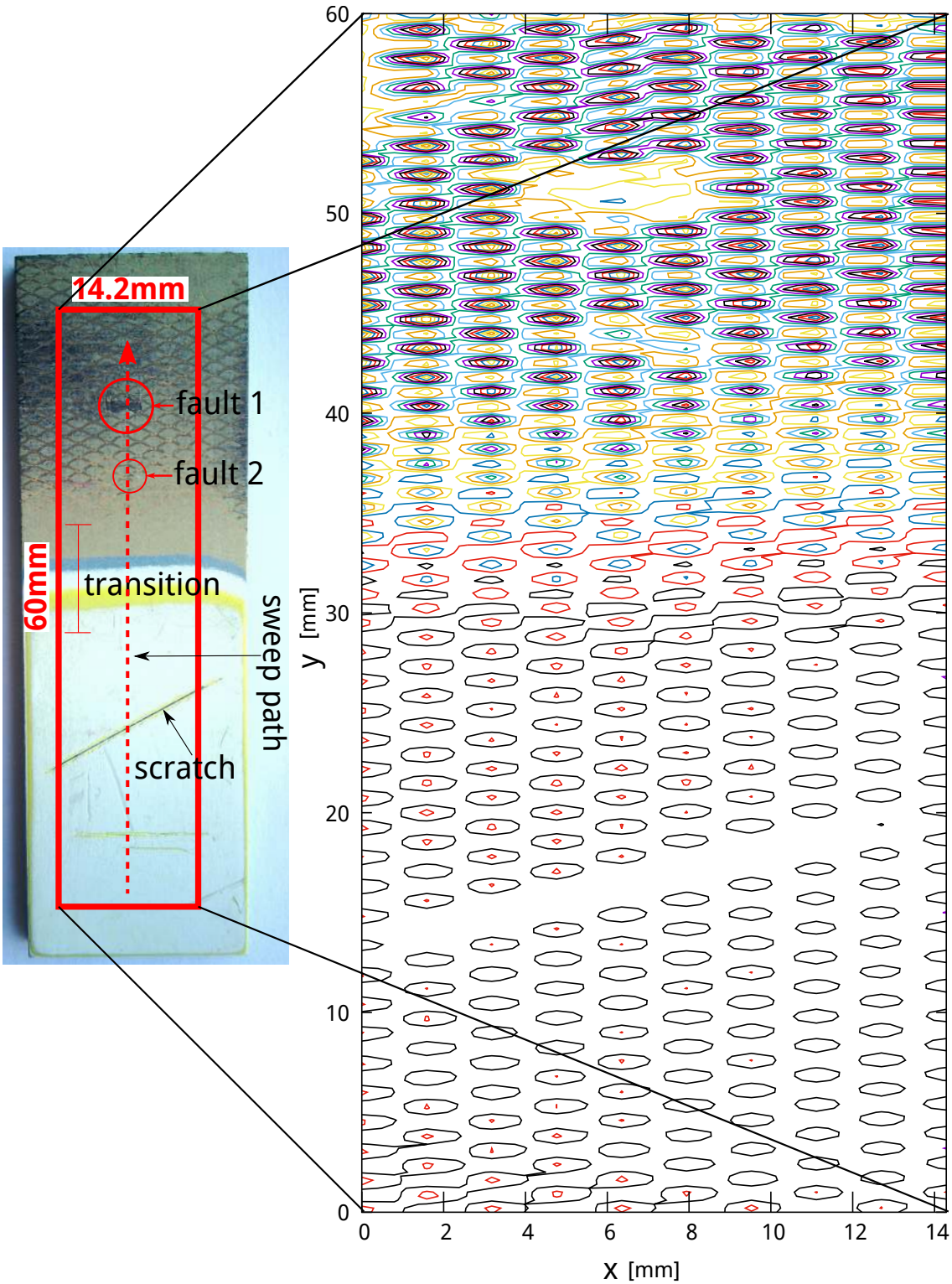

Figure 3.15 Scan Area - Contours every $1.5kHz$.

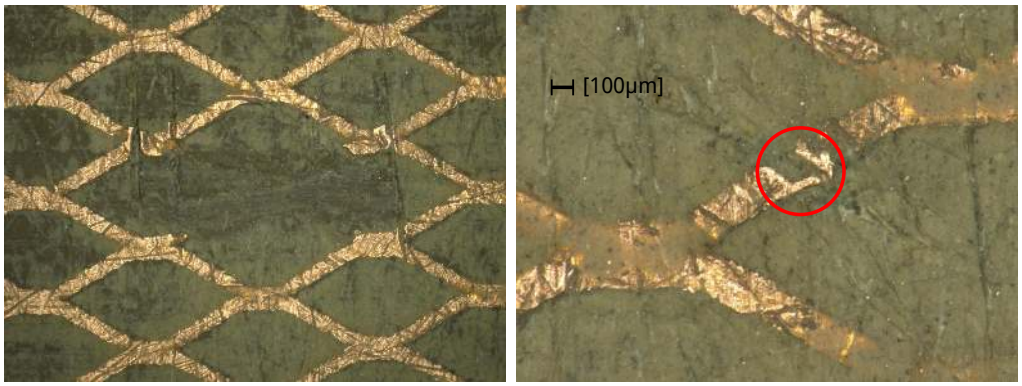

(a) (b)

Figure 3.16 Optical photographs showing defects 1 and 2. In (a) six cell loop paths are interrupted. In (b) one cell loop is discontinued.

3.3.3 Misaligned scanning

In order to stress the capabilities of the system the same sample used previously was covered by a 125 µm dielectric tape. The probe-sample distance was increased by 40% with respect to the maximum standard paint thickness which is 300 µm. Moreover, an angle was introduced between the scanning path and the cell diamond axes, so that the situation where the probe perfectly overlaps a mesh diamond never occurs. A picture of the experimental set-up is showed in Fig. 3.17

Since the objective of this experiment is to demonstrate the capabilities of the system to detect defects under the paint, a small area of 6 mm by 35 mm that covers the scratch is swept. The center point of this scanning area serves as a pivot point and the area is later rotated clockwise by 0°, 6° and 12°. The area covers a region of wire mesh and the start of the paint transition region. Contour plots with the results for tree different angles are shown in Fig. 3.18. It is clear that the scratch under the paint is perfectly detected as well as the wire mesh under the paint.

3.4 Conclusion

To summarize the main characteristics of the magnetic and electric probes a comparison of different features is presented in Table 3.1. The numbers in columns 2 and 4 are the amplitudes of the frequency oscillation due to the mesh in the painted and unpainted regions respectively. For the paint transition region, the base frequency difference between the unpainted and painted region is considered. The electric field distribution for the electric probe

Figure 3.17 Probe scanning sample and tape. Scanning angle of 12°

is concentrated in a small region very close to the tip of the probe. As a consequence, small resonance frequency variations are observed in the transition and painted region. The wire mesh under the paint is undetected as well as defects (scratch). On the contrary, the fields in the magnetic probe are able to reach the mesh under the paint. The bigger span in frequency variations allows finding small defect in the wire mesh under the paint. A frequency span of 265 kHz in the transition region is effective to track changes in the paint thickness in the order of 1 µm.

A new application of microwave microscopy technique has been presented in this chapter. It is able to reveal flaws (under the paint layer and exposed) in the LSP mesh of composite aircraft. Changes in conductivity between metal and carbon fiber shift the resonant frequency of a probe ended resonator that allows us to identify flaws by plotting the wire mesh underneath the paint. Two loop probes have been designed. The first one, with balun, that did

Region	Painted [kHz]	Paint Transition. [kHz]	Unpainted [kHz]	Removed diamond	Scratch
Electric probe	Not detected	23	50	Detected	Undetected
Magnetic probe	45	265	185	Detected	Detected

Table 3.1 Electric and Magnetic probe features comparison

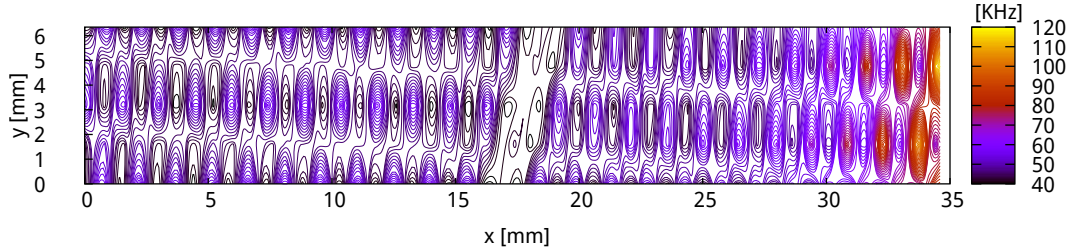

(a)

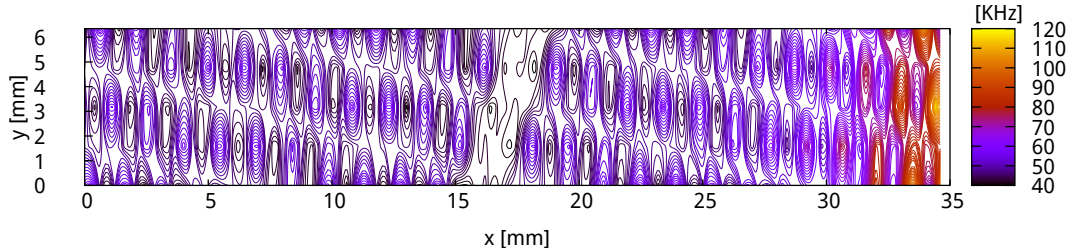

(b)

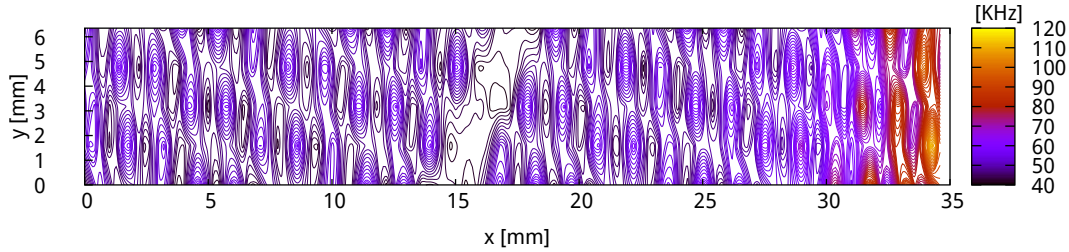

(c)

Figure 3.18 Scan over sample and tape. Scanning angle of (a) 0°, (b) 6°, (c) 12°

not efficiently eliminate the common mode on the feeding transmission line, and made the measurement sensitive to the presence of surrounding objects. The second probe, of planar shielded type, was demonstrated to work effectively by concentrating the fields only around the tip. Both probes have tips adapted to the shape of the wire mesh. They are also flexible so they can copy the curvature of the test objects.

This latter probe has been tested to sense defects as small as a scratch under the painted LSP, and it was able to detect it precisely. The introduced probes have been built with a flexible substrate. Bending the substrate while maintaining pressure on the test sample was confirmed as a simple and effective mechanism of probe-sample distance control to avoid cumbersome traditional set-ups. Lastly, a strong correlation between the paint thickness and frequency response has been pointed out, which could be used to measure the thickness of this layer with an accuracy in the order of micrometers.

Although the capability of the probe to detect broken strands and paint thickness has been demonstrated, quantitative indicators such as resolution, dynamic range and sensitivity have not been assessed in details.

CHAPTER 4 PROBE ARRAY

4.1 Introduction

It was mentioned in previous chapters that the ultimate goal of this project was to develop a device capable of detecting LSP wire mesh defects in the context of aircraft industry. Thus, the device in question should be able to scan large surfaces in a relatively short time. A structure aiming to achieve this purpose was designed and fabricated using the shielded probe presented before. The same probe was integrated 6 times in the same piece of substrate (see Fig. 4.1). A separation of 11.4 mm) between the probes was chosen as the minimal distance that would allow to solder the connectors placed at the other edge of the PCB. Edge mount 50Ω SMA connectors were used to link the probes to the *RF* switch board.

The probes are connected to a single-pole-six-throw (SP6T) off-the-shelf RF switch through semi-rigid coaxial cables. The switch is linked to the resonator through the common port. The rest of the measurement circuit, specifically the tuner and the VNA, are elements previously used in the single probe design. A Matlab® software controls the RF switch in a way that different outputs can be selected. It also triggers a VNA frequency sweep for each probe and moves the array to a new location after each measurement. Fig. 4.2 shows the probe array while sweeping over CFRP sample. Other components, namely the controller board and the RF switch board are also shown in the picture. Semi-rigid 50Ω coaxial cables that links each probe to its respective output in the switch board, are also displayed in this photograph.

Figure 4.1 Probe array.

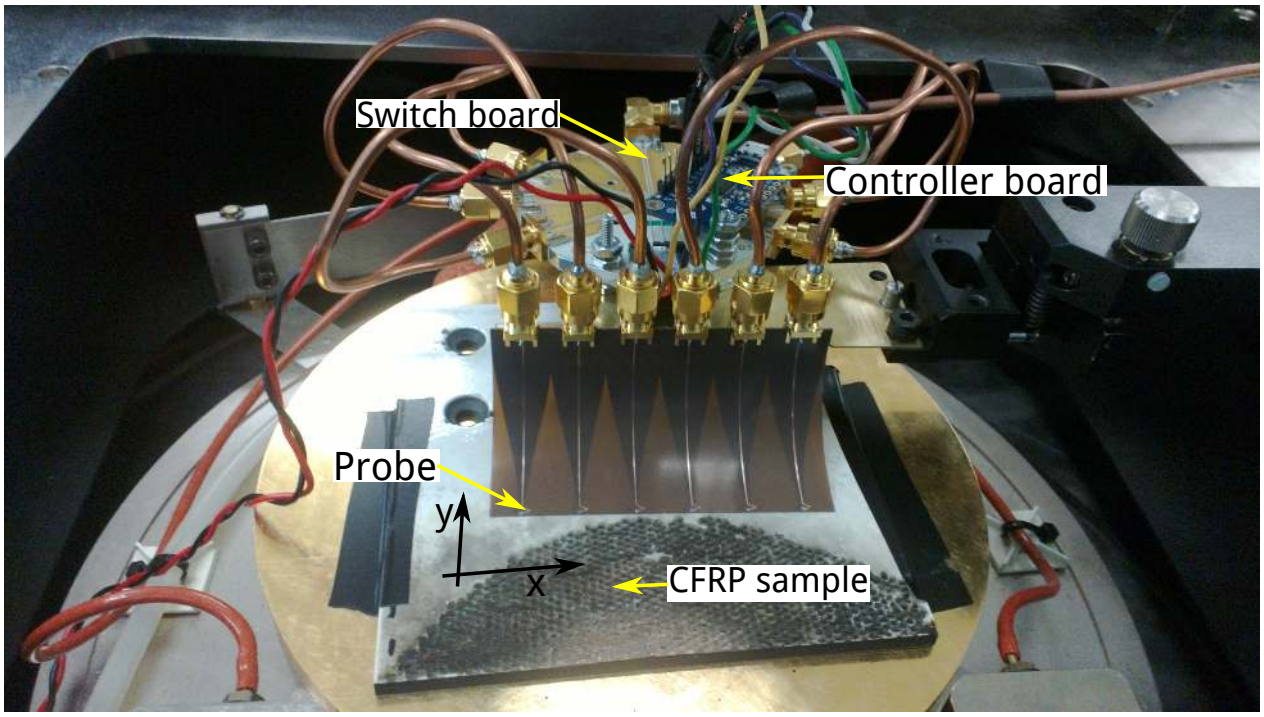

Figure 4.2 Probe array sweeping CFRP panel.

A straightforward way to understand what changes have been introduced in comparison to the set-up presented in the previous chapter is through a simple circuit schematic. In Fig. 4.3 a simplified schematic of the probe array is presented. Except for the switch, the rest of the elements in the circuit are the same as the ones presented beforehand in Chapter 3.

In order to understand all components that intervene in the probe array measurement set-up, a block diagram is exhibited in Fig. 4.4. It contains the devices and interfaces involved. All the devices are controlled by software developed in Matlab®. The probe station is linked

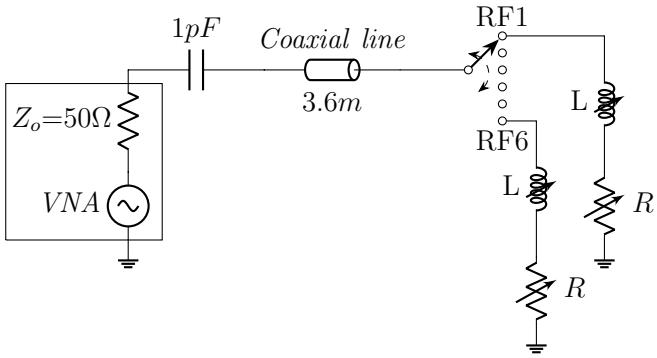

Figure 4.3 Simplified model SP6T

to the computer through ethernet (Eth). The same computer controls the switch via a USB interface, trough an intermediate device, the controller board $FT232H$. The $FT232H$ converts the computer USB interface into a general purpose input/output (GPIO) signal with CMOS levels that are used to control the switch. A second ethernet connection is also used to trigger measurements, get the measured data from the VNA and send commands to the VNA according to the particular needs of each measurement. Lastly, the RF path is composed by VNA, switch and finally the probe array.

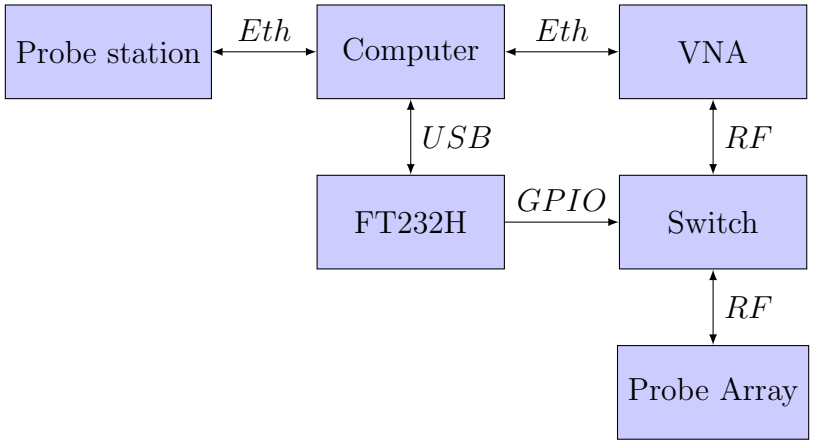

Figure 4.4 Measurement set-up - devices and interfaces.

4.2 RF switch

A switch is an electrical component for opening and closing the connection of a circuit or for changing the connection path of a device. An "ideal switch" should exhibit zero resistance to current flow in the "ON" state and infinite resistance in the "OFF" state. A practical design presents a small resistance in the "ON" state and a finite resistance in the "OFF" state.
For our design purposes, a key parameter that has been used to select the switch was the insertion loss. Particularly, a Minicircuits JSW6-3DR+ was chosen because of its low insertion loss and multiple outputs configuration. It is a single pole six trow switch which has low insertion loss, (0.6 dB at 1 GHz), return loss of (15 dB in ON state) and high isolation (37 dB at 1 GHz) . It also presents reflective shorts on output ports in the OFF condition. The company offers a convenient evaluation board (see Fig. 4.5) with all SMA connectors already installed and ready to use.

Measurements have been performed on the switch to verify compliance to the specifications given in the company datasheet. Fig. 4.6 shows S parameters while switch common input $RF0$ is connected to port 1 on the VNA and $RF1$ output is connected to port 2. Insertion

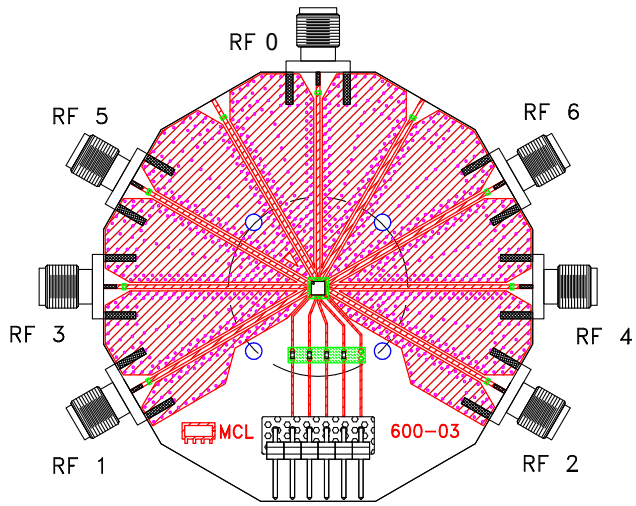

Figure 4.5 Minicircuits RF switch evaluation board [5].

loss and return loss measuremnts agree with the provider specifications (isolation was not measured). Measurements of all other ports were carried out with similar results.

4.2.1 Switch perturbation analysis

It was mentioned previously that the chosen RF switch for was of the reflective type. In other words, the output port of the switch are in short-circuit condition when they are set in the OFF position. Considering the simple model presented in Fig. 4.3, this situation would be equivalent to short-circuiting a loop probe beside the selected probe. As a consequence, there is a possibility that the magnetic flux created by the selected probe, and linked to the shorted neighboring probes, perturb the response of the selected probe. In reality, there is a section of microstrip transmission line as well as a section of coaxial transmission line in between the probe and the short-circuited output of the switch. Consequently, neighboring probes see the OFF-state switch impedance as a short circuit transformed by a line section. Maximum current will be induced in the neighboring probes if they see a short circuit, i.e. when this line section has zero length. Considering future designs where the switch will be integrated on the probe board, the worst scenario, where the short circuit is at the probe itself, is discussed here. The worst case can be simulated as in Fig. 4.7. One selected probe is scanning a wire mesh with one short-circuited parasitic probe on the left and right sides of it. In this simulation model probes are square and not rhomboid shape in order to maximaze the flux linkage.

A MoM simulation simulation software (Feko®), was used to solve the model at a frequency of 1 GHz. Two simulations have been carried out using a square grid composed by square

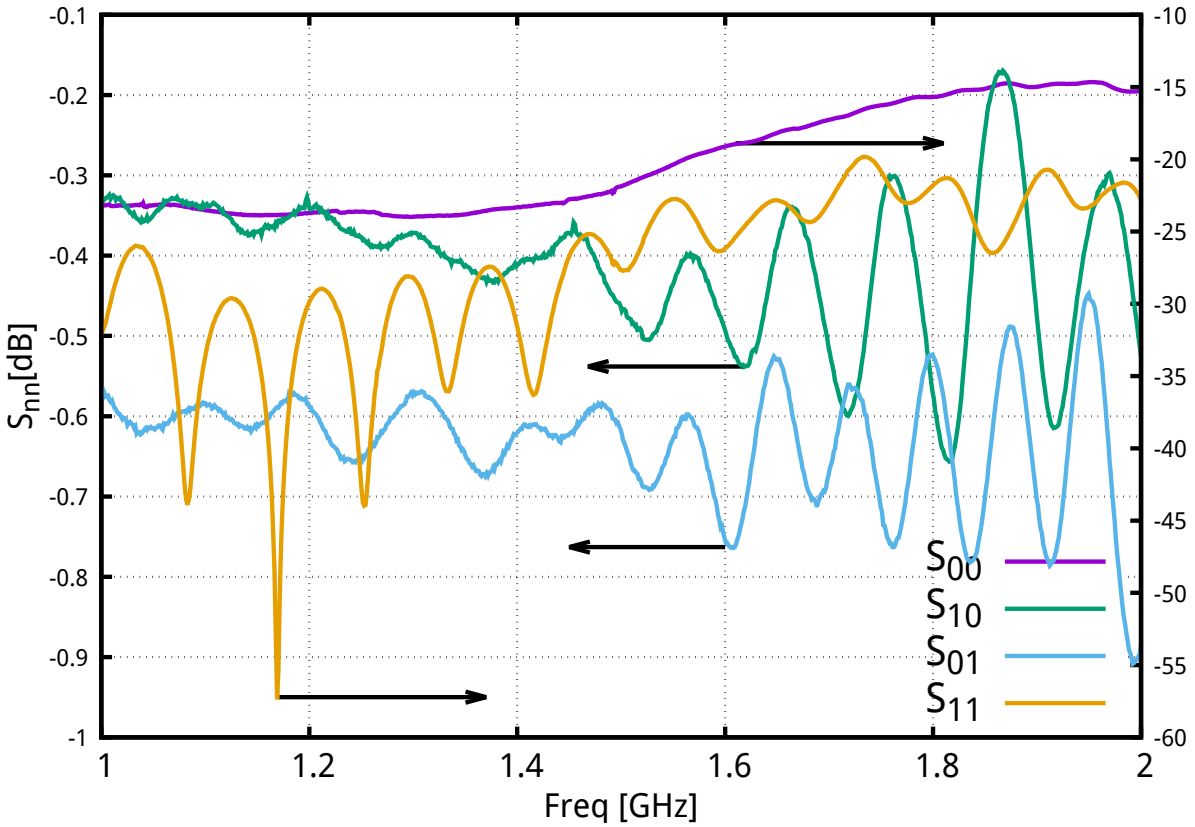

Figure 4.6 Minicircuits RF switch S parameters. $RF1$ output is selected.

cells of 1.5 mm side. The grid, along with the three probes on top of it, are built with PEC strips of 200 µm width. A 100 µm defect was placed at coordinate $x = 4.5mm$. All three probes move together in a path that pass over the defect. The input impedance of the middle probe is ploted in figure Fig. 4.8. The center probe is excited using a 50Ω port while the ports located on the neighbor probes can have two different states. In the first simulation, those ports are set to an impedance of 0Ω, so the parasitic probes become shorted loops. In a second simulation, the same structure is repeated setting a port impedance of 1 MΩ instead of 0Ω on the parasitic ports. Comparing the two simulations, a negligible difference was observed in the input reactance of the center ON-state probe as shown in 4.8. In both cases, the effect of the wire mesh defect can be clearly seen. Consequently, it is safe to say the OFF-state neighboard switches will not perturb the measurements due the magnetic coupling.

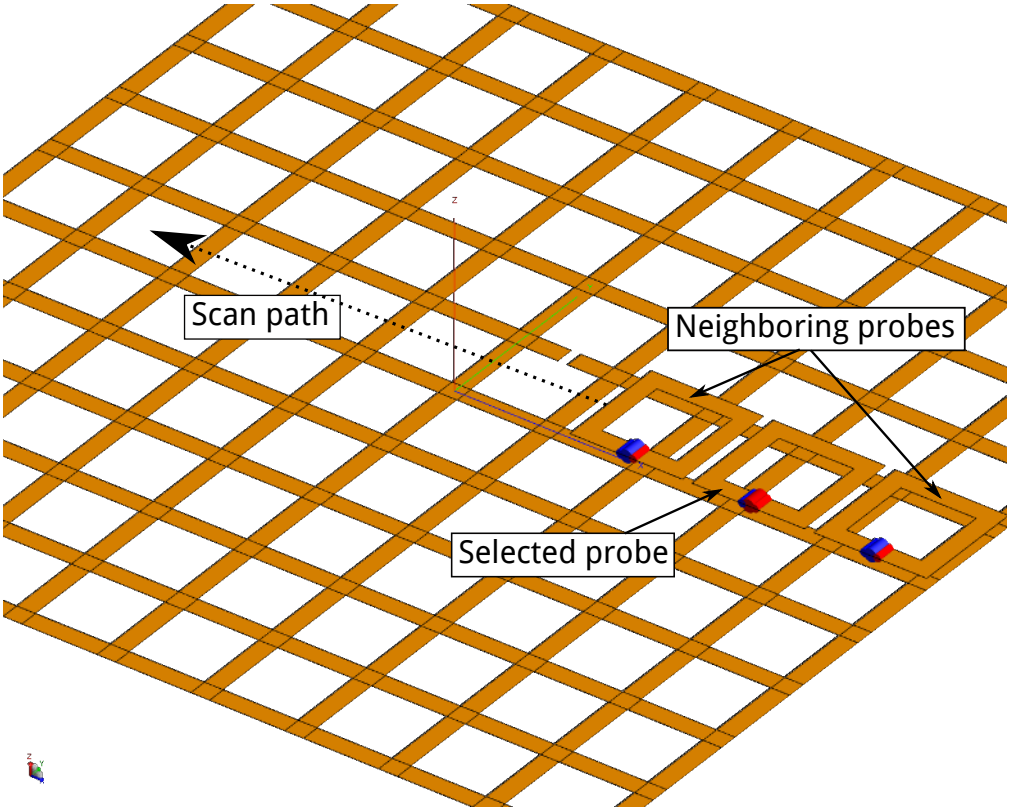

Figure 4.7 Perturbation analysis simulation model.

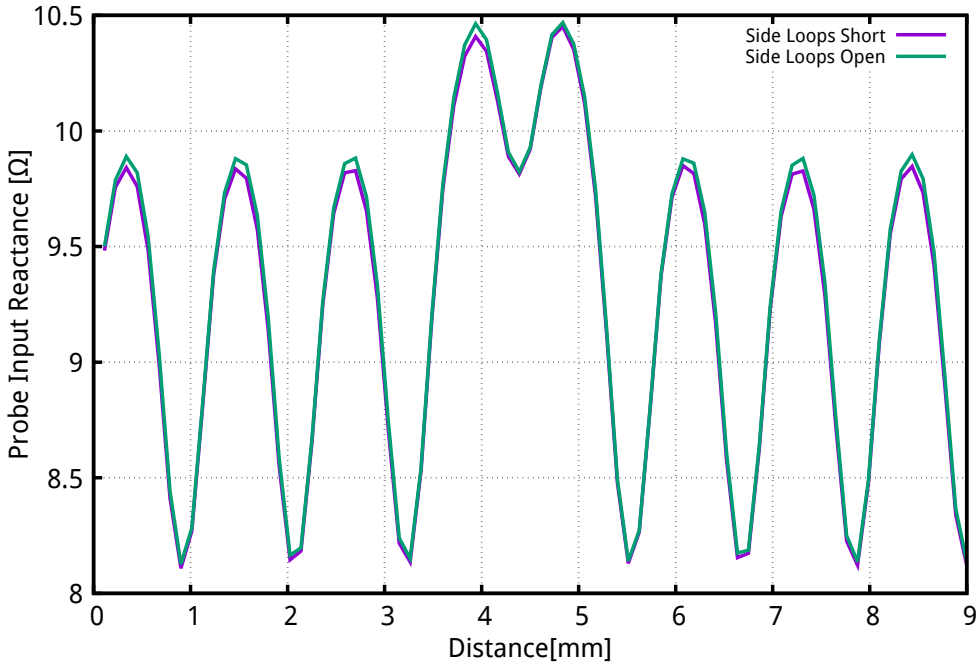

Figure 4.8 Center loop input reactance. Parasitic probes short and open.

4.3 General Purpose USB to GPIO

As presented in the first section of this chapter, the measurement set-up is controlled by a computer which communicates with other devices through USB and Ethernet interfaces. Since the selected RF switch requires CMOS control voltage levels, a "translator" from USB to General-Purpose Input/Output (GPIO) is needed to communicate with the switch board. Adafruit FT232H (Fig. 4.9), is a flexible board that contains all needed ports for the pretended application. Particularly, it packs a USB interface and 18 general purpose pins that will be used to command the switch board. A Windows® dynamic linked library (DLL) was developed so the main Matlab routine can control the FT232H board.

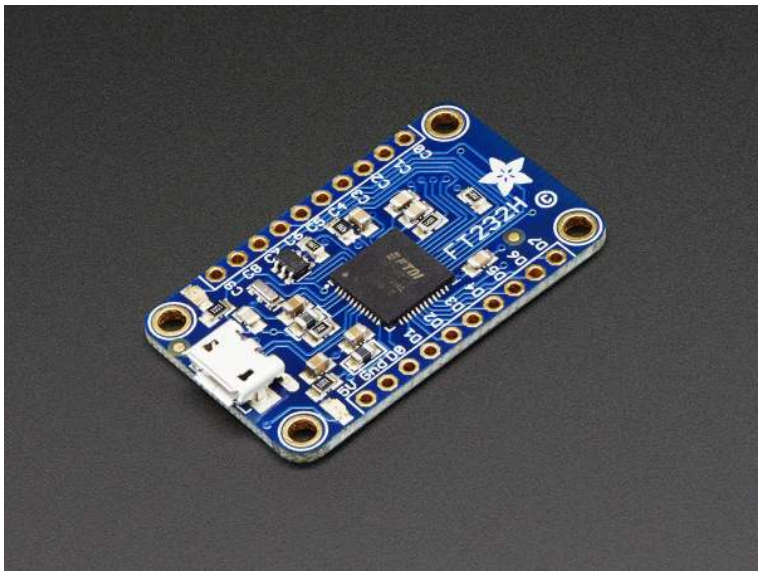

Figure 4.9 Adafruit FT232H control board.

4.4 Control software

The control software that manages the measurement set-up is essentially organized in a main routine and subroutines that are designed to perform very specific tasks among all devices (e.g., move probe station chuck, trigger VNA measurement, select a particular RF switch output). A flow chart that describes the main program is shown in Fig. 4.10. A brief description of each of the block is given below.

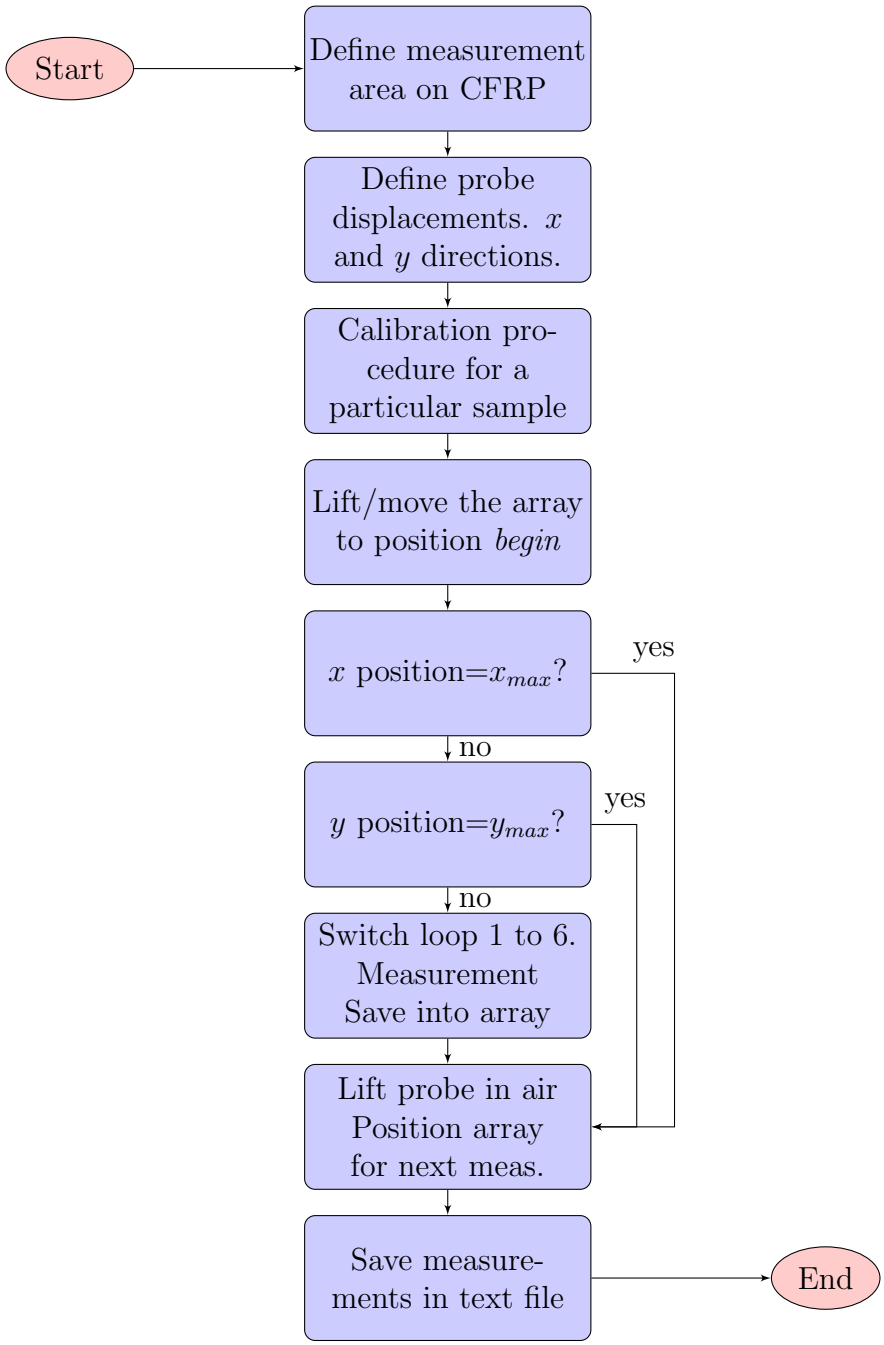

Figure 4.10 Main program flow chart.

4.4.1 Main routine auxiliary functions

- Definition of the scan area: once the sample to be measured is installed in the probe station, a smaller rectangular area needs to be defined. The array will scan this sub-region of the sample.

- Definition of δx and δy probe displacements: this parameters are the spatial sampling resolution. Typically, $LWD/4$ is used for δx and $SWD/2$ for δy.

- Calibration procedure: as it will be shown later in the measurement subsection, due to the introduction of the switch in the measurement circuit, the equivalent of an unknown series impedance is also introduced. This unknown impedance is of different values depending on the selected output. Also the path from the tip of the probe to the switch is of different length for each of the probes. The calibration subroutine finds the resonance for each of the output and sets the frequency range of the VNA segmented sweep. Further explanations are given in the next section.

- Lift probe movement: the measurements are carried out by sweeping the sample in the y direction (see Fig. 4.2). Since the array can sweep the sample only towards y positive coordinates, at the end of each measured path, the whole array needs to be detached from the sample in order to be re-positionned at the beginning of the next measurement path. Sweeping the sample towards y negative coordinates could get the probes stuck into sample irregularities causing permanent damage on the probes board.

- Switch loop: after the array moves to a new position over the sample, the switch selects each of the probes in order to take successive measurements. This is managed by a dynamic linked library routine that was coded in C++ for this purpose.

- Probe station chuck movement: during the calibration and measurement procedures the array "sweeps" the sample. In reality, the array is fixed and the sample, which is installed on the probe station chuck, shifts in discrete displacements namely δx and δy. Many routines have been designed to move the chuck in x,y and z directions as well as rotating in θ degrees. We enumerate them bellow:

  - *Move chuck $x - y$ relative to a coordinate*
  - *Move chuck $x - y$ to absolute coordinate*
  - *Move chuck z relative to a coordinate*
  - *Move chuck z to absolute coordinate*
  - *Read chuck position in absolute coordinates*

  - *Rotate chuck in θ degrees*
  - *Rotate chuck to the center*

- Save measurements: a specific S_{11} versus frequency table is recorded as a response of each of the probes and for each x, y sample coordinates. This table is saved into an array that is written in a text file for later post-processing.

4.4.2 Probe calibration subroutine

This function is in charge of configuring the VNA for each of the probes in the array, in a manner that the gathered data by all probes can be correlated in a later post-processing stage. Basically, it determines the resonance frequency accurately for each of the probes and saves it for future reference. Details on this subject will be given in the following section. A very simple block diagram of the function is shown in Fig. 4.11

The function takes the center frequency, frequency span, intermediate frequency (IF) filter bandwidth and number of data points to be measured as parameters. It uses the Standard Commands for Programmable Instruments (SCPI) specification and Matlab interfaces to program a segment sweep in the VNA.

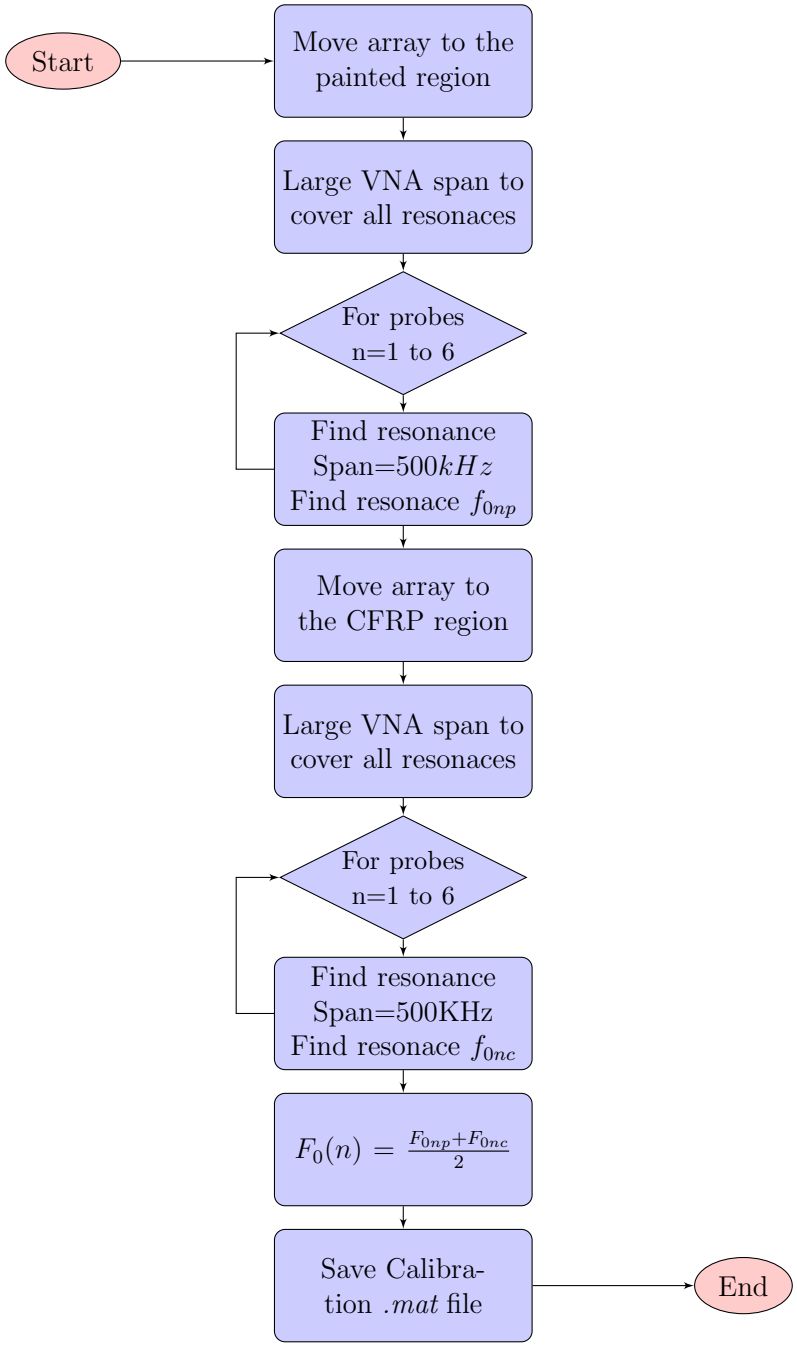

Figure 4.11 Probe calibration subroutine.

4.5 Experimental Results

4.5.1 Probe deterioration

The lab experiments that provided the images shown in this section were not obtained straightforwardly. Many attempts using different samples and difference settings were performed before reaching useful images. These many attempts implied that the probes swept over different samples many times. Some samples exhibit smooth surfaces and others irregular ones. Particularly, the surface of the sample that was struck by lightning was rough and abrasive (see Fig. 4.19). During repetitive measurements while testing this sample, with the single probe system of Chapter 3, the system stopped working as expected. The probe was identified as the defective element. In Fig. 4.12 a close-up of the printed loop is presented. The copper that forms the loop was worn away by friction so it can no longer function as a shielded loop. As a solution to this problem in a later design, a thin layer of 25 µm Kapton® Polyimide film was glued to the probes to avoid direct contact with sample surfaces and protect the probes from abrasion (see Fig. 4.13). Dupont kapton LF7012R was chosen to build the protective layer because of its unmatch durability and flexibility to conform to probes PCB. In addition, Kapton micro-thin width increases the probe-sample separation by a small percentage. Any separation between the probe from the sample would increase field attenuation and consequently decrease system sensibility. Considering a paint layer thickness of 300 µm, a protective layer of 25 µm represents an increase of approximately 10% between the probe and the wire mesh. The frequency shift excursion attenuation caused by this protective layer was experimentally found irrelevant for the purpose of this work. Many other tests over different samples validated the efficacy of this protection measure.

Figure 4.12 Worn-out probe tip.

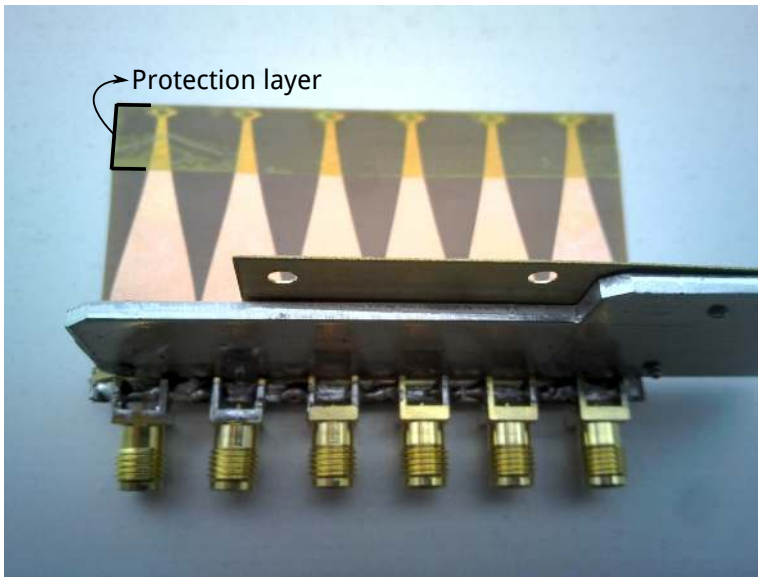

Figure 4.13 Protected array.

4.5.2 Calibration correction procedure

As mentioned in previous sections, a different signal path is introduced between the resonator and the probe each time a new probe is selected. These paths may have different loss levels and introduce different phases. Consequently, different probes positioned over the exact same location on a sample will likely give a different response, i.e. a different frequency shift of the S_{11} minimum. If no corrections are performed in the post-processing graphic construction, the result is dominated by important jumps in the resonance frequency. Fig. 4.14 shows a 3D view of the measured frequency shift of a scanned CFRP painted sample. Visual inspection of this sample shows no apparent defects. The plotted resonance frequencies are raw data provided by the VNA. Six regions can be clearly seen, each one corresponding to one of the probes in the array. As it can be observed in the image, the small frequencies shifts due to the presence of the wire mesh under paint are masked by the large frequency shifts introduced by the switch. As a consequence, a calibration procedure needs to be implemented to remove this masking effect.

The first step to address the calibration problem is to understand the resonance frequency drifts introduced by the switch for each of the probes. A measurement has been performed over a CFRP sample without wire mesh and paint layer. Fig. 4.15 shows the resonance curve for all 6 probes when they are consecutively positioned over the same point of the sample. All six resonances are included in a span of 14 MHz. It can be observed that due to the switch internal construction the six responses are distributed in pairs, consistant with the

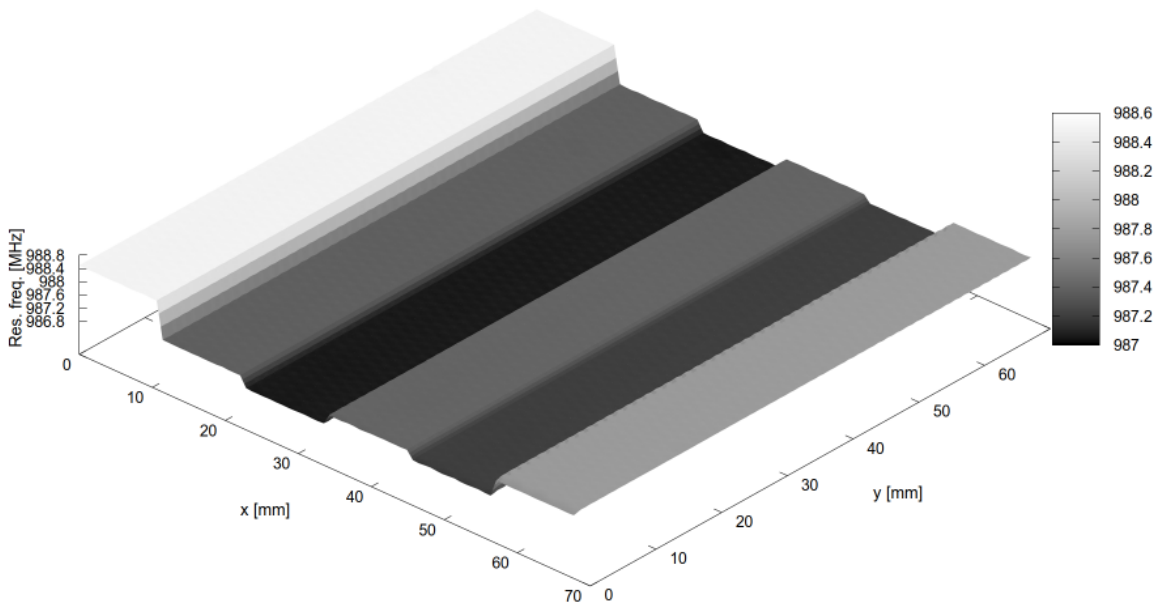

Figure 4.14 Undamaged painted CFRP sample - Uncorrected raw data.

symmetry of the switch design shown in Fig. 4.5. Since the excursions of frequency shift of any given probe are in the order of 500 kHz while measuring the wire mesh, it is obvious that these shifts are hidden by the 14 MHz variations introduced by the switch. Likewise, the frequency shifts due to presence of the wire mesh are different for each probe due to presence of the switch. In other words, the pattern of resonance frequency excursions have different amplitudes for each of the probe examining the same wire mesh. Both mentioned distortions need to be compensated by a correction algorithm.

Firstly, the calibration procedure consists in accurately determining, inside a 500 kHz span, the resonance frequency for each of the probes. A 500 kHz span has been experimentally determined as the maximum resonance frequency excursion that potentially covers all experimental measurement scenarios. That is, aircraft CFRP samples must fit in between two extremes cases, e.g. the probe over a 400 µm paint layer and probe over naked wire mesh. The calibration procedure calculates the mean value resonance frequency for all points measured by each of the 6 probes, so at the end, the procedure will determine 6 resonance frequency averages. Secondly, the calibration procedure calculates the standard deviation considering all points relieved by each probe. Again, 6 standard deviation values are calculated. Once the average resonance frequency and standard deviation values for each of the probes have been determined, corrections can be applied in a post-processing stage to equalize the data

acquired by the six probes using the following expression for probe n.

$$z(x,y)_n = \frac{f_{resonance_n}(x,y) - f_{average_n}}{f_{std_n}} \tag{4.1}$$

So, for a resonance frequency measured by probe n, that corresponds to a sample point with (x, y) coordinates, the corrected z coordinate is plotted in the in 3D equalized graphics of the wire mesh. Applying 4.1 to the data plotted in Fig. 4.14 provides corrected z coordinates that are used to built Fig. 4.16. In this figure, we can clearly see that the six saturated regions in Fig. 4.14 have disapeared. The periodic variation of the resonance frequency associated with the LSP wire mesh are now visible and usable for diagnostic. However, an alternance of slightly darker and lighter strips can still be observed along the x direction. The reason for this binary modulation is yet unknown. Since there are 12 strips (twice the number of probes), they could be due to a slight mechanical disturbance of the test setup near the middle of the sample scanning sequence. At last, it is important to notice that as a consequence of this normalization process the quantities displayed in the z axis are unit-less.

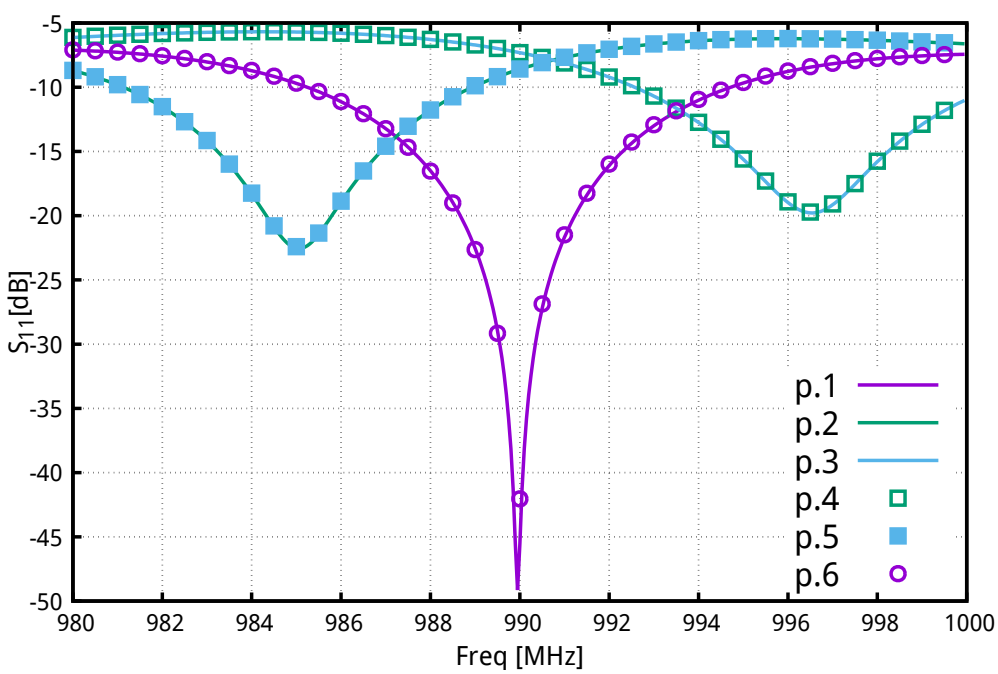

Figure 4.15 Changes in resonance frequency of each probe due to different RF signal paths in the switch.

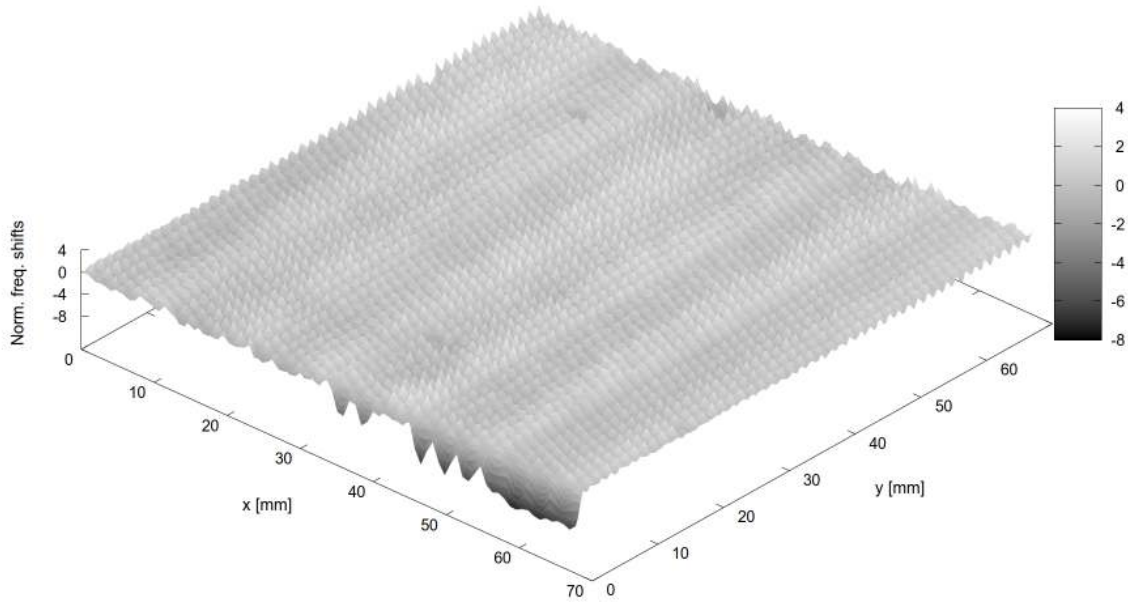

Figure 4.16 Undamaged CFRP - 3D Normalized surface.

4.5.3 Samples

In order to validate the operation of the measurement system, three samples were fabricated and tested. All of them were cut in square shape of 100mm by 100mm from a larger CFRP specimen provided by *Bombardier*. The first sample is a painted CFRP without any visible defect (see Fig. 4.17). The second one is a sample that has been fabricated by milling-off the surface of the CFRP in steps of 80 µm, over strips of 12 mm in width (see Fig. 4.18). The purpose of this sample is to provide means of comparison in the same measurement run, a perfectly healthy wire mesh region (the first 12 mm of the sample are unaltered) against a raw carbon region produced by removing layers of increasing thickness of the paint and wire mesh. The sensibility of the technique can be evaluated here since the paint is removed in discrete steps of 80 µm for the first 4 levels. From the 5th level, even part of the wire mesh is removed. It should be kept in mind however that the layers in the sample and the whole sample itself may not be perfectly planar, therefore the amount of milling is not perfectly uniform over each 12 mm strip. The third sample constitutes a piece of CFRP that has been struck by lightning (Fig. 4.17). Using naked-eye inspection it can be observed that the wire mesh has been melted over a large section of the sample to dissipate the energy that was contained in the strike. The measurements will be able to asses the condition of the mesh underneath the painted layer. This sample also contains holes that were drilled to fit rivets.

The condition of the wire mesh around holes is relevant to ensure a continuous electrical path with the aircraft backbone ground.

4.5.4 Sample measurements

Undamaged Sample

Prior to installing the undamaged sample on the probe station chuck, a small deep cut, less than 2 mm long, was practiced on the sample with an exacto knife at coordinates $x = 36mm$, $y = 15mm$. The purpose of this action is to asses the ability of the technique to detect one cut strand. A 3D image of the scanned surface is presented if Fig. 4.20.

Referring to the previous figure, arrows have been added near regions that exhibit disturbances of the periodic response caused by de underlying wire mesh. These regions correspond to possible defects in the wire mesh. Given that the size of the defects are relatively very small compared to the scan surface, a 3D plot does not constitute the best tool to reveal the flaws, albeit it can provide an overall status of the mesh. A contour image in Fig. 4.21 presents a more clear view of disturbed regions (highlighted with red circles), possibly corresponding to cut strands in the sample. The cut strand that was inflicted intentionally (labeled "deep cut"), can clearly be distinguished at $x, y = 36, 15mm$. Moreover, the are two other irregularities in the mesh that have been discovered in the sample at coordinates $x, y = 19, 57mm$ and $x, y = 28, 68mm$. These flaws need to be validated by x-rays techniques. Due to Covid19 this validation could not be performed.

Multi-Step Sample

In same fashion as in the previous case, the surface plot of corrected frequency shifts of a muti-step sample is displayed in Fig. 4.22 and the contour plot that corresponds to the sample is shown in Fig. 4.23. In these plots, the thickness variation due to milling is along the y direction, whereas the 6 probes are laid along the x direction and scan along the y direction. For this sample, the average and standard deviation values that were used to normalize the image, were the ones extracted from the previous case (undamaged sample). Otherwise stated, the undamaged sample is used as a calibration specimen. Here, only 6 steps out of 8 that are contained in the sample are displayed. The first step, where the paint is undamaged, covers values of y between 0 to $12mm$. This region is represented by lowest peaks. In the following steps, peaks increase in height as layers of materials (at first mostly paint) are milled at a rate of 80 µm per step. In the 5th and 6th steps, the wire mesh is clearly exposed. From the same image, it can also be noticed that the applied milling process is not

Figure 4.17 Undamaged CFRP sample. The ruler scale is in cm.

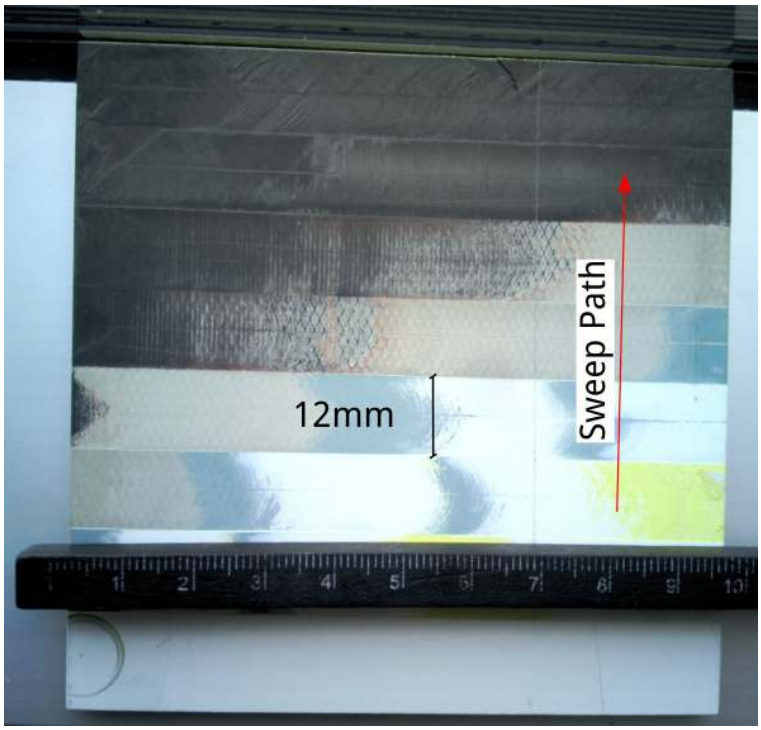

Figure 4.18 8 steps milled sample in strips of $12mm$.

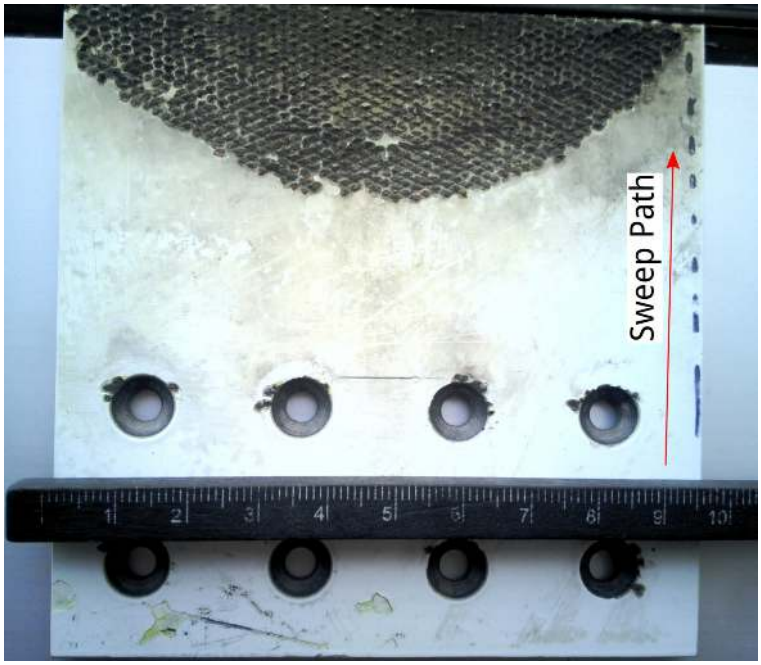

Figure 4.19 CFRP sample damaged by lightning strike.

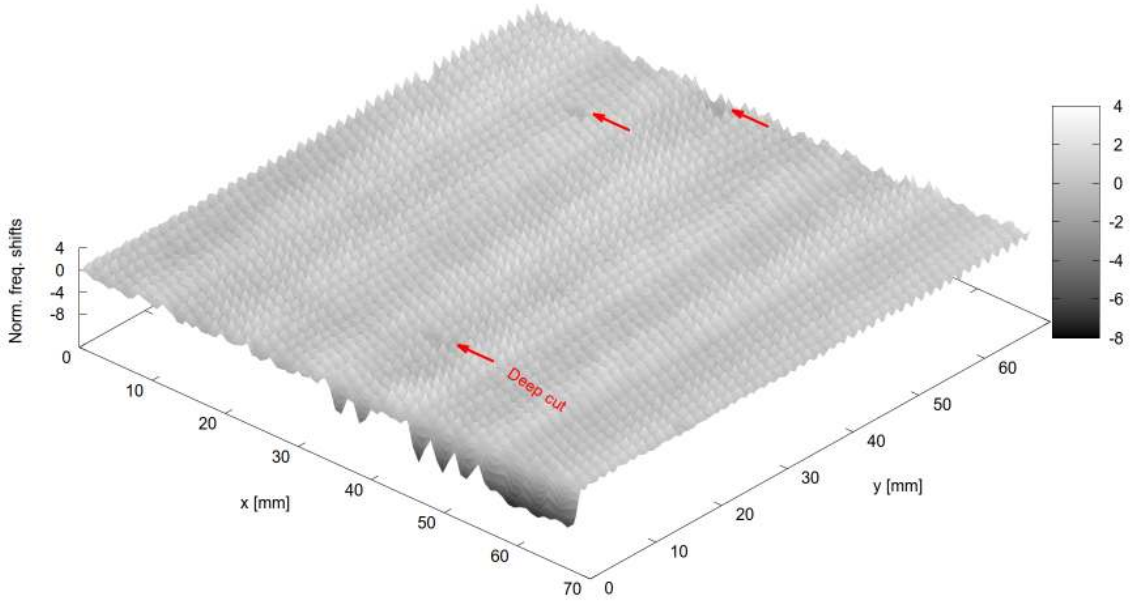

Figure 4.20 Undamaged CFRP with deep cut - 3D Normalized frequency shift surface.

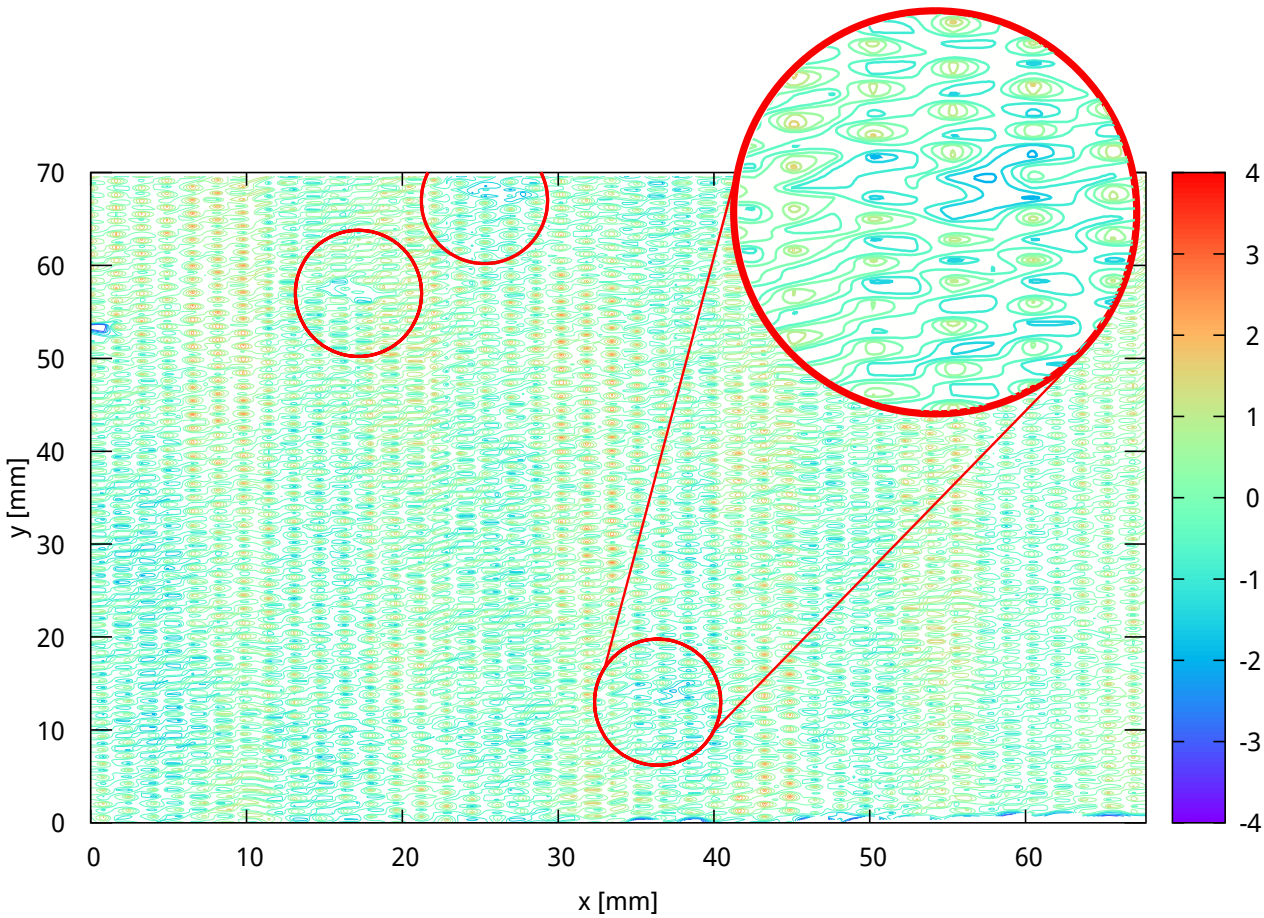

Figure 4.21 Undamaged CFRP. Normalized frequency shift contours. The inset shows a zoom of the region near the deep cut.

uniform within each strip. More material has been removed on the left side of the sample than on the right side (towards $x = 100mm$) of it, in each of the steps. This is evident in steps 5th and 6th where on the left side the mesh is completely removed (plateau) but on the right side part the mesh is still exposed (high peak pattern). Related to Fig. 4.23, it is visible that no close contours are located on the left part of 5th step as well as in almost the entire area of step 6, which implies naked CFRP material or wire mesh completely absent.

One last observation concerning a modulation effect in Fig. 4.23 needs to be made. This effect consist in different peak level along the x coordinate inside a sub-region scaned by an individual probe. For instance, the highlighted shaded orange polygonal region in the first step, presents higher peaks levels than on the sides of this region. It is believed that this is due to lack of orthogonality between the scanning path of the probe array and the long diamond diagonal line that composed the wire mesh. This modulation effect can be perceived inside each step. On the contrary, the sub-regions scanned by each of the probes are evident

because the uneven transitions between each of them (at $x = 12mm$, $x = 23mm$, etc..). This is better noticed in the first step where the sample is not unaltered.

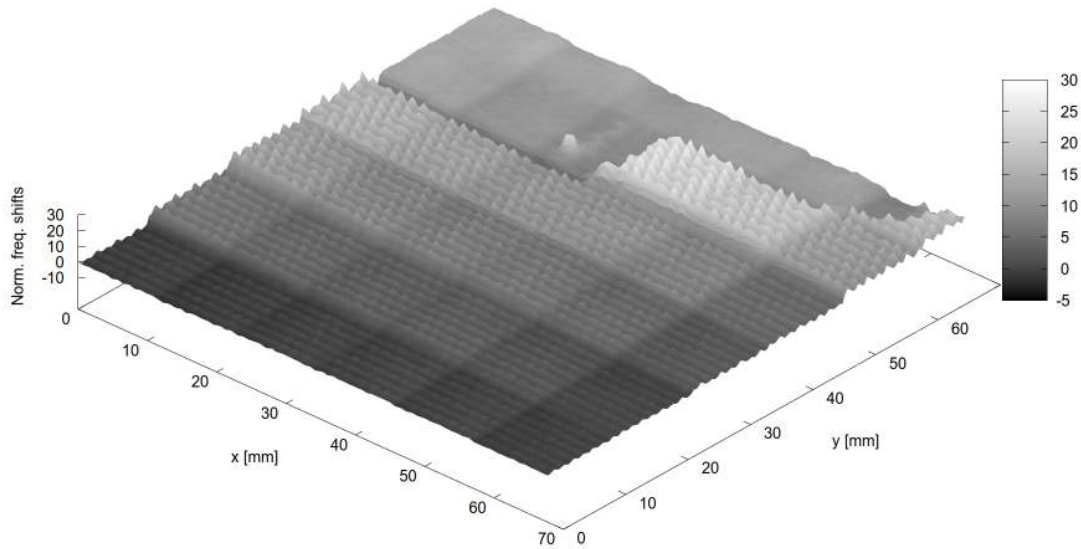

Figure 4.22 Stepped CFRP sample - 3D Normalized frequency shift surface.

Sample damaged by lightning strike

The damaged sample contains two 2 rows of 4 wholes each, situated in the bottom part of the sample (see Fig. 4.19). In the upper part there is the damaged area where the wire mesh has been evaporated due to an inflicted lightning strike. A 3D image of the sample is shown Fig. 4.24. A contour plot of the same measurement is displayed in Fig. 4.25. It is important to mention that due to a power failure during the measurement, some parts of the sample were not measured. These parts appear as white lines parallel to the y axis in both figures.

The scan in Fig. 4.24 covers only 70mm of the 100mm wide sample. So, 4 holes are clearly visible and only part of the other 4 holes has been swept by the probe array. Also, it can be noticed in Fig. 4.25 that some strands are cut around the two top left holes. Finally, the extent of the damage in the area where the wire mesh has burned is described by an arc in the top of the sample, where a regular contour pattern in interrupted. Some residue of copper is still on top of the burned zone and can be perceived by the red contours located mainly on the top right of the sample ($x, y = 50, 80mm$).

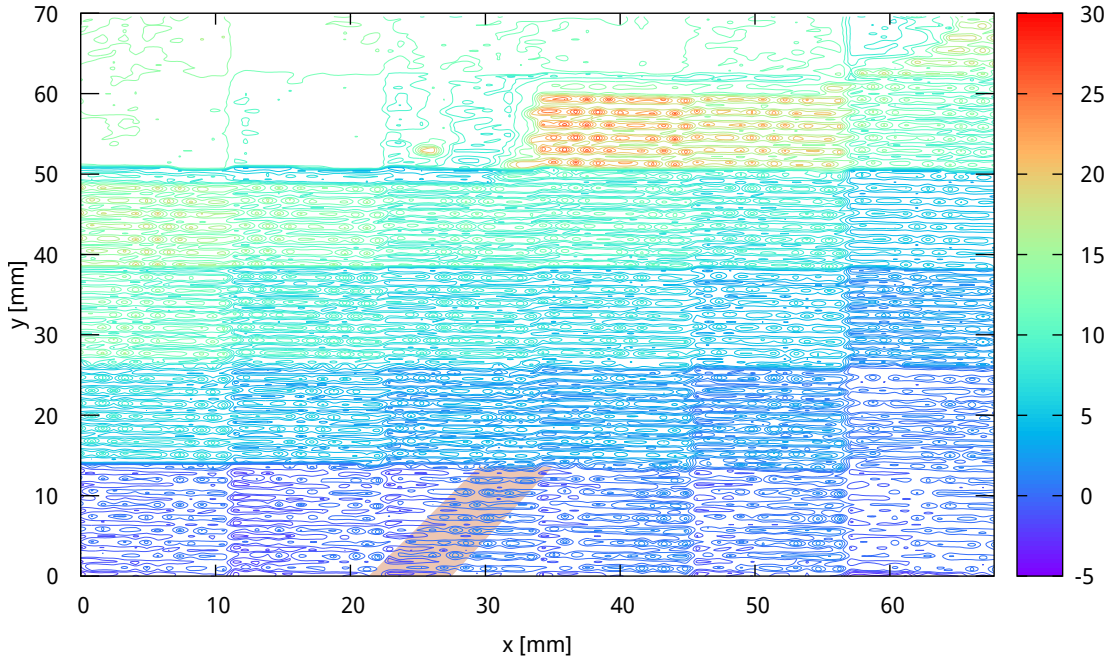

Figure 4.23 Stepped CFRP sample. Normalized frequency shift contours.

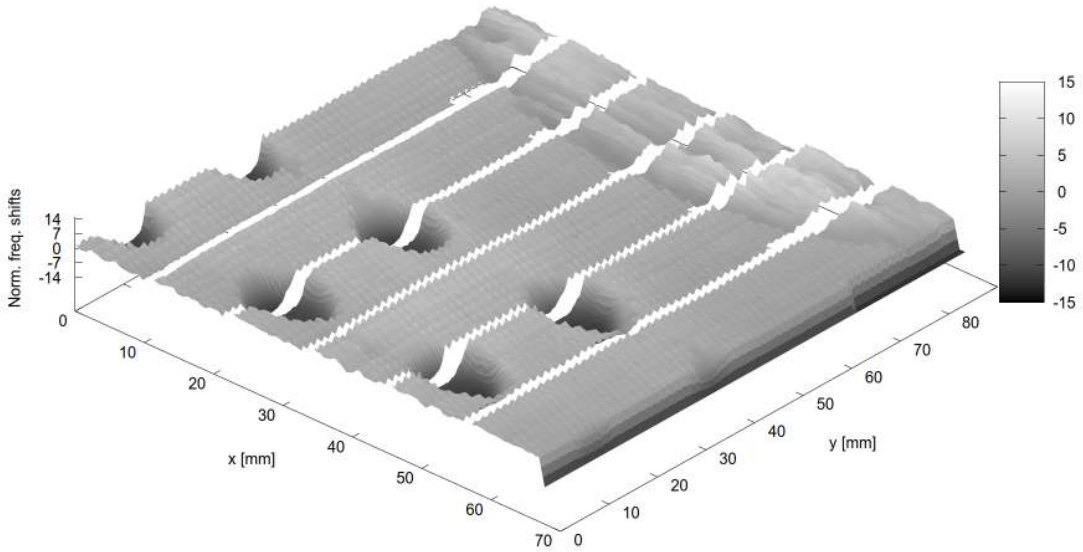

Figure 4.24 CFRP sample damaged by lightning strike - 3D Normalized frequency shift surface.

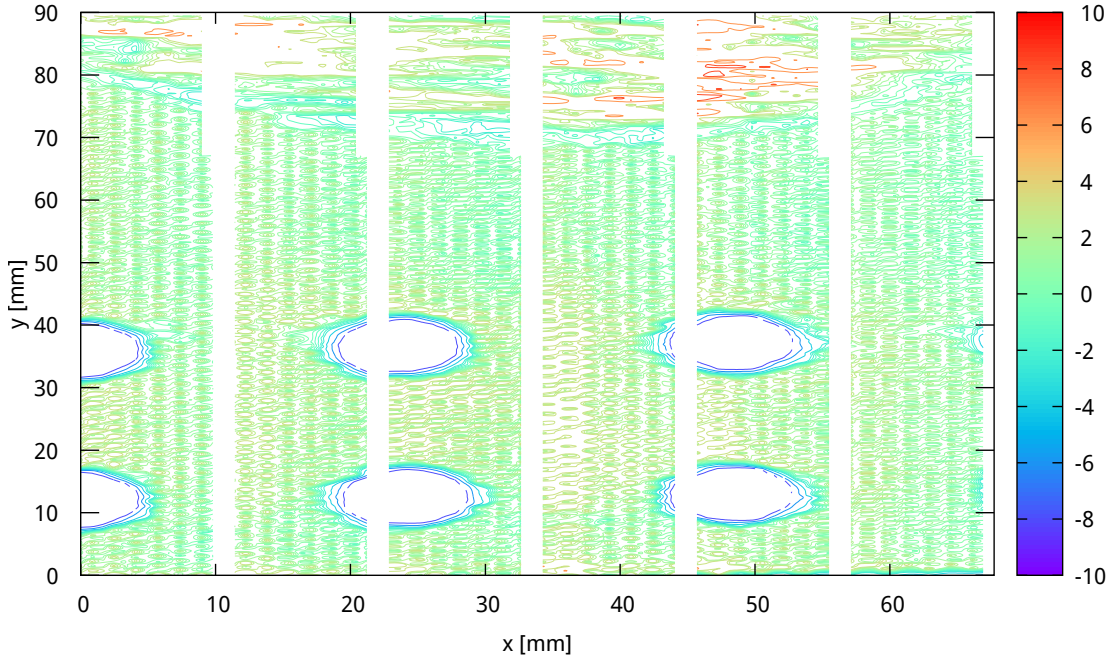

Figure 4.25 CFRP sample damage by lightning. Normalized frequency shift contours.

4.6 Conclusion

In this chapter, a technique to scan large surfaces while reducing the scanning time is presented. An array of 6 probes integrated in the same PCB is used to increase scan surface coverage. Those probes are linked to the resonator by an SP6T RF switch. A measurement set-up as well as its control software was described by block diagrams. The main routines that composed this software were also explained. The complete software code is listed in Annex A. Since there was a risk of flux disturbance while probes are placed close together, a perturbation analysis was realized through simulations. It was concluded that there is a negligible impedance alteration in the selected probe by the neighboring ones.

A protective layer was proposed to avoid the probes to deteriorate through repetitive measurements over possibly abrasive samples. A new array with protective layer was proven effective in characterizing CFRP samples. A calibration procedure was reported that allow equalization of the measurement obtained by each of the probes. This calibration procedure was used to adjust data obtained by all probes to create useful plots of the underlying wire mesh.

Experimental results were presented using three difference CFRP samples namely, undamaged, multi-step and damage by lightning. Very small flaws (in the order of 2 mm were successfully found using the array in what it was believed by visual inspection, an undamaged sample. A contrast measurement of all possible measurement scenarios was shown using the multi-step sample. Here, it was possible to compare regions cover by paint layers of different thicknesses in the same measurement run. In the end, a damage sample struck by lightning was analyzed. Clear limits of the damage areas were found. Additionally, very small defects around rivet holes were also spotted. Concluding, it could be said with certainty that the effectiveness of the array to spot small flaws while scanning large surfaces was demonstrated.

CHAPTER 5 PROBE MEASUREMENT ACCELERATION TECHNIQUE

5.1 Introduction

It has been shown in Chapter 3 that a magnetic probe presents enough resolution to detect small defects in the LSP wire mesh under the aircraft paint. Changing frequency shifts patterns of the resonator on every position permits to spot anomalies in the mesh. As stated in previous chapters, the magnitude of S_{11} coefficient is measured at every position of the probe relative to the sample. By post-processing the measured data, the frequency where the minimum of the $|S_{11}|$ occurs (resonance frequency) can be plotted versus the probe position along the chosen path. It is important to notice that these measurements are performed in a small fraction of the resonant curve or Q circle, namely over a bandwidth of 500 kHz. In order to have precise frequency discrimination and thus being able to detect small defects, the IF filter bandwidth needs to be relatively narrow-band, in the order 2 kHz. In addition, sweeps of 400 frequency points are programmed in the network analyzer for the magnetic probe. The electric probe requires 800 measurement points due to reduced measured frequency shifts. All the previous settings play against the speed of the measurements. In respect to the magnetic probe, the PNA takes 0.9 second per probe for each sampled position. The bottleneck to higher measurement speed is the PNA acquisition time.

In Chapter 4, an attempt to speed-up measurements in large surfaces has been implemented through the use of probes array. Six probes swept the sample in parallel allowing the network analyzer to make six readings at every new position. Although the gain is speed seems to be evident, further improvements are proposed in this chapter to speed up single measurements.

In the following sections a method to accelerate PNA measurements is presented. It is applicable to the single probe and probe array measurement schemes, but its proof of concept will be done for the single probe case only. This technique can speed up measurements quite significantly. The time for one measurement is divided by 80, by reducing the number of frequency points from 400 to only 5 points for each position. At the same time, the technique also allow to quantify the quality factor and coupling coefficient of the resonant structure. Quality factor and coupling coefficient are typically exploited to detect changes in material losses. For instance, this technique could potentially be useful to detect water filtration into CFRP materials.

Determination of Q factor is a well studied subject. Accurate determination of Q factor is needed particularly when electrical properties of a material, such as loss tangent or surface

resistivity, are being measured inside a resonant cavity. It is also important when a resonator is characterized for later application in filters or oscillators. Much research work was performed on the subject of measuring the unloaded quality factor, Q_o, loaded quality factor, Q_L, and coupling coefficient κ. Ginzton [52] was one of the pioneers in Q measurements. In 1958, he presented a graphical method to determine the Q factor of a cavity in the presence of coupling losses [53]. Later, with the advent of vector network analyzers, a plethora of different methods have been developed by many authors [54]. Darko Kajfez was one of the most productive authors in the subject. In one of his first papers [39] he adapted Ginzton's method to the use of a network analyzer. He described a method to find the unloaded Q factor by using the diameter of the Q circle and the phase difference of two conveniently located points on the circle. The circle observed in the complex plane when the input impedance of a resonant microwave cavity is measured as a function of frequency is named Q circle. Many other authors published related work on the subject in the 90s. Sanchez, Martin and Zamarro [55] developed a vectorial automatic technique to characterize a dielectric resonator coupled to a 50Ω microstripline. They fit experimental data into a circle equation and solved the equation system afterwards to finally obtain the coupling coefficient and quality factor. The common denominator of most of these numerical techniques is the solution of the unloaded Q factor, while the resonator itself is loaded by the measurement circuit.

The procedure perfected by Kajfez through many papers since 1984 was a technique that fits measured data to a fractional linear transformation [56]. In contrast with other works on the subject, he implemented an interactive algorithm that allows finding the precise cavity resonant frequency based on a few measured frequency points. Since measurement time increases in proportionally with the number of frequency points, the overall time would be drastically reduced if the frequency points decrease from 400 to only 5. The technique that is explained in the following paragraphs and published in 1995 by Kajfez, has been chosen to track the resonant frequency of the coaxial line probe ended resonator in the experimental set-up implemented in Chapter 3.

5.1.1 Equivalent circuit

The circuit that represents our measurement set-up is replicated from 3.2 in Fig. 5.1. In Fig. 5.2 a general model of the circuit is presented. The coupling capacitor has been replaced by a general coupling network characterized by the chain parameters $ABCD$. In order to simplify the understanding of the technique the coupling network is assumed to be lossless. This is a valid assumption since in practice the losses in the resonator are dominant. The coaxial resonator and probe are modeled by a lumped element resonator where the losses

are taken into account by conductance G_o. In the figure, the admittance that "loads" the resonator is represented by Y_{ex} and the one that "loads" the network as Y_r (the unloaded resonant admittance). Also, the input reflection coefficient in port 1 and the impedance of the generator (R_c) appear in the same figure.

In the following paragraphs, the main lines of the Kajfez's paper will be provided. Some details on his derivation are presented here for the benefit of the reader. It is not the objective of this work to neither analyze nor criticize the techniques to measure the quality factor. For that reason, only the main formulations will be described. Additionally, the meaning of different variables that intervene in formulation will be explained with the help explanatory graphs.

With respect to Fig. 5.2, the resonator itself can be characterized by its resonant frequency, ω_0 and quality factor, Q_0. This resonator is loaded by an external circuit with admittance Y_{ex}. In the same fashion, the resonator is loading the two-port by and admittance Y_r.

The admittance of the unloaded resonator is:

$$Y_r = G_0 \left(1 + jQ_0 2\frac{\omega - \omega_0}{\omega_0}\right) \tag{5.1}$$

The admittance of the external circuit is:

$$Y_{ex} = \frac{A + CR_c}{B + DR_c} = G_{ex} + jB_{ex} \tag{5.2}$$

It is important to notice here that since the network is lossless and reciprocal, A and D are real and B and C are imaginary. Also, $AD - BC$=1.

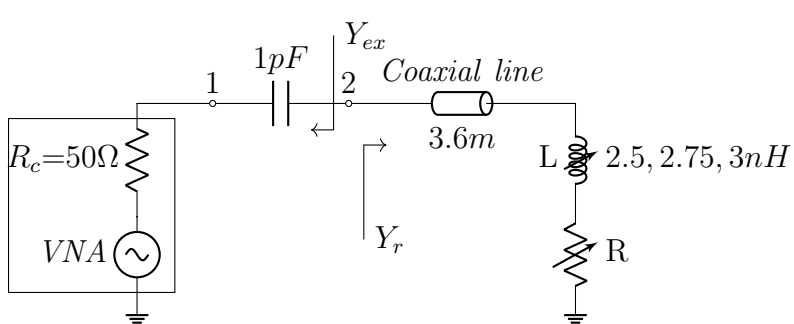

Figure 5.1 ADS set-up simplified model.

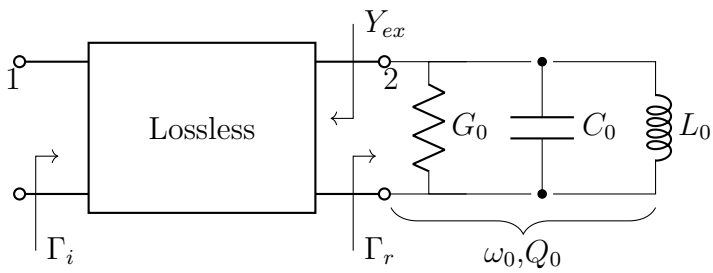

Figure 5.2 Resonator coupled to the source by a lossless two-port.

The admitance of the loaded resonator is:

$$Y_L = Y_{ex} + Y_r = G_0 + G_{ex} + j\left(G_0 Q_o 2\frac{\omega - \omega_0}{\omega_0} + B_{ex}\right) \tag{5.3}$$

The imaginary part of the above expression vanishes at the following frequency:

$$\omega_L = \omega_0(1 - \frac{B_{ex}}{2Q_0 G_0}) \tag{5.4}$$

Therefore the loaded resonance frequency is ω_L. The external admittance Y_{ex} loads the resonant circuit so that the loaded admittance (parallel combination of Y_{ex} and Y_r) becomes as follows:

$$Y_L = Y_{ex} + Y_r = (G_0 + G_{ex})\left(1 + jQ_L 2\frac{\omega - \omega_L}{\omega_0}\right) \tag{5.5}$$

Notice that (5.5) is written in terms of the loaded quality factor Q_L instead of Q_0 appearing in (5.1). The loaded Q factor Q_L has been defined in the following way:

$$Q_L = Q_0 \frac{G_0}{G_0 + G_{ex}} \tag{5.6}$$

The input reflection coefficient at port 1 in Fig. 5.2 is:

$$\Gamma_i = \frac{Z_i - R_c}{Z_i + R_c} \tag{5.7}$$

Z_i can be expressed in terms $ABCD$ parameters as:

$$Z_i = \frac{A + BY_r}{C + DY_r} \tag{5.8}$$

The input reflection coefficient is:

$$\Gamma_i = \frac{KY_r + L}{MY_r + 1} \tag{5.9}$$

where K,L and M are:

$$K = \frac{B - DR_c}{A + CR_c} \quad (5.10) \qquad L = \frac{A - CR_c}{A + CR_c} \quad (5.11) \qquad M = \frac{B + DR_c}{A + CR_c} \quad (5.12)$$

Equation (5.9) can be expressed in the following form:

$$\Gamma_i = \frac{K}{M} + \frac{L - K/M}{M} \frac{1}{Y_r + 1/M} \tag{5.13}$$

We can analyze each term on equation (5.13). Firstly the term $1/M$, in the denominator of the second term, is the same as (5.2), so $Y_r + 1/M$ is equal to $Y_r + Y_{ex}$, which is nothing but Y_L. Secondly, if Y_r tends to infinity, Γ_i tends to K/M, so this first term represents the detuned input reflection coefficient. It can be written as:

$$\Gamma_s = \Gamma_i(Y_r \to \infty) = \frac{K}{M} = \frac{B - DR_c}{B + DR_c} \tag{5.14}$$

Considering the B is pure imaginary and D is pure real number, the absolute value and phase angle of the Γ_s are:

$$|\Gamma_s| = 1 \quad (5.15) \qquad \angle\Gamma_s = -2\delta + \pi \quad (5.16) \qquad \delta = tan^{-1}\frac{B}{DR_c} \quad (5.17)$$

Lastly, the missing term can be developed as follows:

$$\frac{L - K/M}{M} = \frac{2R_c}{(B + DR_c)^2} \tag{5.18}$$

Where the absolute value and phase angle of the last expression are:

$$\frac{2R_c}{|B + DR_c|^2} = 2G_{ex} \quad (5.19) \qquad -2tan^{-1}\frac{B}{DR_c} = -2\delta \quad (5.20)$$

As a consequence, this last angle is the same as $\angle\Gamma_s$ but rotated by π. Concluding, the expression for Γ_i can be rewritten as:

$$\Gamma_i = \Gamma_s + \frac{2G_{ex}}{(G_o + G_{ex})} \frac{de^{-j2\delta}}{\left(1 + jQ_L 2\frac{\omega-\omega_L}{\omega_0}\right)} \tag{5.21}$$

Defining the diameter d and its relation to the coupling coefficients κ as:

$$d = \frac{2G_{ex}}{G_o + G_{ex}} = \frac{2\kappa}{1+\kappa} \tag{5.22}$$

(5.21) can be rewritten as:

$$\Gamma_i = \Gamma_s + \frac{de^{-j2\delta}}{1 + jQ_L 2\frac{\omega-\omega_L}{\omega_0}} \tag{5.23}$$

Equation 5.23 can be interpreted as the vectorial addition of two term. The first term is the detuned reflection coefficient Γ_s. It is defined to be the limiting value of Γ_i when Y_r tends to infinity. The second term represents a point in the quality circle of diameter d that is rotated by angle of -2δ counterclockwise in the complex plane. See Fig. 5.3. Moreover, the detuned reflection coefficient Γ_s, the center Γ_c and Γ_L are located on the same straight line in a way that the following relation is verified:

$$\Gamma_L - \Gamma_c = \Gamma_c - \Gamma_s \tag{5.24}$$

The later equation is utilized in the iterative procedure explained in the following section.

Three conditions of coupling can be defined. If the Q circle diameter is larger than unity we have and over-coupled case. For an under-coupled resonator, as in the example in Fig. 5.3, the diameter is smaller than unity. Lastly, critical coupling is the condition where Q circle passes through the center of the Smith chart. It is also important to notice that because the coupling network was considered lossless, the Q circle is tangential to the edge of the Smith chart. The Q circle would not touch the border of the Smith chart if losses in the coupling network were considered.

5.1.2 Fractional Linear Transformation curve fitting

The curve fitting procedure in use in this chapter is based on the paper published by D. Kajfez in 1975 [57]. In this work, a procedure to fit a large number (> 3) of experimental data points to a fractional linear transformation applied to reciprocal two port networks is described.

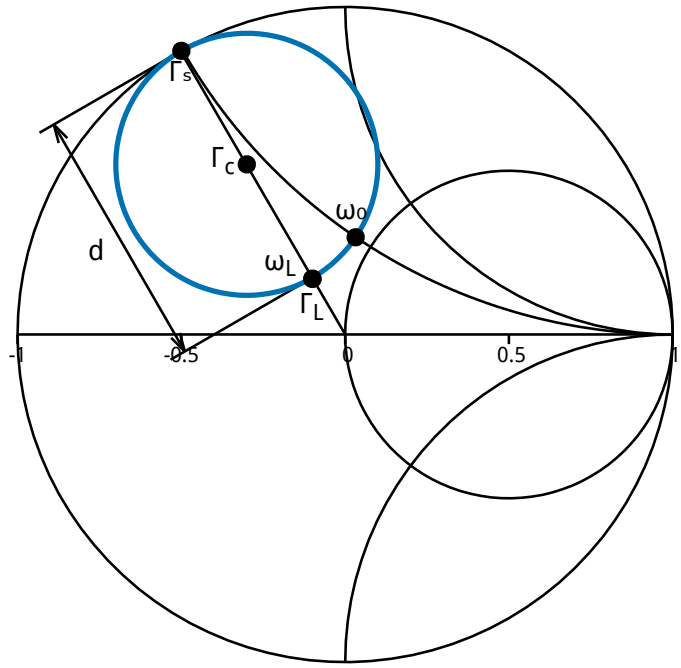

Figure 5.3 Input reflection coefficient as a function of frequency.

At the end of the procedure, the network can be characterized through the calculation of transformation coefficients. The required computing power is very small considering that the whole procedure requires only the inversion of a 3x3 matrix.

Generally speaking, a common property of linear two-port networks is that a given variable z can be transformed into the variable w according to the following linear transformation.

$$w = \frac{a_1 z + a_2}{a_3 z + 1} \tag{5.25}$$

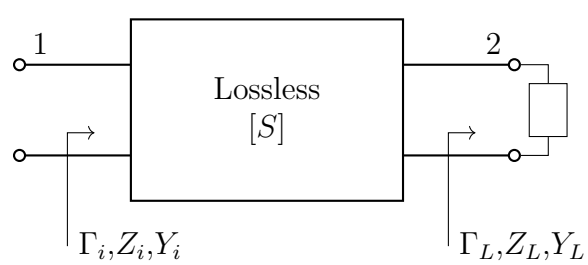

Figure 5.4 Generic lossless two-port network.

For example, in the network shown in Fig. 5.4, the relationship between Γ_i and Γ_L is (see [58]):

$$\Gamma_i = \frac{(S_{12}S_{21} - S_{11}S_{22})\Gamma_L + S_{11}}{1 - S_{22}\Gamma_L} \tag{5.26}$$

where the scattering parameters of the lossless box are used. If for example, we replace Γ_L by the independent variable z and Γ_i by w, then the coefficients a_n are defined by the scattering parameters as follows:

$$a_1 = S_{12}S_{21} - S_{11}S_{22} \quad (5.27) \qquad a_2 = S_{11} \quad (5.28) \qquad a_3 = -S_{22} \quad (5.29)$$

Since there are three unknown coefficients at least three data pairs (w, z) are need to solve the system. In most cases more data points are available, then, the system would be over-determined. Summarizing, it is an over-determined curve-fitting problem where the "curve" is a fractional lineal transformation from a complex variable z to a complex variable w. Once the transformation coefficients are determined the network is fully specified.

Equation solution

Equation 5.25 can be re-written in the following manner:

$$-a_1 z - a_2 + a_3 wz + w = 0 \tag{5.30}$$

As indicated before, z is the independent variable and w is the dependent one. For instance, z could represent the frequency and w a reflection coefficient. In this context we could have N measurements of pairs (z_n,w_n). Since measurement error is always present in practice, for any nth measurement the result would be slightly different from zero (ϵ). So 5.30 would become:

$$a_1 z_n - a_2 + a_3 w_n z_n + w_n = \epsilon \tag{5.31}$$

If we include N measurements, 5.31 would be a system of N equations and 3 unknowns. The last equation can be rearranged in a matrix form by defining 3 x N as follows.

$$\boldsymbol{X_{3,N}} = \begin{pmatrix} z_1^* & z_2^* & \cdots & z_n^* \\ 1 & 1 & \cdots & 1 \\ -w_1^* z_1^* & -w_2^* z_2^* & \cdots & -w_n^* z_n^* \end{pmatrix} \tag{5.32}$$

where $*$ indicates complex conjugate.

The complex column vectors $\boldsymbol{w}$,$\boldsymbol{\epsilon}$ and $\boldsymbol{a}$ are:

$$\boldsymbol{w} = \begin{pmatrix} w_1 \\ w_2 \\ \vdots \\ w_N \end{pmatrix} \quad (5.33) \qquad \boldsymbol{\epsilon} = \begin{pmatrix} \epsilon_1 \\ \epsilon_2 \\ \vdots \\ \epsilon_N \end{pmatrix} \quad (5.34) \qquad \boldsymbol{a} = \begin{pmatrix} a_1 \\ a_2 \\ a_3 \end{pmatrix} \quad (5.35)$$

Now, the system can be reformulated as:

$$\boldsymbol{\epsilon} = \boldsymbol{w} - \boldsymbol{X}^{\intercal}_{\boldsymbol{3,N}}\boldsymbol{a} \tag{5.36}$$

Where the symbol $\boldsymbol{X}^{\intercal}$ denotes the transpose conjugate of $\boldsymbol{X}$.

To each measurement one may assign a weight p_n, which is a way to emphasize that certain measurement are more accurate than others. The weight matrix $\boldsymbol{P}$ can be written as:

$$\boldsymbol{P} = \begin{pmatrix} p_1 & 0 & \cdots & 0 \\ 0 & p_2 & \cdots & 0 \\ \vdots & \vdots & \ddots & \vdots \\ 0 & 0 & \cdots & p_N \end{pmatrix} \tag{5.37}$$

Solving 5.31 by the principle of least squares leads to an expression where the variable to be minimized ($\boldsymbol{\epsilon}$) disappears :

$$\boldsymbol{XPX}^{\intercal}\boldsymbol{a} = \boldsymbol{XPw} \tag{5.38}$$

The matrix $\boldsymbol{XPX}^{\intercal}$ is a 3×3 matrix than can be written for convenience as:

$$\boldsymbol{C} = \boldsymbol{XPX}^{\intercal} \tag{5.39}$$

Also, the vector in the right-hand side of 5.38 will be denoted by:

$$\boldsymbol{q} = \boldsymbol{XPw} \tag{5.40}$$

The equation and its solution are now written as:

$$\boldsymbol{Ca} = \boldsymbol{q} \qquad (5.41) \qquad\qquad \boldsymbol{a} = \boldsymbol{C^{-1}q} \qquad (5.42)$$

Now that that a procedure has been established to solve a general over-determined system, the previous equation will be applied to the original problem where ω is the independent variable and Γ_i the measured input reflection coefficient. Equation 5.23 can be re-written in the form of a fractional linear transformation:

$$\Gamma_i = \frac{jQ_L\Gamma_s 2\frac{\omega-\omega_L}{\omega_0} + \Gamma_s + de^{-j2\delta}}{jQ_L 2\frac{\omega-\omega_L}{\omega_0} + 1} \tag{5.43}$$

To further simplify the last equation we define the variable t as the normalized frequency as follows:

$$t = 2\frac{\omega - \omega_L}{\omega_o} \tag{5.44}$$

Then Γ_i becomes:

$$\Gamma_i = \frac{a_1 t + a_2}{a_3 t + 1} \tag{5.45}$$

Where the coefficients are:

$$a_1 = jQ_L\Gamma_s \qquad (5.46) \qquad a_2 = \Gamma_s + de^{-j2d} \qquad (5.47) \qquad a_3 = jQ_L \qquad (5.48)$$

The later is exactly the same equation defined as in 5.25 where z has been replaced by t and w by Γ_i.

Measurements in the lab will provide us with N measurements pairs of frequency ω, and reflection coefficient Γ_i, so it will be possible to set an over-determined system of equation with 3 unknowns that can be solved as in 5.42.

This system will be solved with a software designed for that purpose. A particular attention must be paid to the values ω_o and ω_L. The solution has strong dependence on these variables. Both are unknown, and they intervene in the definition of the variable t (see equation 5.44). An iterative procedure is carried out by the solving algorithm which makes successive corrections to the value of ω_L. In simple terms, once the circle equation is obtained using

measurement pairs (ω_n,Γ_n), a new interpolated Γ_L can be calculated. Later a new value of ω_L is derived from the interpolated Γ_L.

In the first iteration, the values ω_L and ω_o are set as equal to the measured ω for which Γ is closest to center of the Smith chart. In Fig. 5.5, squares indicate 8 measurement points. Γ_L used for the first iteration is denoted as Γ_{L1}. The center of the Q circle (Γ_c) and the detuned reflection coefficient (Γ_s) are also indicated in the same figure. Coefficient can be now calculated using equation 5.42. Once the fitting procedure is completed and coefficients a_n are obtained a new value of Γ_L (Γ_{L2}) can be computed using the equation 5.24, which is a function of the center of the circle Γ_c and detuned reflection coefficient Γ_s. Substituting Γ_{L1} to the equation 5.45 a new value of t can be computed. Using the later value of t, a new value of ω_L can be computed using equation 5.44.

It can be noticed in Fig. 5.6 that successive iterations does not change the position or the size of the Q circle. The circle always passes through all measurement points used to compute equation 5.45. However, the iterations improves the accuracy of ω_L and Q factors. Using measured data with the probe developed in Chapter 3, it was found that variation of the loaded resonant frequency ω_L is in the order of 0.01% between the second and the third iteration. The results presented in the next section were obtained with this procedure limited to 3 iterations.

5.1.3 Simulation results

This section demonstrates the application of the curve fitting algorithm introduced in the previous sections using simulated measurement over an LSP mesh. The simulation procedure has been divided in three stages. First of all, in order to simplify the understanding of the algorithm, ADS simulations are presented based on the lumped-element circuit model presented before (See Fig. 5.1). The loop probe at the end of the resonator is represented by an inductor whose value change from 2.5 nH to 3 nH. The later inductance values resulted from *Feko*®simulations discussed in the next paragraphs.

Results of *ADS*®simulation are plotted in Fig. 5.7. The magnitude of $|\Gamma_{in}|$ and the Smith chart representation shows the curves for three values of the inductance L namely 2.5 nH, 2.75 nH and 3 nH. It can be seen that the resonance frequency varies in a range of 500 kHz. On the other hand, a frequency span of 5 MHz was required to draw the Q circle. Although not perceptible in Fig. 5.7b, a small clockwise rotation Q circles occur in the Smith chart for increasing values of L, whereas the Γ_{in} plot shows a decrease of the resonant frequency with increasing values of L.

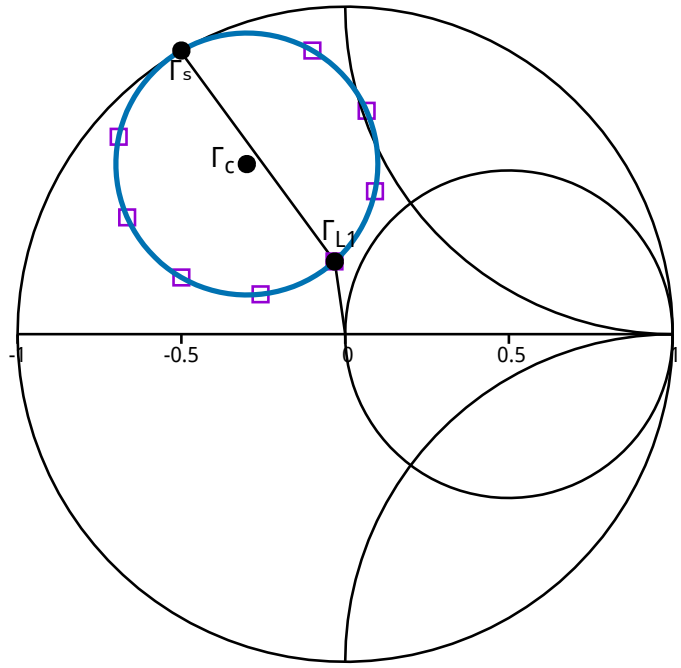

Figure 5.5 Values of Γ_{L1},Γ_c, Γ_s for the 1st iteration.

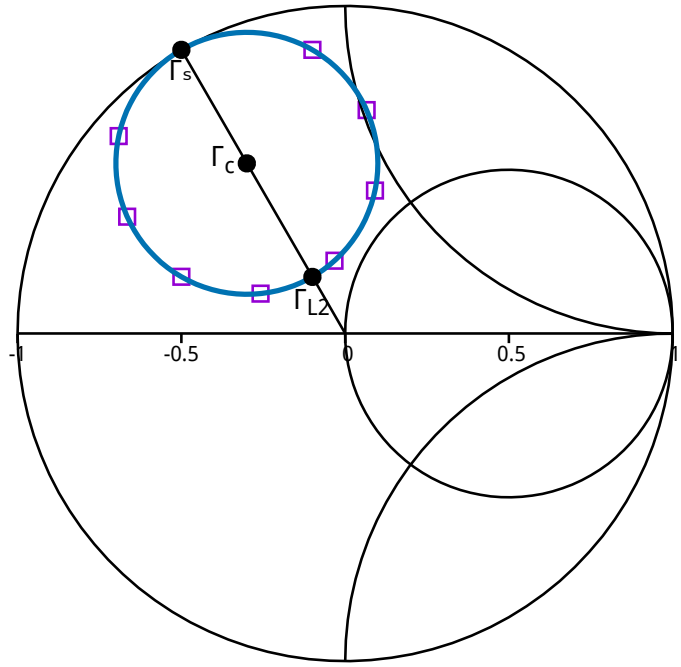

Figure 5.6 Values of Γ_{L1},Γ_c, Γ_s for the 2nd iteration.

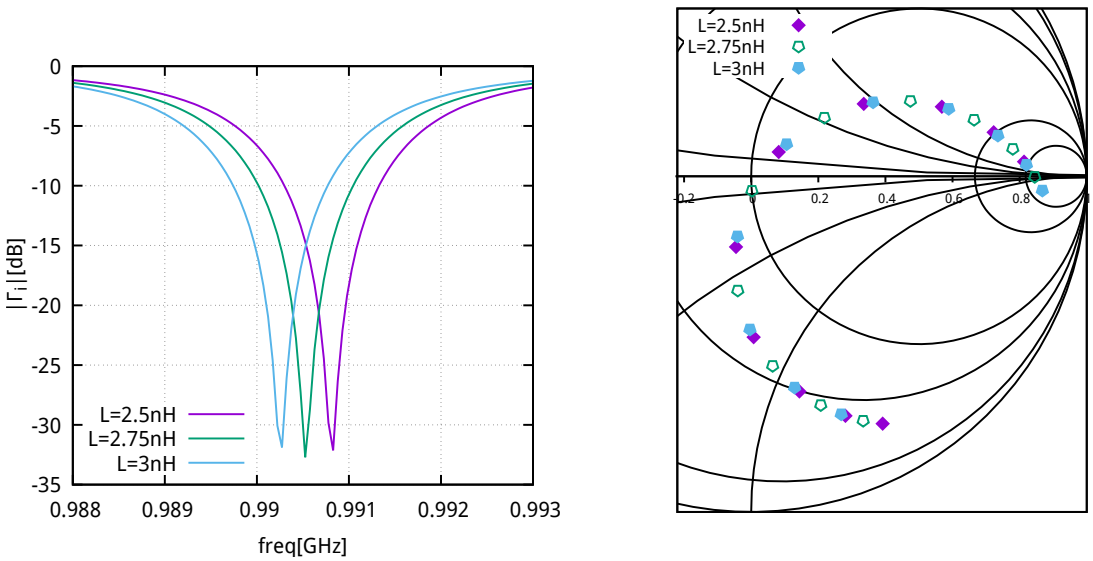

(a) (b)

Figure 5.7 Γ_i for L=2.5, 2.75 and 3 nH. (a) Γ_i magnitude. (b) Γ_i Smith chart.

The next stage to design a simulation as close as possible to reality consists in replacing the inductance by the impedance of the loop probe over an LSP mesh obtained from a full wave simulation. The probe model is the same as in Chapter 3 and it is replicated in Fig. 5.8. The probe sweeps over the wire mesh in discrete steps over the x coordinate. The MoM simulation using *Feko*®covered a frequency range centered at 0.9905 GHz with a 5 MHz span and 21 simulated frequency points for each position. In addition, a script was programmed to save the associated *.snp* parameter file every time the probe moves to a new position.

In the first simulated position, the probe starts at $x = 0$ (see Fig. 5.8). It then moves towards the positive x-coordinates in steps of $0.8mm$ which is equivalent to one quarter of the longest diagonal of a diamond ($LWD/4$). Hence, at the third simulated position, the probe is at $x = LWD/2$ and it overlaps the opposite mesh diamond. Due to symetry, the 4th and 5th simulated positions are relatively equivalent to the 2nd and 1st positions respectively. Fig. 5.9 shows the probe in the 1st, 2nd and 3rd positions. Subsequently, an *ADS*®simulations of the system shown in Fig. 5.1 was performed with the inductance replaced with the simulated probe impedances. (see Fig. 5.10). A series of pre-recorded *snp* files are used to connect to *ADS*®through the available database access component.

It can be noticed in this figure that the curves corresponding to the 1st and 5th positions overlap. This is because these two positions are one full mesh period apart. Likewise the curves for the 2nd and 4th positions also overlap, but this time it is due to the symmetrical

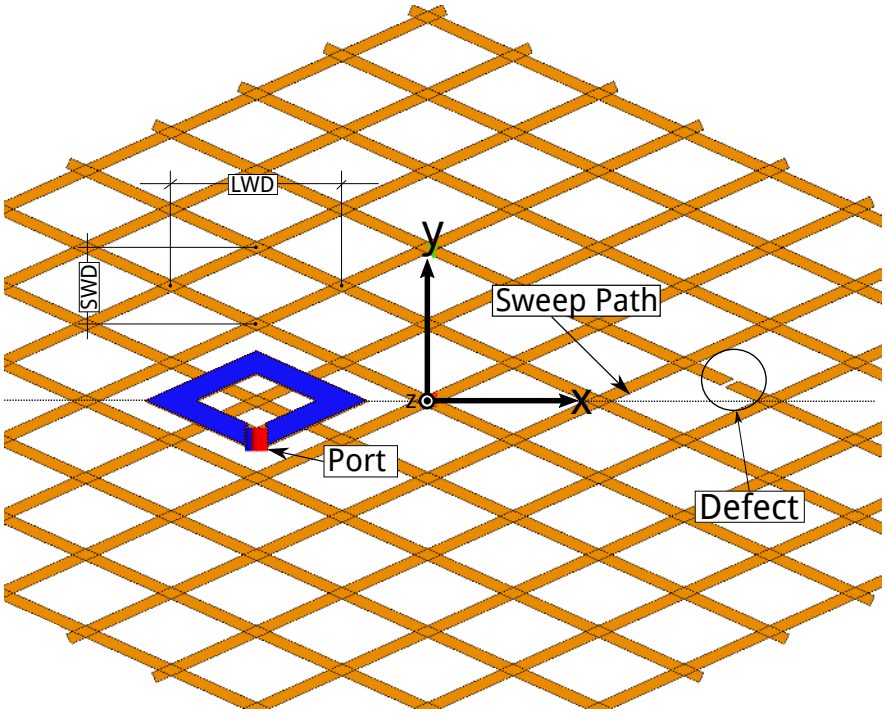

Figure 5.8 Wire mesh and probe simulation model. Probe at $x = -3.175mm$ $(-1LWD)$

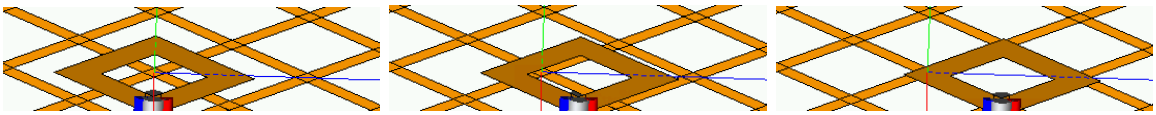

(a) (b) (c)

Figure 5.9 Simulated probe in the 1st (a), 2nd (b) and 3rd (c) positions.

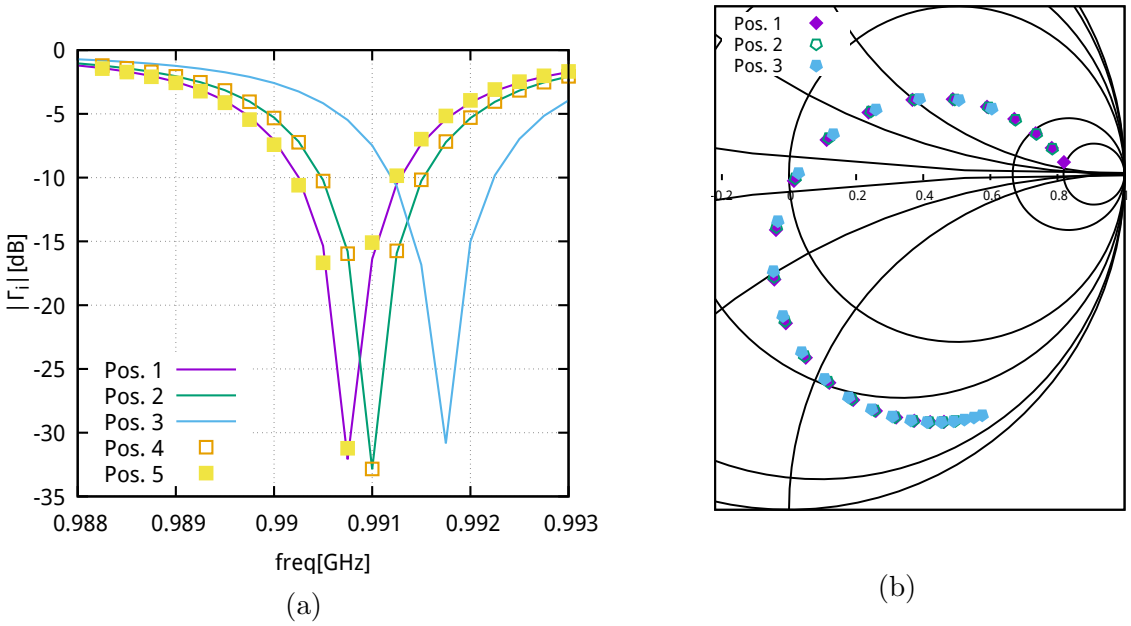

Figure 5.10 Γ_i for 5 positions. (a) Γ_i magnitude for positions 1 to 5. (b) Γ_i Smith chart for positions 1,2 and 3.

positions of the probes with respect to the mesh. Moreover, on the 3rd position, where the probe diamond and the corresponding wire mesh diamond overlap, constitutes the condition of the lowest probe inductance. As a consequence, the resonant frequency is the highest when the probe occupies this position. The corresponding response plotted in the Smith chart behaves, as expected, exactly as for the lumped inductor case. It rotates counterclockwise as probe shifts from 1st to the 3rd. position. The effect is hardly noticeable in Fig. 5.10b but it can be observed with a magnified view.

For third stage of the simulation, the curve fitting iterative procedure developed the previous section is used with the simulation data obtained in the previous stage. The procedure should allow us to find the changes in the resonant frequency and quality factor as the probe moves over the LSP sample.

The interative curve fitting algorithm is applied to 5 positions using 21 frequency points. A curve indicating the obtained resonant frequency for each position is displayed in Fig. 5.11. The violet curve represents the frequencies for which Γ_i is the closest to the center of the Smith chart, out of 21 simulated frequency points. The green curve shows the corrected resonance frequencies by the curve fitting procedure. Even when the differences appear to be small, the corrections made by the algorithm can be clearly observed.

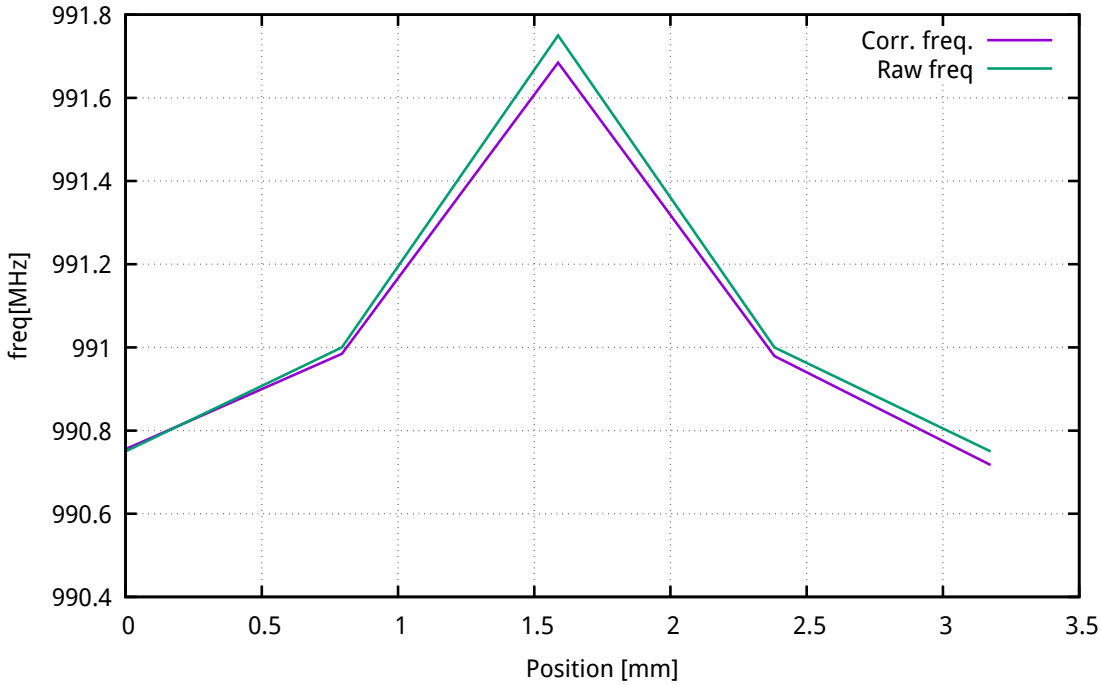

Figure 5.11 Resonance frequencies estimated with 21 frequency points. Probe at $x = 0$, $\frac{1}{4}LWD$, $\frac{1}{2}LWD$, $\frac{3}{4}LWD$, LWD.

In the next case, only 5 frequency points equally spaced are calculated instead of the previous 21, but the same span of 5 MHz is covered.. A Smith chart plot with raw data for position 1,2 and 3 is shown in Fig. 5.12. The rectangular plot in Fig. 5.13 shows two curves: raw data with 5 frequency point is shown in green and interpolated data using only 5 frequencies in violet. The interpolated data, obtained by applying the iterative algorithm, provides the same results at if it was calculated with 21 points. Furthermore, resonance frequency points are undetected for the 2nd and 4th positions using 5 frequency points raw data (green line). Applying the algorithm, those resonant frequencies are accurately calculated. As a conclusion it can be appreciated that the curve fittings technique calculates the resonant frequency efficiently even with a low number of frequency points.

As a final simulation for this chapter, the last model consists on the probe sweeping over the LSP from position 1 to the far end of the mesh, shown in Fig 5.8 in which a broken strand is introduced near $x = 4.8mm$. The swept path goes one LWD after the end of the mesh. Only 5 frequency points were calculated for each position. The results are plotted in Fig. 5.14. The algorithm can precisely detect the defect located at $x = 4.8mm$ as well as the diamonds with no defects. The raw data (green curve) completely missed the defect. It can be concluded

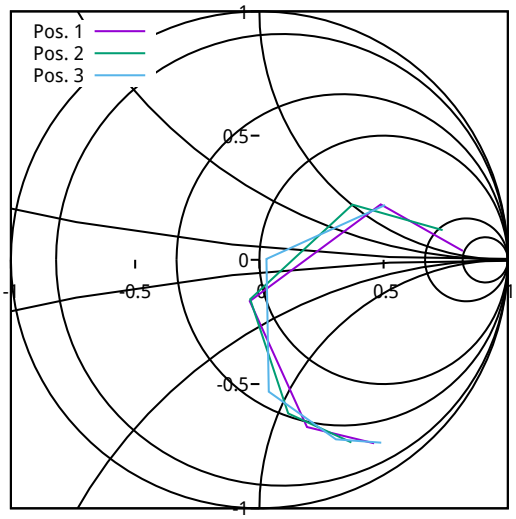

Figure 5.12 ADS Γ_i simulation with 5 frequency points. Probe at positions 1, 2 and 3.

that without aplying the interpolation procedure it would not have been possible to detect the defect in the LSP. Besides, notice the behavior of the resonant frequency at the end of the mesh. The reported decrease in resonance frequency (990.6 MHz) can be explained through the increase of inductance due to the absence of LSP mesh.

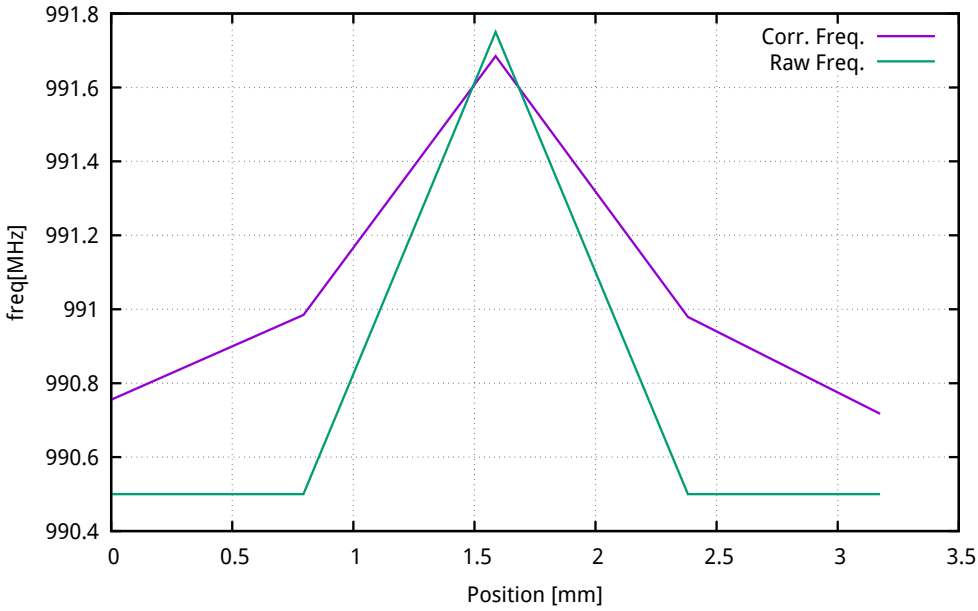

Figure 5.13 Resonance frequencies estimated with 5 frequency points. Probe at positions 1, 2 and 3.

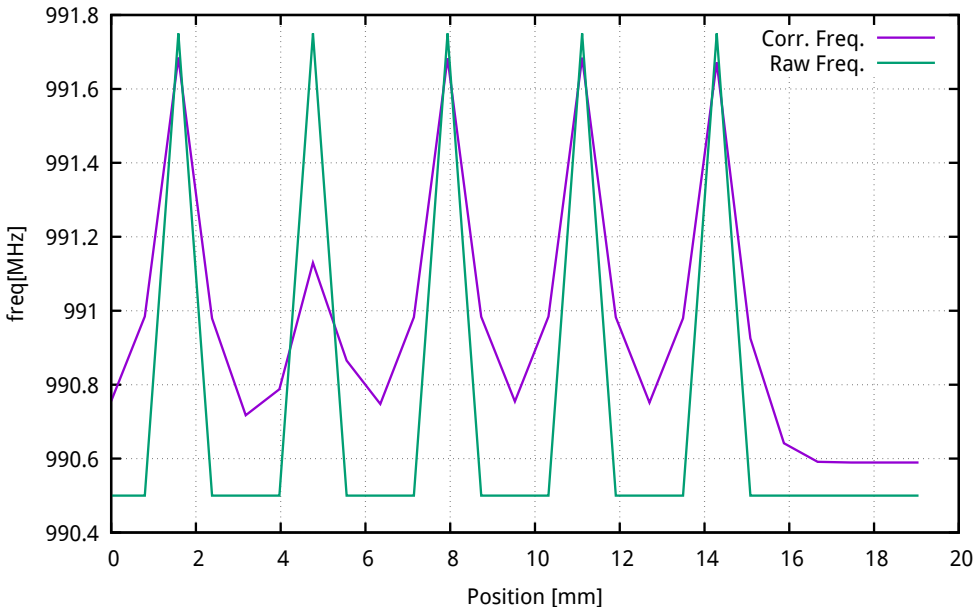

Figure 5.14 ADS Γ_i simulation with 5 frequency points over $6LWD$

5.1.4 Experimental results

In this section we present a demonstration of the curve fitting algorithm previously introduced using experimental data. Almost all measurements presented in this thesis have been performed in a narrow frequency band; typically 500 kHz. As shown at the beginning of this chapter, this bandwidth does not contain enough useful data suitable for the application of the proposed algorithm. Due to Covid-19 it was not possible to carry-out new measurements in the laboratory. The only data available that can potentially be used to prove the effectiveness of the algorithm is the one presented in Fig. 2.8. Figure 5.15 shows Γ_i measurements using a micro-coaxial probe over two different materials namely copper and FR4 dielectric; and also empty space. The probe-sample distance is always the same for the first two cases. The data consist of 401 frequency points taken over 10 MHz span centered around 1.05 GHz. It can be observed that the three Q-circles overlap almost perfectly. Also, the circles are detached from the external contour of the Smith chart. Thus, as explained in the first section of Chapter 3, the coupling mechanism involves losses. These losses are not taken into account by the curve fitting algorithm. Losses should be considered while looking for precise values of unloaded quality Q_0 factor but they have very little impact in the determination of the loaded resonant frequency.

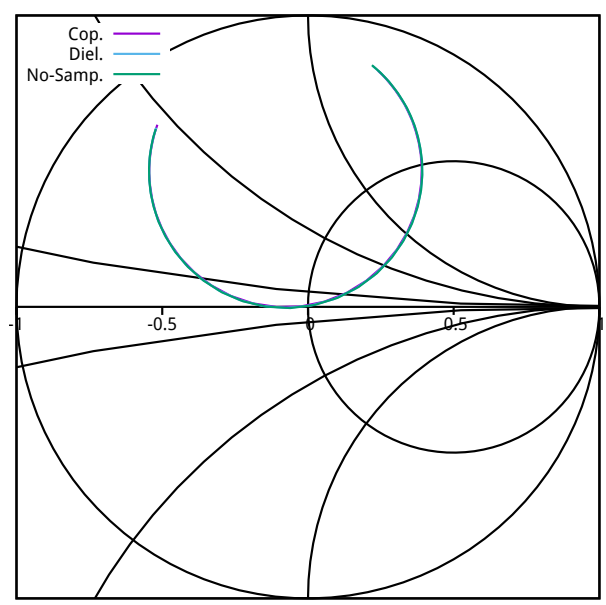

Figure 5.15 Γ_i Micro-coax probe measurements. 401 frequency points.

With a focus on demonstrating the performance of the algorithm, two rather extreme cases will be presented. First, the algorithm is applied to each of the three measurements consider-

ing 401 frequency points. Loaded resonance frequencies and unloaded quality factors will be calculated for each of the three samples. In a second instance, only 5 frequency points will be considered by the algorithm to execute the same calculations, namely resonance frequencies and unloaded quality factor Q_0. A Smith chart representation of Γ_i using only 5 equally spaced frequency points, sampled from the set of 401 points, is shown in Fig. 5.16.

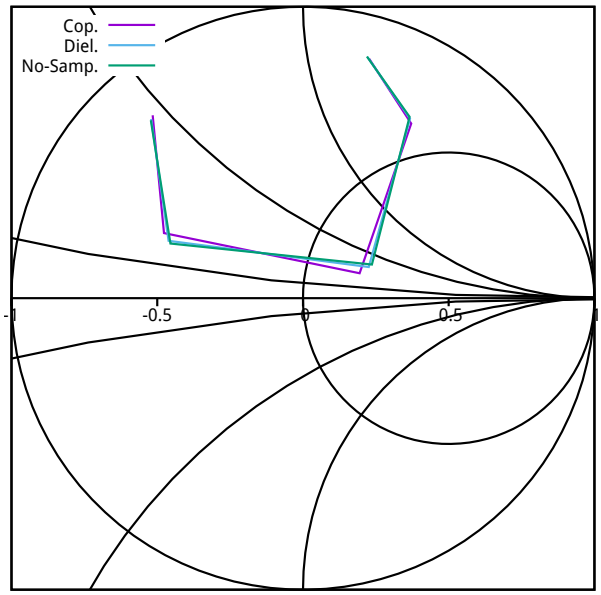

Figure 5.16 Γ_i Micro-coax probe measurements. 5 frequency points.

Applying the algorithm presented before to this data, it is possible to extract the loaded resonance frequency for the three samples. Results are shown in table 5.1. This table compares the results of the applied algorithm with 401 frequency measurement points (raw data) and 5 measurements points (interpolated data) for the three evaluated samples. To highlight the differences between the two calculations relative differences between the two are also shown. As it can be appreciated, the differences are in the order of 26 kHz in the worst case, which represents a negligible quantity for our purposes. The relative error is small for the three cases, indicating that using interpolated data does not degrade the contrast between the responses of different materials. Recalling that the wire mesh defect detection lies in the disruption of frequency patterns from a calibration case, the error in which the calculations incurs due to fewer data points would not weaken the over-all detection sensibility of the system.

The gain in terms of measurement time is presented in table 5.2. Here we compare the measurement time per probe and per position due to PNA acquisition (frequency sweep), mechanical displacement and RF switch. The times for electric and magnetic probes referred

Material	Copper	FR4	No-sample
Raw Data	1048.400	1048.525	1048.575
Interpolated Data	1048.398	1048.510	1048.549
Difference (%)	0.0002	0.0014	0.0025

Table 5.1 Resonant frequencies - Raw data and Interpolated data

to the CPW and shielded loop probes respectively. Concerning the probe array the mechanical displacement time is divided by the number of elements in the array; 6 in the previously presented experiment. The times calculated for the interpolation algorithm considered that the overall PNA acquisition has a linear behavior with the number of frequency points measured which can not be strictly the case due to some other variables that intervene in a measurement. The total per square centimeter considered a matrix of 4×4 measurement points in a rectangular surface equivalent to the footprint of a mesh diamond, which for the sample employed in measurements is 3.1×1.4mm.

Probe type	Acquisition PNA [sec]	Mechanical Displacement [sec]	RF switch [sec]	Total [sec]	Total per cm^2 [min]
Electric probe	1.8	1	0	2.8	16.1
Magnetic probe	0.9	1	0	1.9	10.92
Probe array	0.9	1/6	0.3	1.36	7.85
Probe array + freq. interp.	0.9/80	1/6	0.3	0.47	2.74

Table 5.2 Measurement time per probe per position (sec) and per square centimeter (min).

5.2 Conclusion

In this chapter a new application of an existent technique is presented to improve measurement time. It provides drastic reductions in measurement time for each probe individually. Previously, tight constraints in term of network analyzer measurement points, bandwidth, and IF filter were necessary to be able to discriminate relative small frequency displacements compared to the resonator natural resonance frequeny. This technique permits to relax those constraints and thus speed-up measurements. Summarizing, using the presented technique, the PNA requirements in terms of frequency range, dynamic range, test time and frequency precision are notably low for today standards. Highly portable and low cost VNAs could potentially be used in portable device for field testing. Narrow band trials have been carried out with a R54 planar Copper Mountain Technologies VNA. This a 1 port, USB, display-less network analyzer. Due to its lack of speed it was not suitable for narrow band measurements.

However, we believe that due to its size, price, and performance it could be easily embedded in a portable device.

Theoretically, the experimental set-up that was used for all measurements in the lab can be replaced by an equivalent network were the coupling mechanism is represented by a lossless two-port structure. This network behaves as a fractional linear transformation. A generic curve fitting algorithm is given as a mean to fit a circle with the information provided by few measurement pairs (ω,Γ_i). Changes in the resonance frequency can be tracked through and iterative procedure that use Q circle parameters extracted from measured data.

In an attempt to prove the previous concepts, combined simulations in ADS and FEKO are given. They demonstrate the algorithm ability to track the resonance frequency changes while the probe sweeps over the mesh. By using a few frequency points (5 points) LSP cells as well as defects are clearly detected, hence validating the hypothesis of measurement time reduction per probe position without any information loss.

To further validate the results, the algorithm was applied to measurements taken over three different samples using 5 frequency points. Again, the procedure is able to find the corresponding resonance frequency effectively with a a maximum error of 0.025%.

CHAPTER 6 CONCLUSION

6.1 Conclusions

This thesis focuses on finding a new technique capable of detecting defects on LSP mesh used in composite aircraft. Based on a microwave microscopy approach, novel electric and magnetic probes have been developed. These new probes have been proven to be very effective in finding small defects in the wire mesh. With the proposed tool, aircraft manufacturers are capable of measuring the quality of LSP mesh installed in a composite panel. No method or technique was available at the present time to quantify damage in LSP with the level of details required by the industry. The present technique allows to asses damage in composite panel struck by lightning too. Moreover, a potential for measurement the paint thickness with high accuracy was also demonstrated.

A proof of how near filed microwave microscopy can be applied to CFRP defect mesh detection is given in Chapter 2. A new flexible probe that sweeps over a composite panel is introduced. A salient feature of this probe is that it maintains contact with sample as it is scanned. An original simple stand-off distance control mechanism is revealed making use of a flexible substrate. Chapter 3 introduce a novel shielded planar magnetic probe. Flaws in the order of micrometers are found in the wire mesh under the paint layer using this probe.

Usually large surfaces needs to be analyzed in the aircraft domain. A method for applying this novel technique to large surfaces is introduced in Chapter 4. An array of shielded probes linked together by an RF switch is provided. A mechanism of compensating asymmetries introduced by the switch is described. Measurement in CFRP samples show that the proposed array achieves the same resolution as an isolated probe. In order to accelerate measurements, an iterative procedure has been outlined in Chapter 5. Theoretical an experimental result show that a few measurement frequencies are needed to reach the same precision as a measure with 400 frequencies.

Many limitations concerning the measurement set-up still needs to be overcome. All the measurements have been carried out with laboratory grade equipment, namely probe station and PNA-X. Further work needs to be done to improve the portability and to lower the measurement instrument requirements to reach the precision needed by this technique.

6.2 Future work

6.2.1 Instrument specifications

The final outcome of this thesis is an instrument capable of defect detection in LSP mesh. As a detection instrument, quantitative indicators, such as resolution, dynamic range, sensitivity should be given. This thesis presents a demonstration of a measurement principle and a detailed study to determine the limitations has not been done. Nevertheless, it can be seen that the detection of the properties of interest (broken strand, paint thickness) for a mesh used in practical aerospace applications is possible, which was the original objective. A lot more work is required to determine the limitations of microwave microscopy in terms of the previously mentioned parameters. For the most part, the indicators mentioned previously are closely tied to the PNA-X that was employed in the measurements. The use of a narrow-band 6 port reflectometer must be considered. It could be a good option in terms of portability and cost reduction.

6.2.2 Reduction of resonator size

The goal of this thesis was to demonstrate that a principle used in microwave microscopy was useful as a building block for a new application in the aircraft domain. The ultimate goal was to engineer a portable device. In order to fulfill this purpose, it is of primary importance to reduce the size of the resonator, which is now a 3.2 m semi-rigid coaxial cable. Some alternatives are given that complies with the quality factor as well as overall size of a potentially portable device. During the experiments, the unloaded quality factor was calculated in the order of 800.

In [59] an extremely small non-contact near-field microwave circuit was proposed for planar structures. Instead of the long coaxial cable resonator used in this thesis, they employed an integrated $\lambda/2$ open circuit coaxial resonator which is filled with high dielectric constant ($\epsilon_r = 90$). Its size is $6 \times 6 \times 8.5$ mm and its loaded Q of 650 at 4.39 GHz. This quality factor is in the same order of magnitude of the one used in the design presented in this thesis. Besides, the paper shows graphs with frequency shifts of 25 kHz span, whereas a 500 kHz span was required in our work. Another feature of this resonator in that it can easily be integrated in a microstrip circuit, which could potentially be the same PCB circuit of the probes.

In [60] a low-cost planar active resonator based on substrate integrated waveguide techniqueis reported. The resonator is composed by an active negative resistance converter which compensates the energy loss within the SIW cavity. The author reported a loaded Q factor of 1455 at 11.5 GHz. Higher levels of Q implies better frequency selectivity which in our appli-

cation means more spatial resolution. Because of its compact size (the substrate thickness is 0.508 mm) and its high frequency selectivity it can be a good candidate to replace the actual resonator.

In [61] a compact self-oscillator suitable for high resolution imaging is presented. The circuit is composed by a 14 cm long folded resonator working at 2.25 GHz, and RF amplifier and the tip. The salient feature of the circuit is that it does not require a signal source; only a spectrum analyzer is needed to track frequency drifts. The author states that due to the amplifier non-linearity the circuit sensitivity and spatial resolution are improved compared to traditional design, so the benefits of this approach would also be an increase of spatial resolution.

The last venue that could be explored in order to reduce the size of the resonator is related to surface acoustic wave resonators (SAW). SAW devices operate in a frequency range from 20 MHz to 2 GHz. They are small, low loss, and inexpensive. Unloaded Q factors vary from 50 000 at the low end to 3000 at the higher frequencies. As an example, *Muratta*® manufactures a SAW resonator packaged in a 3×3 mm surface-mount ceramic case. It features and unloaded Q factor of 6400. Thee equivalent circuit of this resonator is a shunt LCR circuit where the value of L is in the order 15 µH. The challenge resides that the equivalent inductance of the probe proposed in this thesis is in the order of 5 nH, making the frequency perturbations introduced in the resonator by the probe negligible.

6.2.3 X-rays validation

It has been said at the introduction of this thesis that the only capable technique to find small defects in the LSP wire mesh in X-ray tomography. High resolution X-rays images of the three sample presented in Chapter 4 could be compared with the images generated by the proposed near field technique afterwards. Conclusions could be drawn from this comparison exercise in term of undetected flaws and resolution of the proposed technique. This validation could not take place because of Covid19.

REFERENCES

[1] Jennifer Segui, "Protecting aircraft composites from lightning strike damage," 2015, [Online; accessed August 1, 2020]. [Online]. Available: https://www.comsol.com/blogs/protecting-aircraft-composites-from-lightning-strike-damage/

[2] J. G. G. Sweers, B. Birch, "Lightning strikes: Protection, inspection, and repair," 2012, [Online; accessed August 1, 2020]. [Online]. Available: https://www.boeing.com/commercial/aeromagazine/articles/2012_q4/4/

[3] V. Venugopal, "What does it feel like when your plane gets hit by lightning?" 2019, [Online; accessed August 1, 2020]. [Online]. Available: https://www.quora.com/What-does-it-feel-like-when-your-plane-gets-hit-by-lightning

[4] Aerossurance, "When screens go blank: Ntsb on a 787 display loss after a lightning strike," 2018, [Online; accessed August 1, 2020]. [Online]. Available: http://aerossurance.com/safety-management/ntsb-787-lightning-strike/

[5] "JSW6-33DR+ switch on test board," Mini-circuits Inc, 2018, TB-724+,Rev. A.

[6] G. Gardner, "Lightning strike protection for composite structures," *High performance composites*, vol. 14, no. 4, p. 44, 2006.

[7] H. Mulazimoglu, "Recent developments in techniques to minimize lightning current arcing between fasteners and composite structure," in *International Conference on Lightning and Static Electricity*, Sep. 2011.

[8] M. Gagné and D. Therriault, "Lightning strike protection of composites," *Progress in Aerospace Sciences*, vol. 64, p. 1–16, Jan 2014. [Online]. Available: http://dx.doi.org/10.1016/j.paerosci.2013.07.002

[9] S. Black, "Lightning strike protection strategies for composite aircraft," *High-Performance Composites*, no. 5-1, 2013.

[10] B. Zhang, V. R. Patlolla, D. Chiao, D. K. Kalla, H. Misak, and R. Asmatulu, "Galvanic corrosion of al/cu meshes with carbon fibers and graphene and ito-based nanocomposite coatings as alternative approaches for lightning strikes," *The International Journal of Advanced Manufacturing Technology*, vol. 67, no. 5-8, p. 1317–1323, Oct 2012. [Online]. Available: http://dx.doi.org/10.1007/s00170-012-4568-3

[11] F. Moupfouma, "Aircraft structure paint thickness and lightning swept stroke damages," *SAE International Journal of Aerospace*, vol. 6, no. 2, p. 392–398, Sep 2013. [Online]. Available: http://dx.doi.org/10.4271/2013-01-2135

[12] L. Chemartin, P. Lalande, B. Peyrou, A. Chazottes, P. Elias, C. Delalondre, B. Cheron, and F. Lago, "Direct effects of lightning on aircraft structure: analysis of the thermal, electrical and mechanical constraints," *AerospaceLab*, no. 5, pp. 1–15, 2012.

[13] J. H Heida and D. J Platenkamp, "Evaluation of non-destructive inspection methods for composite aerospace structures," *International Worksho of NDT Experts*, vol. 2011, Oct 2011.

[14] A. Ng and J. Swanevelder, "Resolution in ultrasound imaging," *Continuing Education in Anaesthesia Critical Care & Pain*, vol. 11, no. 5, p. 186–192, Oct 2011. [Online]. Available: http://dx.doi.org/10.1093/bjaceaccp/mkr030

[15] T. Zweschper, A. Dillenz, and G. Busse, "Ultrasound lockin thermography – a ndt method for the inspection of aerospace structures," *Proceedings of the 2000 International Conference on Quantitative InfraRed Thermography*, 2000. [Online]. Available: http://dx.doi.org/10.21611/qirt.2000.046

[16] F. Taillade, M. Quiertant, K. Benzarti, and C. Aubagnac, "Non-destructive evaluation (nde) of composites: using shearography to detect bond defects," *Non-Destructive Evaluation (NDE) of Polymer Matrix Composites*, p. 542–557e, 2013. [Online]. Available: http://dx.doi.org/10.1533/9780857093554.4.542

[17] J. García-Martín, J. Gómez-Gil, and E. Vázquez-Sánchez, "Non-destructive techniques based on eddy current testing," *Sensors*, vol. 11, no. 12, pp. 2525–2565, Feb. 2011. [Online]. Available: https://doi.org/10.3390%2Fs110302525

[18] A. Savin, D. Faktorova, and R. Grimberg, "High frequency eddy current testing," in *International Workshop of NDT Experts*, Prague, 2011, pp. 71–78.

[19] J. R. Gallion and R. Zoughi, "Millimeter-wave imaging of surface-breaking cracks in steel with severe surface corrosion," *IEEE Transactions on Instrumentation and Measurement*, vol. 66, no. 10, pp. 2789—2791, Oct. 2017. [Online]. Available: http://dx.doi.org/10.1109/tim.2017.2735658

[20] S. Kharkovsky, M. Ghasr, and R. Zoughi, "Near-field millimeter-wave imaging of exposed and covered fatigue cracks," *IEEE Transactions on Instrumentation*

and Measurement, vol. 58, no. 7, pp. 2367—2370, Jul. 2009. [Online]. Available: http://dx.doi.org/10.1109/tim.2009.2022380

[21] M. A. Abou-Khousa, K. T. Muhammed Shafi, and X. Xingyu, "High-resolution uhf near-field imaging probe," *IEEE Transactions on Instrumentation and Measurement*, vol. 67, no. 10, pp. 2353—2362, Oct. 2018. [Online]. Available: http://dx.doi.org/10.1109/tim.2018.2815437

[22] A. Albishi and O. Ramahi, "Detection of surface and subsurface cracks in metallic and non-metallic materials using a complementary split-ring resonator," *Sensors*, vol. 14, no. 10, pp. 19 354—19 370, Oct. 2014. [Online]. Available: http://dx.doi.org/10.3390/s141019354

[23] A. M. Albishi and O. M. Ramahi, "Microwaves-based high sensitivity sensors for crack detection in metallic materials," *IEEE Transactions on Microwave Theory and Techniques*, vol. 65, no. 5, pp. 1864—-1872, May. 2017. [Online]. Available: http://dx.doi.org/10.1109/tmtt.2017.2673823

[24] J. Kastner, B. Plank, A. Reh, D. Salaberger, and C. Heinzl, "Advanced x-ray tomographic methods for quantitative characterization of carbon fibre reinforced polymers," *Proc. of 4th International Symposium on NDT in Aerospace*, pp. 1–9, 11 2012.

[25] I. Jandejsek, J. Jakubek, M. Jakubek, P. Prucha, F. Krejci, P. Soukup, D. Turecek, D. Vavrik, and J. Zemlicka, "X-ray inspection of composite materials for aircraft structures using detectors of medipix type," *Journal of Instrumentation*, vol. 9, no. 05, pp. C05 062–C05 062, 2014. [Online]. Available: https://doi.org/10.1088/1748-0221/9/05/c05062

[26] S. Garcea, Y. Wang, and P. Withers, "X-ray computed tomography of polymer composites," *Composites Science and Technology*, vol. 156, p. 305–319, Mar 2018. [Online]. Available: http://dx.doi.org/10.1016/j.compscitech.2017.10.023

[27] E. Synge, "A suggested method for extending microscopic resolution into the ultra-microscopic region," *The London, Edinburgh, and Dublin Philosophical Magazine and Journal of Science*, vol. 6, no. 35, pp. 356–362, 1928. [Online]. Available: https://doi.org/10.1080/14786440808564615

[28] Z. Frait, "The use of high-frequency modulation in studying ferromagnetic resonance," *Czechoslovak Journal of Physics*, vol. 9, no. 3, p. 403–404, May 1959. [Online]. Available: http://dx.doi.org/10.1007/bf01557202

[29] R. F. Soohoo, "A microwave magnetic microscope," *Journal of Applied Physics*, vol. 33, no. 3, pp. 1276–1277, 1962. [Online]. Available: https://doi.org/10.1063/1.1728690

[30] A. Husain and E. Ash, "Microwave scanning microscopy for non-destructive testing," *1975 5th European Microwave Conference*, Sep 1975. [Online]. Available: http://dx.doi.org/10.1109/euma.1975.332181

[31] M. Tabib-Azar, N. S. Shoemaker, and S. Harris, "Non-destructive characterization of materials by evanescent microwaves," *Measurement Science and Technology*, vol. 4, no. 5, p. 583–590, May 1993. [Online]. Available: http://dx.doi.org/10.1088/0957-0233/4/5/007

[32] M. Tabib-Azar, D.-P. Su, A. Pohar, S. R. LeClair, and G. Ponchak, "0.4 μm spatial resolution with 1 ghz ($\lambda = 30cm$) evanescent microwave probe," *Review of Scientific Instruments*, vol. 70, no. 3, pp. 1725–1729, 1999. [Online]. Available: https://doi.org/10.1063/1.1149658

[33] D. E. Steinhauer, C. P. Vlahacos, S. K. Dutta, F. C. Wellstood, and S. M. Anlage, "Surface resistance imaging with a scanning near-field microwave microscope," *Applied Physics Letters*, vol. 71, no. 12, pp. 1736–1738, 1997. [Online]. Available: https://doi.org/10.1063/1.120020

[34] D. E. Steinhauer, C. P. Vlahacos, S. K. Dutta, B. J. Feenstra, F. C. Wellstood, and S. M. Anlage, "Quantitative imaging of sheet resistance with a scanning near-field microwave microscope," *Applied Physics Letters*, vol. 72, no. 7, p. 861–863, Feb 1998. [Online]. Available: http://dx.doi.org/10.1063/1.120918

[35] C. P. Vlahacos, D. E. Steinhauer, S. K. Dutta, B. J. Feenstra, S. M. Anlage, and F. C. Wellstood, "Quantitative topographic imaging using a near-field scanning microwave microscope," *Applied Physics Letters*, vol. 72, no. 14, p. 1778–1780, Apr 1998. [Online]. Available: http://dx.doi.org/10.1063/1.121182

[36] S.-C. Lee, C. P. Vlahacos, B. J. Feenstra, A. Schwartz, D. E. Steinhauer, F. C. Wellstood, and S. M. Anlage, "Magnetic permeability imaging of metals with a scanning near-field microwave microscope," *Applied Physics Letters*, vol. 77, no. 26, p. 4404–4406, Dec 2000. [Online]. Available: http://dx.doi.org/10.1063/1.1332978

[37] C. Gao and X.-D. Xiang, "Quantitative microwave near-field microscopy of dielectric properties," *Review of Scientific Instruments*, vol. 69, no. 11, pp. 3846–3851, 1998. [Online]. Available: https://doi.org/10.1063/1.1149189

[38] C. P. Vlahacos, R. C. Black, S. M. Anlage, A. Amar, and F. C. Wellstood, "Near-field scanning microwave microscope with 100 μm resolution," *Applied Physics Letters*, vol. 69, no. 21, pp. 3272–3274, 1996. [Online]. Available: https://doi.org/10.1063/1.118033

[39] D. Kajfez and E. Hwan, "Q-factor measurement with network analyzer," *IEEE Transactions on Microwave Theory and Techniques*, vol. 32, no. 7, pp. 666–670, 1984. [Online]. Available: https://doi.org/10.1109/tmtt.1984.1132751

[40] F. Duewer, C. Gao, I. Takeuchi, and X.-D. Xiang, "Tip-sample distance feedback control in a scanning evanescent microwave microscope," *Applied Physics Letters*, vol. 74, no. 18, pp. 2696—2698, May 1999. [Online]. Available: http://dx.doi.org/10.1063/1.123940

[41] E. Ponchak, D. Akinwande, R. Ciocan, S. LeClair, and M. Tabib-Azar, "Evanescent microwave probes using coplanar waveguide and stripline for super-resolution imaging of materials x," *1999 IEEE MTT-S International Microwave Symposium Digest (Cat. No.99CH36282)*, 1999. [Online]. Available: http://dx.doi.org/10.1109/mwsym.1999.780335

[42] R. N. Simons, *Conventional Coplanar Waveguide.* John Wiley & Sons, Ltd, 2002, ch. 2, pp. 11–86. [Online]. Available: https://onlinelibrary.wiley.com/doi/abs/10.1002/0471224758.ch2

[43] M. Anlage, V. Talanov, and A. Schwartz, *Principles of Near-Field Microwave Microscopy.* New York, NY: Springer New York, 2007, pp. 215–253. [Online]. Available: https://doi.org/10.1007/978-0-387-28668-6_8

[44] L. Rufail, J. J. Laurin, and F. Moupfouma, "On the use of microwave microscopy for detecting defects in the lightning strike protection mesh for carbon fiber composite aircraft," *2016 17th International Symposium on Antenna Technology and Applied Electromagnetics*, Jul. 2016. [Online]. Available: http://dx.doi.org/10.1109/antem.2016.7550159

[45] L. Rufail, J. Laurin, and F. Moupfouma, "Composite aircraft lightning strike protection damage evaluation using microwave microscopy techniques," *2017 11th European Conference on Antennas and Propagation*, Mar. 2017. [Online]. Available: http://dx.doi.org/10.23919/eucap.2017.7928331

[46] W. Smythe, *Static and Dynamic Electricity.* McGraw-Hill, 1950.

[47] K. Awadalla and A. E. M. Sharshar, "A simple method to determine the impedance of a loop antenna," vol. 32, no. 11, pp. 1248–1251, Nov. 1984.

[48] M. Tabib-Azar, D.-P. Su, A. Pohar, S. LeClair, and G. Ponchak, "0.4 μm spatial resolution with 1 ghz (λ= 30 cm) evanescent microwave probe," *Review of Scientific Instruments*, vol. 70, no. 3, pp. 1725–1729, 1999. [Online]. Available: http://dx.doi.org/10.1063/1.1149658

[49] B. R. Jackson and B. Liao, "Uniform circular array with integrated microstrip tapered baluns," *2015 IEEE International Symposium on Antennas and Propagation USNC URSI National Radio Science Meeting*, Jul 2015. [Online]. Available: http://dx.doi.org/10.1109/aps.2015.7304500

[50] C. F. M. Carobbi and L. M. Millanta, "Analysis of the common-mode rejection in the measurement and generation of magnetic fields using loop probes," vol. 53, no. 2, pp. 514–523, April 2004.

[51] C. F. M. Carobbi, L. M. Millanta, and L. Chiosi, "The high-frequency behavior of the shield in the magnetic-field probes," in *IEEE International Symposium on Electromagnetic Compatibility*, 2000, pp. 35–40.

[52] E. L. Ginzton, *Microwave Measurements*. McGraw-Hill, 1957.

[53] E. Ginzton, "Microwave q measurements in the presence of coupling losses," *IEEE Transactions on Microwave Theory and Techniques*, vol. 6, no. 4, p. 383–389, Oct 1958. [Online]. Available: http://dx.doi.org/10.1109/tmtt.1958.1125210

[54] P. J. Petersan and S. M. Anlage, "Measurement of resonant frequency and quality factor of microwave resonators: Comparison of methods," *Journal of Applied Physics*, vol. 84, no. 6, p. 3392–3402, Sep 1998. [Online]. Available: http://dx.doi.org/10.1063/1.368498

[55] M. Sanchez, E. Martin, and J. Zamarro, "New vectorial automatic technique for characterisation of resonators," *IEE Proceedings H Microwaves, Antennas and Propagation*, vol. 136, no. 2, p. 147, 1989. [Online]. Available: http://dx.doi.org/10.1049/ip-h-2.1989.0026

[56] D. Kajfez, "Linear fractional curve fitting for measurement of high q factors," *IEEE Transactions on Microwave Theory and Techniques*, vol. 42, no. 7, p. 1149–1153, Jul 1994. [Online]. Available: http://dx.doi.org/10.1109/22.299749

[57] ——, "Numerical determination of two-port parameters from measured unrestricted data," *IEEE Transactions on Instrumentation and Measurement*, vol. 24, no. 1, p. 4–11, 1975. [Online]. Available: http://dx.doi.org/10.1109/tim.1975.4314360

[58] D. Pozar, *Microwave Engineering*. Wiley, 2004. [Online]. Available: https://books.google.ca/books?id=4wzpQwAACAAJ

[59] J. Chisum, M. Ramirez-Velez, and Z. Popovic, "Planar circuits for non-contact near-field microwave probing," 11 2009, pp. 802 – 805.

[60] Z. Chen, W. Hong, and J. Chen, "High-q planar active resonator based on substrate integrated waveguide technique," *Electronics Letters*, vol. 48, no. 10, p. 575, 2012. [Online]. Available: http://dx.doi.org/10.1049/el.2012.0508

[61] M. Tabib-Azar, T. Zhang, and S. LeClair, "Self-oscillating evanescent microwave probes for nondestructive evaluations of materials," *IEEE Transactions on Instrumentation and Measurement*, vol. 51, no. 5, p. 1126–1132, Oct 2002. [Online]. Available: http://dx.doi.org/10.1109/tim.2002.807798

APPENDIX A MATLAB CODE

A.1 Main control program

This piece of software controls centralizes the control of the probe station, PNA-A, RF switch. It also gathers the measured data.

```
function []=PbenchtestArray1()
clear all
global ProbeSt s numPoints
%The diffrence between PbenchtestArray is the formation of the S11 matrix.
% addpath('C:\Leandro\Visual Studio 2013\FTDI_VS\ft232h_dll\x64\Debug','C:\Leandro\Visual Studio 2013\FTDI_VS\ft232h_dll\ft232h_dll');
% if ~libisloaded('ft232h_dll')
%     loadlibrary('ft232h_dll.dll','ft232h_dll.h');
% end
%****CREATE AGILENT OBJ *****
naip='192.168.1.15';
naport=5025;
instrObj = instrfind('Type', 'tcpip', 'RemoteHost', naip, 'RemotePort',naport, 'Tag', '');
% Create the tcpip object if it does not exist
% otherwise use the object that was found.
if isempty(instrObj)
    instrObj = tcpip(naip,naport);
else
    fclose(instrObj);
    instrObj = instrObj(1);
end
instrObj.InputBufferSize = 10e6;
instrObj.ByteOrder = 'littleEndian';
%-----------------------------------------------------------------
% *** CREATE PROBE STATION OBJ
```

```
% Find a porbestation object (tcpip object) otherwise create it.
ProbeSt = instrfind('Type', 'tcpip', 'RemoteHost', '192.168.1.13', 'RemotePort', 1000, 'Tag', '');
if isempty(ProbeSt)
    ProbeSt = tcpip('192.168.1.13', 1000);
else
    fclose(ProbeSt);
    ProbeSt = ProbeSt(1);
end
fopen(ProbeSt);
ProbeSt.timeout=15; %If it's less than this valua a timeout occur when the chuck in going to the initial positioin.
%-----------------------------------------------------------------
probesep=11430; %[um]
LWD=3175;  %[um]
SWD=1422; %[um]
sqx=15;%[mm]
%sqx=probesep;]
sqy=70;%[mm]
%deltax=fix((LWD/4)*1e3);%[um]
nsep=fix(probesep/(LWD/4));
%nsep=1;
deltax=fix(probesep/nsep);
deltay=fix((SWD/4));%50;%200;% moving steps in y axis in [um]
%deltay=7000
deltaz=15500;%deltaz between the probe in the air and touching the surface
n=0;p=0; %fix(sqx*1000/deltax); %sqx and sqy controls a small square than samplebegin-sampleend ..
pymax=fix(sqy*1000/deltay); %staring at samplebegin
vair=90; %speed in the air
vsample=10;%speed sweeping the sample
%probe switching according to physical order.
s(1)=4;
s(2)=2;
```

```
s(3)=0;
s(4)=1;
s(5)=3;
s(6)=5;
IFfilterbw=.5e3;
numPoints=801;
span=.3e6;
f0=1e9;
%%%%%%————————————SAMPLE CALIBRATION————————————
%%%——This should be executed manually step by step———
samplecal=0;
if samplecal==1
    %Move the chuck to sample begin BOTTOM LEFT of the sample and execute
    %the following line
    inputdlg('Move the chuck to sample begin BOTTOM-LEFT corner and press OK')
    setbeginsample(ProbeSt)
%     inputdlg('Move the chuck to sample begin TOP-RIGHT corner and press OK')
%     %Move the chuck to sample UPPER RIGHT corner and execute.
%     setendsample(ProbeSt)
end

%%%%————————CALIBRATION————————————————
cal=0; %allowes to turn on and off the calibration. Set the probes over the sample where you want to calibrate.
if cal==1
    CalibrationProbe(ProbeSt,instrObj,probesep)
end
%%%%————————Segments TABLE CONFIG————————————
load('SegmentedCal.mat');
netanSegmentConfig((f0Segm+f1Segm)/2,span,numPoints,IFfilterbw)

%%————————————Network Analyser Keysight N5247a parameters Configuration————————
```

```
% netanalyserConfig(f0,span,numPoints,IFfilterbw);% netanalyserConfig(f0,span,numPoints,iffilter)

%%%******************** M A I N ************************************
load('home'); %load the the prositions samplebegin and sampleend
clearvars S11;
probepos=ReadChuckPositionZero(ProbeSt);
%define z coordinate for the probe on air: zposair
if probepos(3)-deltaz>0
    zposair=probepos(3)-deltaz;
else
    zposair=0;
end
MoveChuckZzero(ProbeSt,[zposair 100]); %Chuck down (lift probe) in Z axis - probe air position
MoveChuckZero(ProbeSt,[samplebegin(1:2) vair]); %move to beginning of measurement
for n=1:nsep %X movement = n x deltax
    MoveChuckZero(ProbeSt,[samplebegin(1)-deltax*(n-1) samplebegin(2) vair]);p=0; %Move chuck in the air until samplebegin
    MoveChuckZzero(ProbeSt,[samplebegin(3) 100]); %Move chuck up over samplez
    for p=1:pymax %Y movement relative deltay
        tic
        %disp('measurement')
        %ReadChuckPositionZero
        %pause(0.01);
        for sn = 1:6
            fnDportOut(s(sn)); %Switch to probe sn
            fprintf(instrObj,sprintf('SENS1:SEGM%.0f:STATE ON',sn)); %turn on the Segment
            if (sn>1)
```

```
                    fprintf(instrObj,sprintf('SENS1:SEGM%.0f:STATE OFF',sn-1));%turn off the previous segment
                else
                    fprintf(instrObj,sprintf('SENS1:SEGM%.0f:STATE OFF',6));%turn off the previous segment
                end
                rawdata=measurement(numPoints);
                S11(p,n+nsep*(sn-1),:)=rawdata(numPoints+1:2*numPoints)+j*rawdata(2*numPoints+1:3*numPoints);
                %                MagV=squeeze(20*log10(abs(S11(n+1,p+1,sn,:))));
                %                plot(rawdata(1:numPoints),MagV)
                %                drawnow
                %                hold on;
            end
            fprintf('%d %d %d \n',p,n,toc)
            MoveChuckrel(ProbeSt,[0 -deltay vsample]);
        end
        MoveChuckZzero(ProbeSt,[zposair vair]); %lift probe after the each Y scan
end
MoveChuckZzero(ProbeSt,[zposair vair]); %lift probe
save('SampleArrayStepFull','S11','nsep','deltax','deltay','f0Segm','f1Segm','IFfilterbw','span') %name of the file where the data has to be saved.
fclose(ProbeSt)
end


function [resp]=MoveChuckrel(ProbeSt,xyv)
fprintf(ProbeSt,'Cmd=0:34:%f %f R Y %u\n',xyv)
resp=fscanf(ProbeSt);
end

function [resp]=MoveChuckZero(ProbeSt,xyv)
fprintf(ProbeSt,'Cmd=0:34:%f %f Z Y %u\n',xyv)
```

```
resp=fscanf(ProbeSt);
end

function [resp]=MoveChuckZrel(ProbeSt,zv)
fprintf(ProbeSt,'Cmd=0:3B:%f R Y %u\n',zv)
resp=fscanf(ProbeSt);
end

function [resp]=MoveChuckZzero(ProbeSt,zv)
fprintf(ProbeSt,'Cmd=0:3B:%f Z Y %u\n',zv)
resp=fscanf(ProbeSt);
end


function [pos3]=ReadChuckPositionZero(ProbeSt)
fprintf(ProbeSt,'Cmd=0:31:Y Z')
pos3=fscanf(ProbeSt,['Rsp=0:0:%f %f %f'],[1 3]);
end

function [resp]=MoveChuckThetaZero(ProbeSt,deg)
fprintf(ProbeSt,'Cmd=0:53:%f Z D \n',deg)
resp=fscanf(ProbeSt)
end

function [resp]=MoveChuckThetaCenter(ProbeSt,deg)
fprintf(ProbeSt,'Cmd=0:53:%f C D \n',deg)
resp=fscanf(ProbeSt)
end

function [theta]=ReadChuckThetaCenter(ProbeSt)
fprintf(ProbeSt,'Cmd=0:51:D C')
theta=fscanf(ProbeSt,['Rsp=0:0:%f'],[1 1]);
end

function [pos3]=setbeginsample(ProbeSt)
pos3d=ReadChuckPositionZero(ProbeSt);
```

```
178 samplebegin=pos3d;
179 save('home','samplebegin','-append');
180 end
181
182 function [pos3]=setendsample(ProbeSt)
183 pos3d=ReadChuckPositionZero(ProbeSt);
184 sampleend=pos3d;
185 save('home','sampleend','-append');
186 end
187
188 function [f0Segm]=CalibrationProbe(ProbeSt,instrObj,probesep)
189 % The calibration consist in searching for the best f0 for each
      of the probe to later program the segmented sweep. So, at
      the end of the calibration we need to obtain 6 x f0 (one for
      earch probe)
190 % For each of the probes two measurement needs to be taken. On
      in the painted region and one in the non-painted region. For
      each of the measurements f0p(painted) and f0c(carbon - non-
      painted) needs to ne determined.
191 % The f0n (nprobe) is the mean of the two previous values
192 % where the calibration will take place
193 % All the probes should calibrate in the same point, so there
      will be a dx movement that takes place.
194 % samplebegin contains the position of the probe in the first
      point.(can
195 % be painted) Samplend ca be unpainted for example
196 global s numPoints
197 load('home'); %load the the prositions samplebegin and
      sampleend
198 IFfilterbw=.5e3;
199 span1=30e6; %necesary span to catch the resonances of all the
      probes.
200 f0=1e9;
201 netanalyserConfig(f0,span1,numPoints,IFfilterbw);%
      netanalyserConfig(f0,span,numPoints,iffilter)
202 vsample=10;
```

```
MoveChuckZzero(ProbeSt,[0 100]); %Chuck down (lift probe) in Z axis - probe air position
MoveChuckZero(ProbeSt,[samplebegin(1) samplebegin(2) 60]);
MoveChuckZzero(ProbeSt,[samplebegin(3) 100]);
%calibration over METAL
for sn = 1:6 %switch between the probes
    %MoveChuckZzero(ProbeSt,[0 100]); %Chuck down (lift probe) in Z axis - probe air position
    netanalyserConfig(f0,span1,numPoints,IFfilterbw);%netanalyserConfig(f0,span,numPoints,iffilter)
    fnDportOut(s(sn));
    %MoveChuckZero(ProbeSt,[samplebegin(1)+sn*probesep samplebegin(2) 60]); %X+ movements!!
    %MoveChuckZzero(ProbeSt,[samplebegin(3) 100]);
    f0min=netanSearchMin(instrObj);
    netanalyserConfig(f0min,300e3,numPoints,IFfilterbw);%netanalyserConfig(f0,span,numPoints,iffilter)
    f0min=netanSearchMin(instrObj);%probe over metal
    netanalyserConfig(f0min,300e3,numPoints,IFfilterbw);%netanalyserConfig(f0,span,numPoints,iffilter)
    rawdata=measurement(numPoints);
    S11calmetal(sn,:)=rawdata(numPoints+1:2*numPoints)+j*rawdata(2*numPoints+1:3*numPoints);
    f0Segm(sn)=f0min;
end
MoveChuckZzero(ProbeSt,[0 100]); %Chuck down (lift probe) in Z axis - probe air position
IFfilterbw=.5e3;
span1=30e6; %necesary span to catch the resonances of all the probes.
f0=.99e9;
netanalyserConfig(f0,span1,numPoints,IFfilterbw);%netanalyserConfig(f0,span,numPoints,iffilter)
vsample=10;
for sn = 1:6 %switch between the probes
```

```
    netanalyserConfig(f0,span1,numPoints,IFfilterbw);%netanalyserConfig(f0,span,numPoints,iffilter)
    fnDportOut(s(sn));
    f1min=netanSearchMin(instrObj);
    netanalyserConfig(f1min,300e3,numPoints,IFfilterbw);%netanalyserConfig(f0,span,numPoints,iffilter)
    f1min=netanSearchMin(instrObj);
    netanalyserConfig(f1min,300e3,numPoints,IFfilterbw);%netanalyserConfig(f0,span,numPoints,iffilter)
    rawdata=measurement(numPoints);
    S11calair(sn,:)=rawdata(numPoints+1:2*numPoints)+j*rawdata(2*numPoints+1:3*numPoints);
    f1Segm(sn)=f1min;
end

save('SegmentedCal.mat','S11calmetal','S11calair','f0Segm','f1Segm','span1','numPoints','IFfilterbw') %name of the file where the data has to be saved.
end
```

A.2 Calibration function

```
%-----------------------------------------------------
load('SampleArraySmallCut'); %we have to normalize the steped sample with the undamaged sample.
for ip=1:6
    for j=1:nsep
        for i=1:size(S11,1)
            [sm,im]=min(abs(S11(i,j+nsep*(ip-1),:)));
            S11Min(i,j+nsep*(ip-1))=sm;
            ResIndexip(i,j+nsep*(ip-1))=im;
        end
    end
    probeaux=ResIndexip(:,nsep*(ip-1)+1:nsep*ip);
    ResIndexMean(ip)=mean(reshape(probeaux,[numel(probeaux),1]));
```

```
    ResIndexStd(ip)=std(reshape(probeaux,[numel(probeaux),1]));
    ResIndexNorm(:,nsep*(ip-1)+1:nsep*ip)=(ResIndexip(:,nsep*(ip-1)+1:nsep*ip)-ResIndexMean(ip))/ResIndexStd(ip);
end
MeanUndamaged=ResIndexMean;
StdUndamaged=ResIndexStd;
clear S11 ResIndexip ResIndexNorm;

%--------Normalized DATA PLOT--------------------------------------
clear S11 ResIndexip ResIndexNorm;
load('SampleArrayStepFull');
%load('SampleArrayStepFull');
%load('SampleArraySmallCut');
%load('SampleArrayNoDefect');
for ip=1:6
    for j=1:nsep
        for i=1:size(S11,1)
            [sm,im]=min(abs(S11(i,j+nsep*(ip-1),:)));
            S11Min(i,j+nsep*(ip-1))=sm;
            ResIndexip(i,j+nsep*(ip-1))=im;
        end
    end
    probeaux=ResIndexip(:,nsep*(ip-1)+1:nsep*ip);
    ResIndexMean(ip)=mean(reshape(probeaux,[numel(probeaux),1]));
    ResIndexStd(ip)=std(reshape(probeaux,[numel(probeaux),1]));
    %ResIndexNorm(:,nsep*(ip-1)+1:nsep*ip)=(ResIndexip(:,nsep*(ip-1)+1:nsep*ip)-ResIndexMean(ip))/ResIndexStd(ip);
    ResIndexNorm(:,nsep*(ip-1)+1:nsep*ip)=(ResIndexip(:,nsep*(ip-1)+1:nsep*ip)-MeanUndamaged(ip))/StdUndamaged(ip);
end

% write matrix to tab files
%writematrix(ResIndexipfreq,'SampleArraySmallCutNoCorr.txt','Delimiter','tab');
% writematrix NOTAVAILABLE IN THIS VERSION OF MATLAB
```

```
%dlmwrite('SampleArraySmallCutNoCorr.txt',ResIndexipfreq,'delimiter','\t','precision',9);
%dlmwrite('SampleArrayStep.txt',ResIndexNorm,'delimiter','\t','precision',9);


% Ploting indexes.
[X,Y] = meshgrid((1:size(ResIndexip,2))*deltax/1e3,(1:size(ResIndexip,1))*deltay/1e3);
figure(5)
figure1hl=surf(X,Y,ResIndexip);
xlabel('x [mm]');


figure(7)
surf(X,Y,ResIndexNorm);
xlabel('x [mm]');
%dlmwrite('SampleArraySmallCutNorm.txt',ResIndexNorm,'delimiter','\t','precision',3);
%dlmwrite('SampleArrayStep.txt',ResIndexNorm,'delimiter','\t','precision',3);


figure(8) %contour plots
contour(X,Y,ResIndexip,40)
xlabel('x [mm]');

figure(9) %contour plots
contour(X,Y,ResIndexNorm,50)
xlabel('x [mm]');


%------ploting normalized data per row
% every row is separated by a distance of 0.355mm
figure(10)
for row=10:14
```

```
    subplot(4,1,row-10+1)
    hold on
    grid on
    grid minor
    deltay=0.355*(row-10);
    titletxt=['deltay=',num2str(deltay)];
    title(titletxt);
    for ip=1:6
        txt=['probe',num2str(ip)];
        plot(nsep*(ip-1)+1:nsep*ip,ResIndexNorm(row,nsep*(ip-1)
            +1:nsep*ip));
    end
    hold off
end

%%%----------UnNorm Raw data rows----------
figure(11)
for row=10:14
    subplot(4,1,row-10+1)
    hold on
    grid on
    grid minor
    deltay=0.355*(row-10);
    titletxt=['deltay=',num2str(deltay)];
    title(titletxt);
    for ip=1:6
        txt=['probe',num2str(ip)];
        plot(nsep*(ip-1)+1:nsep*ip,ResIndexip(row,nsep*(ip-1)
            +1:nsep*ip));
    end
    hold off
end
```

APPENDIX B C CODE: FT232H

```
# include "mex.h"
#include <stdio.h>
#include <string.h>
#include <math.h>
#include <ftd2xx.h>
#include <Windows.h>
#include "stdio.h"

void mexFunction(int nlhs, mxArray *plhs[], int nrhs, const
    mxArray *prhs[]);

void mexFunction(int nlhs, mxArray *plhs[], int nrhs, const
    mxArray *prhs[])

{
        int x;
        /*
        INPUT:
        Retrieve the (first) (scalar) input argument from the
            line
        */
        x = mxGetScalar(prhs[0]);
        FT_HANDLE ftHandle;
        FT_STATUS ftStatus;
        DWORD BytesWritten;
        ftStatus = FT_Open(0, &ftHandle);
        if (ftStatus != FT_OK) {
                // FT_Open failed
        }
        if (ftStatus == FT_OK) {
                // FT_Write OK
                FT_SetBitMode(ftHandle, 0xFF, 1);
                FT_SetBaudRate(ftHandle, 9600);  /* Actually
```

```
                    9600 * 16 */
31          }
32          else {
33                  // FT_Write Failed
34          }
35          // write data to port
36          ftStatus = FT_Write(ftHandle, &x, 1, &BytesWritten);
37          //close device
38          FT_Close(ftHandle);
39  }
```

APPENDIX C PUBLICATIONS

- L. Rufail, J. J. Laurin, and F. Moupfouma, "On the use of microwave microscopy for detecting defects in the lightning strike protection mesh for carbon fiber composite aircraft," *2016 17th International Symposium on Antenna Technology and Applied Electromagnetics*, Jul. 2016.

- L. Rufail, J. Laurin, and F. Moupfouma, "Composite aircraft lightning strike protection damage evaluation using microwave microscopy techniques," *2017 11th European Conference on Antennas and Propagation,* Mar. 2017.

- L. Rufail and J. J. Laurin, "Composite Aircraft Lightning Strike Protection Damage Evaluation Using Microwave Microscopy," *IEEE Transactions on Instrumentation and Measurement,* vol. 69, no. 6, pp. 3804–3811, Jun. 2020.

- "Apparatus and methods for non-destructive inspection using microwave microscopy." Canada. CA2,972,435 and US62/527,336. 2017/07/04. Patent Status: Pending Inventors: L. Rufail. J.-J. Laurin and F. Moupfouma